ตัวเร่งปฏิกิริยานิกเกิลบนเส้นใยซิลิกาสำหรับการผลิตแก๊สสังเคราะห์จากรีฟอร์มิงด้วยไอน้ำ

ของเอทานอลและกรดแอซีติก

นางสาวนรรฏธวรรณ ประสงค์ธรรม

วิทยานิพนธ์นี้เป็นส่วนหนึ่งของการศึกษาตามหลักสูตรปริญญาวิทยาศาสตรดุษฎีบัณฑิต
สาขาวิชาปิโตรเคมี
คณะวิทยาศาสตร์ จุฬาลงกรณ์มหาวิทยาลัย
ปีการศึกษา 2559

Ni/SiO$_2$ FIBER CATALYST FOR SYNGAS PRODUCTION FROM STEAM

REFORMING OF ETHANOL AND ACETIC ACID

Miss Natthawan Prasongthum

A Dissertation Submitted in Partial Fulfillment of the Requirements

for the Degree of Doctor of Philosophy Program in Petrochemistry

Faculty of Science

Chulalongkorn University

Academic Year 2016

Thesis Title	Ni/SiO$_2$ FIBER CATALYST FOR SYNGAS PRODUCTION FROM STEAM REFORMING OF ETHANOL AND ACETIC ACID
By	Miss Natthawan Prasongthum
Field of Study	Petrochemistry
Thesis Advisor	Associate Professor Prasert Reubroycharoen, Ph.D.

Accepted by the Faculty of Science, Chulalongkorn University in Partial Fulfillment of the Requirements for the Doctoral Degree

⋯⋯⋯⋯⋯⋯⋯⋯⋯⋯⋯⋯⋯Dean of the Faculty of Science

(Associate Professor Polkit Sangvanich, Ph.D.)

THESIS COMMITTEE

⋯⋯⋯⋯⋯⋯⋯⋯⋯⋯⋯⋯⋯Chairman

(Assistant Professor Warinthorn Chavasiri, Ph.D.)

⋯⋯⋯⋯⋯⋯⋯⋯⋯⋯⋯⋯⋯Thesis Advisor

(Associate Professor Prasert Reubroycharoen, Ph.D.)

⋯⋯⋯⋯⋯⋯⋯⋯⋯⋯⋯⋯⋯Examiner

(Professor Tharapong Vitidsant, Ph.D.)

⋯⋯⋯⋯⋯⋯⋯⋯⋯⋯⋯⋯⋯Examiner

(Associate Professor Wimonrat Trakarnpruk, Ph.D.)

⋯⋯⋯⋯⋯⋯⋯⋯⋯⋯⋯⋯⋯External Examiner

(Assistant Professor Chanatip Samart, Ph.D.)

นรรฏธวรรณ ประสงค์ธรรม : ตัวเร่งปฏิกิริยานิกเกิลบนเส้นใยซิลิกาสำหรับการผลิตแก๊สสังเคราะห์จากรีฟอร์มิง ด้วยไอน้ำของเอทานอลและกรดแอซีติก (Ni/SiO$_2$ FIBER CATALYST FOR SYNGAS PRODUCTION FROM STEAM REFORMING OF ETHANOL AND ACETIC ACID) อ.ที่ปรึกษาวิทยานิพนธ์หลัก: รศ. ดร.ประเสริฐ เรียบร้อยเจริญ, 147 หน้า.

งานวิจัยนี้ได้สังเคราะห์ตัวเร่งปฏิกิริยานิกเกิลบนเส้นใยซิลิกา (NiSF) สำหรับการผลิตไฮโดรเจนจากรีฟอร์มมิง ด้วยไอน้ำของเอทานอลได้สำเร็จโดยเทคนิคอิเล็กโทรสปินนิงและวิธีการเปียกชุ่ม ในงานวิจัยนี้สนใจศึกษาผลของอุณหภูมิใน การทำปฏิกิริยา สัดส่วนไอน้ำต่อคาร์บอน (S/C) น้ำหนักตัวเร่งปฏิกิริยาต่ออัตราการไหล (W/F) และปริมาณโลหะนิกเกิล ของตัวเร่งปฏิกิริยา NiSF ที่มีผลต่อความว่องไวในการเกิดปฏิกิริยาและการผลิตไฮโดรเจนรวมถึงคุณสมบัติของผลิตภัณฑ์ ข้างเคียงคาร์บอนนาโนทิวบ์ (CNTs) พบว่า ตัวเร่งปฏิกิริยา NiSF มีประสิทธิภาพในการผลิตไฮโดรเจนควบคู่กับการผลิต CNTs โดยภาวะที่เหมาะสมของการรีฟอร์มมิงด้วยไอน้ำของเอทานอลในรูปของการเปลี่ยนเอทานอลและผลผลิตไฮโดรเจน คือ อุณหภูมิ 600 องศาเซลเซียส S/C เท่ากับ 9:1 และ W/F เท่ากับ 18 กรัมของตัวเร่งปฏิกิริยาที่ 1 ชั่วโมงต่อโมล ซึ่งให้ผล ผลิตไฮโดรเจน สูงสุดเท่ากับ 55% ในขณะที่คุณภาพและปริมาณของ CNTs และผลผลิตไฮโดรเจนที่ 29% สามารถผลิตโดย ใช้ปริมาณโลหะนิกเกิลร้อยละเท่ากับ 30 S/C เท่ากับ 1:1 และ W/F เท่ากับ 9 กรัมของตัวเร่งปฏิกิริยาที่ 1 ชั่วโมงต่อโมล การเกิดคาร์บอนนาโนทิวป์-ซิลิกาไฟเบอร์ (CNTs-SF-E) ถือเป็นคอมโพสิตชนิดใหม่ ที่มีพื้นที่ผิวสูงและว่องไวต่อการทำ ปฏิกิริยา เหมาะในการนำมาใช้เป็นตัวรองรับสำหรับตัวเร่งปฏิกิริยา ดังนั้นในส่วนที่สองของการศึกษา CNTs-SF-E คอมโพ สิตได้นำมาประยุกต์ใช้เป็นตัวรองรับตัวเร่งปฏิกิริยานิกเกิลในการรีฟอร์มมิงด้วยไอน้ำของเอทานอลสำหรับผลิตไฮโดรเจนโดย ใช้ปริมาณโลหะนิกเกิลร้อยละเท่ากับ 5 และ 10 ศึกษาประสิทธิภาพของตัวเร่งปฏิกิริยาเปรียบเทียบกับตัวเร่งปฏิกิริยานิกเกิล บนเส้นใยซิลิกา (10NiSF) และตัวเร่งปฏิกิริยานิลเกิลบนพอรัสซิลิกา (10NiSP) อุณหภูมิที่ใช้ศึกษาอยู่ในช่วงอุณหภูมิต่ำ 300 ถึง 500 องศาเซลเซียส ผลการศึกษาพบว่า ที่อุณหภูมิต่ำตัวเร่งปฏิกิริยา 10NiCNTs-SF-E มีความว่องไวและมีความเสถียรสูง เนื่องจากตัวเร่งปฏิกิริยามีการกระจายตัวที่ดีและสามารถเข้าทำปฏิกิริยาได้ง่าย ในส่วนที่สามของการศึกษา เป็นการ เปรียบเทียบลักษณะของ CNTs ที่ผลิตจากรีฟอร์มมิงด้วยไอน้ำของกรดแอซิติกและเอทานอล โดยใช้ภาวะที่ใกล้เคียงกัน พบว่าคาร์บอนที่เกิดจากเอทานอลเป็น CNTs ในขณะที่คาร์บอนที่เกิดจากการแตกตัวของกรดแอซิติกนอกจากจะได้ CNTs แล้วยังได้คาร์บอนที่มีลักษณะเป็นเส้นใยม้วนพันกัน นอกจากนี้ CNTs ที่ผลิตจากกรดแอซิติกจะมีขนาดเส้นผ่าศูนย์กลาง ภายนอกใหญ่กว่า CNTs ที่ผลิตจากเอทานอล โดยความแตกต่างของการเกิดคาร์บอนของกรดแอซิติกและเอทานอลสัมพันธ์ กับจำนวนออกซิเจนที่แตกต่างกันของสารตั้งต้น คาร์บอนนาโนทิวป์-ซิลิกาไฟเบอร์คอมโพสิต (CNTs-SF-A) ที่ได้จากรีฟอร์ม มิงด้วยไอน้ำของกรดแอซิติกมาใช้เป็นตัวรองรับตัวเร่งปฏิกิริยานิกเกิลในการรีฟอร์มมิงด้วยไอน้ำของกรดแอซิติก โดยใช้ตัวเร่ง ปฏิกิริยา 10NiCNTs-SF-E, 10NiSF และ 10NiSP เป็นตัวเปรียบเทียบ พบว่าตัวเร่งปฏิกิริยานิกเกิลบนตัวรองรับ CNTs-SF-E และ CNTs-SF-A มีการกระจายตัวที่ดีและมีขนาดเล็ก ในการศึกษาประสิทธิภาพของตัวเร่งปฏิกิริยาพบว่า ตัวเร่งปฏิกิริยา 10NiCNTs-SF-E มีความสามารถในการเปลี่ยนกรดแอซิติกสูงกว่าตัวเร่งปฏิกิริยาอื่น ผลของตัวเร่งปฏิกิริยาหลังจากทำ ปฏิกิริยา 4 ชั่วโมงพบว่า คาร์บอนส่วนใหญ่บนตัวเร่งปฏิกิริยาเส้นใยคอมโพสิตและเส้นใยซิลิกาเป็นคาร์บอนแบบว่องไวซึ่ง กำจัดได้ง่ายด้วยออกซิเดชัน ในขณะที่คาร์บอนบนตัวเร่งปฏิกิริยา 10NiSP ยากต่อการกำจัดและไม่สามารถคำนวณปริมาณ คาร์บอนที่แน่นอนได้ เนื่องจากพื้นที่ผิวของตัวเร่งปฏิกิริยา 10NiSP ถูกปกคลุมด้วยพอริเมอร์ไรซ์คาร์บอนจำนวนมาก

สาขาวิชา   ปิโตรเคมี   ลายมือชื่อนิสิต _____

ปีการศึกษา 2559   ลายมือชื่อ อ.ที่ปรึกษาหลัก _____

V

5672819523 : MAJOR PETROCHEMISTRY

KEYWORDS: STEAM REFORMING / NICKEL-BASED CATALYST / SILICA FIBER / CARBON NANOTUBES / ETHANOL / ACETIC ACID

NATTHAWAN PRASONGTHUM: Ni/SiO$_2$ FIBER CATALYST FOR SYNGAS PRODUCTION FROM STEAM REFORMING OF ETHANOL AND ACETIC ACID. ADVISOR: ASSOC. PROF. PRASERT REUBROYCHAROEN, Ph.D., 147 pp.

In this research, synthesis of Ni/silica fiber (NiSF) catalyst for hydrogen production in ethanol steam reforming was successfully synthesized by electrospinning technique following by conventional impregnation method. The effects of reaction temperature, steam to carbon ratio (S/C), weight to flow rate ratio (W/F) and Ni loading of the NiSF catalyst on the reaction activity and H$_2$ production as well as CNTs characteristics (as a by-product) were investigated. The NiSF catalyst exhibited high activity to the simultaneous production of hydrogen and CNTs. The optimized conditions of ethanol steam reforming in terms of ethanol conversion and H$_2$ yield were achieved at 600 °C, S/C of 9:1 and W/F of 18 g$_{cat}$h/mol with a maximum hydrogen yield of 55%. Whereas, the quality and the quantity of CNTs formation along with a H$_2$ yield of 29% were obtained at Ni loading of 30 wt%, S/C of 1:1 and W/F of 9 g$_{cat}$h/mol. The novel carbon nanotubes-silica fiber composite (CNTs-SF-E) obtained from ethanol steam reforming exhibited relatively high surface area and easy accessibility, which can be applied as a support catalyst. Therefore, in the second part of this study, the CNTs-SF-E composite was applied as a support catalyst for Ni in ethanol steam reforming for hydrogen production by Ni loading at 5 and 10 wt%. The reaction performance of 10NiCNTs-SF-E catalyst was investigated and compared with that of Ni/silica fiber catalyst (10NiSF), and Ni/silica porous catalyst (10NiSP). The effect of temperature on ethanol conversion and products distribution was studied at low-temperature in the range of 300 and 500 °C. The 10NiCNTs-SF-E catalyst exhibited the best performance in term of stability and high activity at lower reaction temperature. The outstanding performance of 10NiCNTs-SF-E catalyst could be associated with high metallic dispersion and easy accessibility of ethanol to the active site. In the third part of this study investigated CNTs characteristics produced from steam reforming of different carbon sources: acetic acid and ethanol. Under the similar reaction conditions, ethanol was found to favor the growth of CNTs, while acetic acid was capable of the formation of both CNTs and curled shape filament carbon. Furthermore, CNTs obtained from acetic acid had larger outer diameters and a shorter length as compared to CNTs obtained from ethanol. The difference in the carbon formation could be attributed to the different number of oxygen atoms of both feed. The carbon nanotubes-silica fiber composite (CNTs-SF-A) produce from acetic acid was used as a support catalyst in acetic acid steam reforming, using 10NiCNTs-SF-E, 10NiSF and 10NiSP as comparative support. 10NiCNTs-SF-A and 10NiCNTs-SF-E catalysts exhibited high dispersion and smaller metal nanoparticles. Catalytic performances demonstrated that 10NiCNTs-SF-E exhibited significantly higher acetic acid conversion as compared with the other catalysts. The results of catalysts after 4 h of the reaction indicated that most of the carbon species over fibrous composite and fiber catalysts were relatively reactive carbon species which could be easily removed by oxidation, while carbon formation on 10NiSP was difficult to be removed and estimated the exact amount because 10NiSP surface was covered by a large amount of polymerized carbon.

Field of Study: Petrochemistry	Student's Signature	-------------------------
Academic Year: 2016	Advisor's Signature	-------------------------

ACKNOWLEDGEMENTS

I would like to thank to all the people who contributed to this thesis in innumerable ways. First and foremost, I would like to express my sincere gratitude to my advisor Assoc. Prof. Dr. Prasert Reubroychareon for his kind support during my Ph.D study and research. I would like to thank him for his patience, enthusiasm and guidance at all times during the research. He always gave me sound advice that helped me to achieve my aims. By benefiting from his experience, I learned many fundamental skills and acquired much invaluable knowledge of catalysis. Without him, this thesis would not have been written or completed.

I am very grateful to Assist. Prof. Dr. Warinthorn Chavasiri, Prof. Dr. Tharapong Vitidsant, Assoc. Prof. Dr. Wimonrat Trakarnpruk and Assist. Prof. Dr. Chanatip Samart for serving as chairman and members of thesis committee, respectively and for their worthy comments and suggestions.

I would like to acknowledge the financial support of Science Achievement Scholarship of Thailand (SAST) and Overseas Academic Presentation Scholarship for Graduate Students, Graduate School, Chulalongkorn University. I would also like to thank the Department of Chemical Technology, Chulalongkorn University for instrument support.

Then I would like to thank to Assist. Prof. Dr. Chaiyan Chaiya for his kind support Thermogravimetic and Differential Thermal instrument.

I also wish to express my great appreciation to every laboratory worker of Assoc. Prof. Prasert for helping and encouragement.

To my close friend and sister by choice, Dr. Paweesuda Natewong for her deepest friendship and irreplaceable encouragement.

Last but not least, I appreciate the encouragement, support and understanding from each members in my family. Thank you very much.

CONTENTS

จุฬาลงกรณ์มหาวิทยาลัย
CHULALONGKORN UNIVERSITY

LIST OF FIGURES

LIST OF TABLES

CHAPTER I
GENERAL BACKGROUND

1.1   Introduction

Nowadays, petroleum-based fuels are the main energy resources for the worldwide energy demand over the past two centuries. However, the burning of fossil fuels has resulted in significant CO_2 which could cause global warming and air pollution. Moreover, our heavy reliance makes them less abundant and more expensive. Hence, the utilization alternative fuels which are environmentally friendly, abundant and low releasing CO_2 have received significant attention in recent research. Hydrogen is generally considered as a promising alternative fuel source to replace fossil fuels. Electricity can be directly generated by hydrogen fuel cell. Hydrogen is also a potential feedstock in the oil refinery and chemical industry. Hydrogen can be obtained from various sources such as fossil resources (coal and natural gas) and renewable (biomass and water). Currently, almost 50% hydrogen is produced from the light oil fraction or natural gas by steam reforming process[1]. The use of fossil-based feedstock is unsustainable and generates enormous undesirable greenhouse gases. Therefore, an alternative pathway to reduce environmental emissions will be needed for the hydrogen production in the next future. Ethanol is the one of interesting sources for hydrogen production since it is a clean source deriving from renewable biomass and widely available around the world at a relatively low cost. Currently, ethanol is mainly

obtained from the fermentation process of corn grains, sugar cane and other starch-rich materials. Acetic acid represents another as a promising and economically available hydrogen source. Similar to other oxygenated derived from renewable biomass; acetic acid is an organic material resource, which can be produced from fermentation of biomass. It also represents as the main components of bio-oil obtained by biomass pyrolysis and hence recent studies are more focused on testing acetic acid as a model material for steam reforming of bio-oil. For this reason, the use of ethanol and acetic acid to produce hydrogen production would open up an opportunity for the utilization of the renewable resources. The steam reforming is one of the most effective processes for converting opportunity sources into a sustainable source of hydrogen [2-4]. This process also produces the co-production of carbon nanotubes (CNTs) and carbon nanofibers (CNFs). The valuable CNTs product is receiving considerable attention due to its unique structural properties, including high specific surface area, high thermal stability and excellent electrical conductivity. These advantages allow it to be used in various applications, especially in composite materials [5-7]. Therefore, steam reforming of ethanol and acetic acid has been widely investigated in various research groups. Steam reforming has been greatly investigated using several catalytic materials, for instance, transition metals and noble metals. Although noble metal-based catalysts demonstrate excellent activity and stability in steam reforming, their application in large scale could be limited by their high cost. For this reason, the development of non-noble catalysts with high catalytic activity

and stability has been studied in recent years. Among non-noble catalysts, especially Ni-based catalyst, has shown remarkable activity and has been commonly used in commercial steam reforming process because of its high performance, low cost and wide availability [8]. Alumina and silica are commonly used as support catalyst for nickel in ethanol steam reforming due to their high specific surface area [9]. Unfortunately, strong acidic property of alumina easily promotes carbon deposition through the formation of ethylene intermediate, which is a serious problem for nickel-based catalysts. Compared to the alumina, silica is inherently neutral acidity/basicity property, high specific surface area and excellent thermal stability [10]. On the contrary, weak interaction between Ni and silica can promote metal aggregation, which is the key factor catalyst deactivation [11]. In liquid and gas phase reactions, the reaction rate conversion and product selectivity in heterogeneous catalysts are often negatively affected by mass transfer limitations, especially in porous catalysts [12-14]. Internal mass transfer limitations can be minimized by lowering the tortuosity of the catalyst support and maximizing the porosity. The fibrous structure of silica has been considered as a promising alternative support material for Ni catalysts because of their extremely open morphology which can easily access of their active sites as compared with the traditional use of pores [15]. In addition, the catalyst in a fibrous form exhibited the excellent mass/heat transfer characteristics and low pressure drops, which may result in improve the efficiency of catalysts [16]. Reubroycharoen et al. [17] have developed a fibrous Ni/SiO_2 catalyst for steam reforming of glycerol. They found that

the fiber catalyst presented superior catalytic activity and stability compared to a conventional porous catalyst due to their high accessibility with extremely open morphology of silica fiber. However, silica fiber catalyst had a relatively small specific surface. Additionally, weak interaction between active species and silica support had negative to stability of catalysts, which led to aggregation of nickel nanoparticles and catalyst deactivation eventually. With regard to these issues, other unconventional structures have been investigated. In recent years, carbon nanotubes (CNTs) have been considered as a promising alternative support due to their unique tubular structure and large specific surface areas, which significantly enhance the dispersion of the active sites. In addition, the tubular morphology consists of graphene layers, involving π-electron density, which can efficiently promote electron transfer between metallic active sites and the support to the reactants. The remarkable unique properties of CNTs make them most ideal and promising components for fabricating composite materials that exhibit one and/or more of these properties, making it suitable for use in various applications [18]. In the last year new composite materials was used as a support catalyst in PEM fuel cell. The composite materials exhibited enhance catalyst stability [19]. For this reason, the combination of silica fiber and CNTs as the composite is of interest. The CNTs hybridizing of silica fibers which combined of the advantages of carbon nanostructure and the extremely open structure of silica fiber would be used as a support for nickel catalyst in steam reforming process to solve the mass transfer limitation problem as well as enhance catalytic activity and stability. Recently,

Chernyak et al. [20] have developed hybrid composites which comprised of CNTs and conventional porous Al_2O_3 as an alternative support for cobalt catalyst in Fischer-Tropsch synthesis and they found that the hybrid composite catalysts presented remarkable catalytic activity and stability as well as outperformed other supports. CNTs are one of the by-product occurred during steam reforming. The use of ethanol and acetic acid to growing long CNTs is very important because it is a clean carbon source. As CNTs can be applied in many applications, the growth of carbon nanotubes on silica fibers would be a new material for extending the application of CNTs.

1.2   Scope of this work

In this work, ethanol and acetic acid steam reforming were investigated to produce hydrogen and synthesize a new kind of carbon nanotubes-silica fibrous composite at the same time. The effects of Ni loading, space-time (W/F), reaction temperature and steam to carbon ratio (S/C) on gas production and carbon nanotubes deposits were investigated. The fibrous carbon nanotubes-silica composite was then used as a support for nickel in steam reforming of ethanol and acetic acid. The large surface area of CNTs combined the advantages of tubular structure silica fiber were expected to enhance catalytic activities with small Ni particles and sufficient active areas which was useful for achieve high yield of hydrogen as well as improve catalytic stability by suppressing carbon deposition. This research work was scoped as follow:

1. Synthesis of Ni/silica fiber by using a combination method of sol-gel process and electrospinning technique following by conventional impregnation method.

2. Characterization of the Ni/silica fiber catalysts using nitrogen adsorption–desorption (BET), X-ray diffraction (XRD), Scanning electron microscopy equipped with energy-dispersive X-ray analysis (SEM-EDX) and temperature-programmed reduction of hydrogen (H_2-TPR).

3. Study of catalytic performance of Ni/silica fiber catalysts for co-production of hydrogen and carbon nanotubes-silica fiber (CNTs-SF-E) composite in steam reforming of ethanol in the fixed bed reactor with various parameters and the reaction products were analyzed by GC. Investigated parameters are

- Ni loading (10, 20 and 30 wt%)

- Weight of catalyst to feed flow rate (W/F) (9, 12, 18 and 36 g_{cat}h/mol)

- Temperature (400, 500, and 600 °C)

- Mole ratio of steam to carbon (S/C) ratio (1, 3, 6, 9 and 12)

4. Purification of carbon nanotubes-silica fiber (CNTs-SF-E) composite.

5. Preparation of NiCNTs-SF-E catalyst by impregnation method using Ni/silica fiber catalyst (NiSF), and Ni/silica porous catalyst (NiSP) as comparative catalysts.

6. Characterization of the catalysts using nitrogen adsorption–desorption (BET), X-ray diffraction (XRD), scanning electron microscopy equipped with energy-dispersive X-ray analysis (SEM-EDX) and temperature-programmed reduction of hydrogen (H_2-TPR).

7. Study of catalytic performance and stability of the catalysts in ethanol steam reforming.

8. Synthesis of carbon nanotubes-silica fiber composite from acetic acid steam reforming (CNTs-SF-A) and characterization of the NiCNTs-SF-A catalyst using nitrogen adsorption–desorption (BET), X-ray diffraction (XRD), scanning electron microscopy equipped with energy-dispersive X-ray analysis (SEM-EDX).

9. Catalytic performance of NiCNTs-SF-A catalyst in acetic acid steam reforming using NiCNTs-SF-E, NiSF, and NiSP as comparative catalysts.

1.3   Objectives

1. To prepare SiO_2-supported Ni fiber catalysts by electrospinning method for co-production of hydrogen and carbon nanotubes-silica fiber composite from ethanol steam reforming (CNTs-S-E).

2. To synthesize NiCNTs-SF-E catalyst and investigate catalytic performance of the synthesized catalyst in steam reforming of ethanol.

3. To synthesize carbon nanotubes-silica fibrous composite (CNTs-SF-A) by acetic acid steam reforming and its use as a novel catalyst support for acetic acid steam reforming.

CHAPTER II

THEORY AND LITERATURE REVIEWS

2.1   Hydrogen

Hydrogen is regarded as one of the most widely used chemical elements in the world. It can be used in many industrial fields, including in the manufacture of ammonia and in the hydrogenation of CO_2 and organic compounds to produce a variety of chemicals and fuels. Hydrogen appears to be a clean energy of the future and a potential source of transportation and electricity production since it possesses high energy density and buns cleanly with less environmental pollutants (producing only water) [21]. Hydrogen can be obtained from a variety of sources such as fossil resources (natural gas and coal) and renewable resources (biomass and water) [22]. An overview of the various processes and feedstock or hydrogen production is shown in **Figure 2.1**.
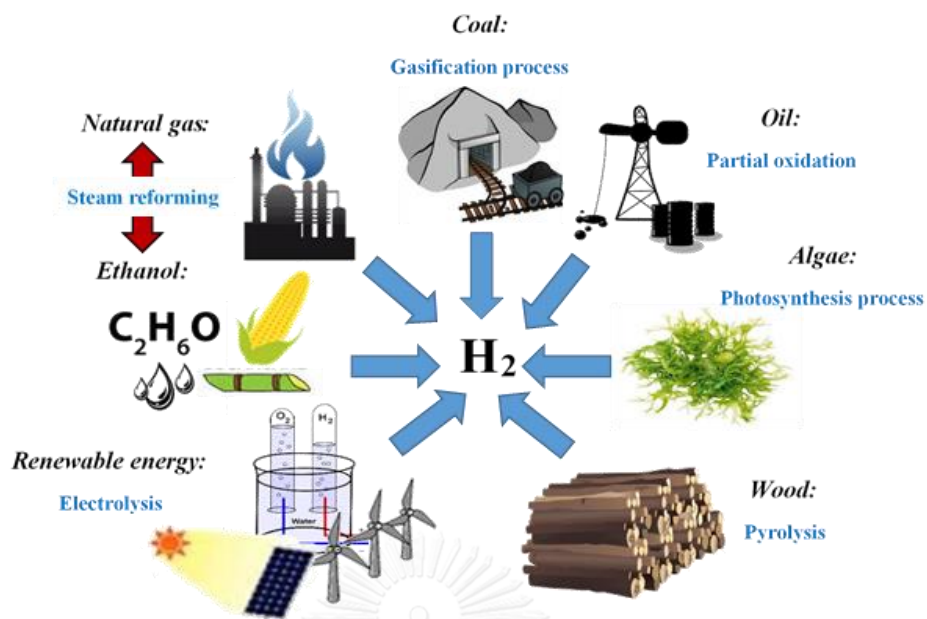
Figure 2.1 Feedstock and process for production of hydrogen

2.2   Synthesis gas (Syngas)

A mixture of hydrogen (H_2) and carbon monoxide (CO) or syngas is a significant feedstock for the manufacture of variety of chemicals (methanol production), long chain hydrocarbons or Fischer-Tropsch fuel and CO-tolerant fuel cells.

Syngas can be produced from oxygenated hydrocarbons like glycerol, ethanol, n-butanol and bio-oil. Recently, steam reforming of oxygenated hydrocarbons is the new technologies with potential industrial interest.
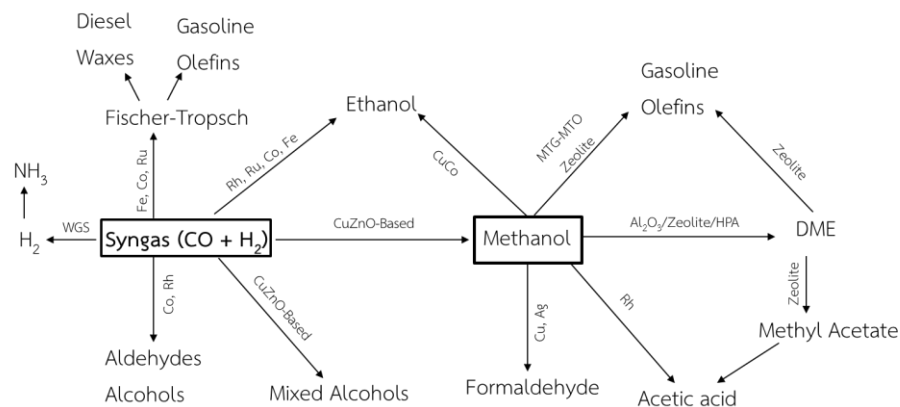
Figure 2.2 Simple flow diagram for production of fuels and chemicals from syngas

2.3   Processes to produce hydrogen

2.3.1 Pyrolysis

Pyrolysis is the thermal decomposition processes conducted at temperatures in the range 370 – 550 °C, in which the organic materials (such as biomass, plastic and solid waste) are converted by heat in the absence of oxygen. The process produces three products: gas (syngas), pyrolysis liquid (bio-oil) and leaves a solid residue (charcoal). Valuable gases, such as H_2, CO, CH_4, and CO_2 from pyrolysis can be applied in many application such as chemical synthesis, creating electricity and high efficiency combustion systems [23]. Ni et al. [24], investigated the effect of type of catalyst, temperature, heating rate and residence time on hydrogen gas production in the pyrolysis process. The results revealed that high hydrogen yield can be observed at high heating rate and long contact time. The similar results of the products yield have also been found in biomass steam gasification [25]. Pyrolysis could be further divided

into two types: slow pyrolysis and fast pyrolysis. In case of slow pyrolysis, the former takes several hours to complete and produces biochar as the main product. While, the latter is carried out at a high temperature (450 – 550 ºC) in the absence of oxygen. The main products produced from fast pyrolysis are gas (20%), liquid (60%) and biochar (20%) as following equations (Equations 2.1 and 2.2 [26]):

$$C_nH_m \longrightarrow nC + 1/2mH_2 \qquad\qquad\qquad (2.1)$$

$$Biomass + heat \longrightarrow H_2 + CO + CH_4 + liquid \text{ and solid products} \qquad (2.2)$$
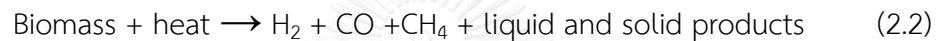
According to Garcia et al.[25] Ni metal has been widely used in biomass pyrolysis, because of its good physical and chemical properties. Dolomite represents as a promising catalyst in biomass pyrolysis because it is cheap and readily available source in acidic soil [27]. Zang et al. [28] used a fluidized bed reactor for investigation of catalytic fast pyrolysis of corncob and the performance of the catalyst was compared to non-catalyst. The results showed that the yield of uncondensed gas, coke and water increased, whereas the yield of liquid and char decreased in the presence of the catalyst. The suitable conditions in term of liquid yield (56.8 %) were found to be at reaction temperature of 550 ºC and feed flow rate of 3.4 L/min.

2.3.2 Biomass gasification

Biomass gasification as an alternative process of converting biomass into a gaseous combustible gas through a sequence of thermo-chemical reactions that has

the potential to decrease CO_2 emissions. The gasification has been considered as a technology for changing of biomass, agriculture waste, organic wastes, lignocellulose residues into valuable gas product [29]. In the process, air and steam are also employed to minimize the energy cost by partial oxidation [30]. Direct gasification at low temperature can be conducted in many reactors such as fluidized-bed reactor, fixed-bed reactor, and circulating fluidized-bed reactor [26].

Chang et al. [30], reported that gas and hydrogen yields were influenced by reaction temperature. The increase of reaction temperature could result in increasing the yield of gas and hydrogen. Xie et al. [31] studied the production of syngas from two-stage method of biomass catalytic pyrolysis and gasification. They found that that the gasification process need a higher temperature than the pyrolysis process to obtain high syngas yield. Nipattummakul et al. [32] studied the production of syngas from oil palm trunk waste steam gasification. They found that increasing steam flow rate led to decrease the time duration of gasification as well as increase hydrogen yield reduced. Lv et al. [33] investigated the production of syngas by gasification of pine sawdust. They found that the highest gas yield of 2.41 Nm^3/kg could be obtained at 850 °C.

2.3.3 Partial oxidation

Partial oxidation is an exothermic process conducted by thermal or catalytic partial oxidation [34]. The general form of partial oxidation is:

$$CH_4 + 1/2O_2 \longrightarrow CO + 2H_2 \quad [\Delta H = -247 \text{ kJ/mol}] \qquad (2.3)$$

$$CH_4 + 2O_2 \longrightarrow CO_2 + 2H_2O \quad [\Delta H = -801 \text{ kJ/mol}] \qquad (2.4)$$
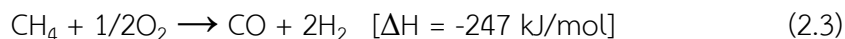
Thermal partial oxidation (TPOX) is usually conducted at high temperatures (1200 °C or above) and in the absence of a catalyst. Thermal partial oxidation has an advantage over catalytic partial oxidation due to do not need to be removed sulfur compounds from the reaction. While, catalytic partial oxidation can be operated at mild temperature. In catalytic partial oxidation (CPOX), catalysts is used to reduce the reaction temperature to around 800 – 900 °C, but need to remove sulfur compounds which poisons the catalyst, which led to the deactivation of the catalyst [35].

2.3.4 Steam reforming

Steam reforming is currently the most effective processes for hydrogen and syngas production [36]. Steam reforming is the catalytic reaction of hydrocarbons or oxygenated hydrocarbons with steam to produce CO and H_2. Water gas shift reaction (WGS) and the methanation reaction are the side reaction that usually occurs during steam reforming. Steam reforming, WGS and methanation reaction strongly depend on reaction conditions and catalyst used. Steam reforming, methanation and WGS can be shown as below:

$$\text{Steam reforming} \quad : C_nH_m + nH_2O \longrightarrow nCO + (n+m/2)H_2 \qquad (2.5)$$

$$\text{Methanation} \quad : CO + 3H_2 \longrightarrow CH_4 + H_2O \qquad (2.6)$$

WGS $\qquad$: $CO + H_2O \longrightarrow CO_2 + H_2$ $\qquad$ (2.7)
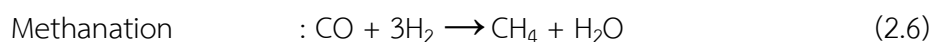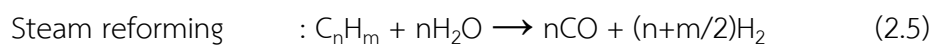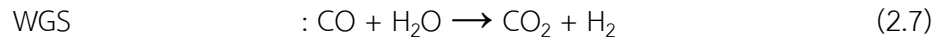
Steam reforming reaction is endothermic reaction that must be carried out at high temperature between 300 and 800 °C and low pressure [37]. In contrast, WGS and methanation are exothermic reaction. At high temperature, WGS would shift toward CO and H_2O (reverse water gas shift reaction). H_2 and CO_x selectivity greatly depend on the catalysts and operating conditions.
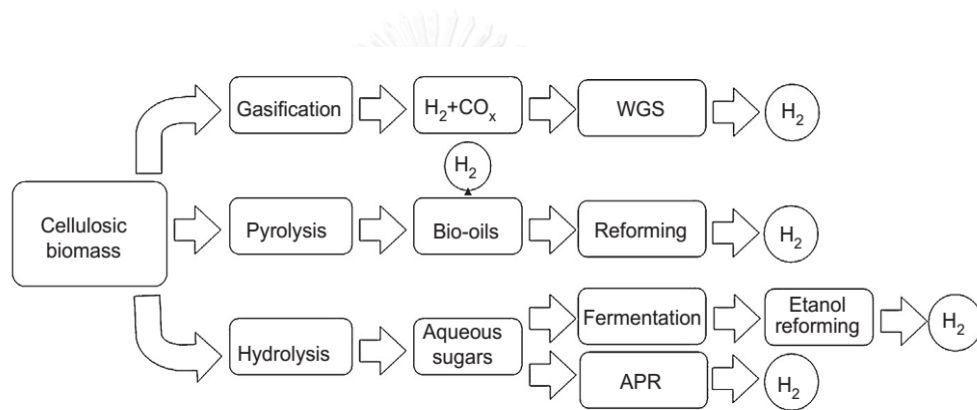
Figure 2.3 Simple flow diagram of hydrogen gas production from the biomass

2.4 Ethanol steam reforming

Ethanol repents one of the most attractive sources for hydrogen and syngas production because it is considered as a renewable source. Ethanol can obtained from the fermentation of biomass such as corn, sugar cane, wood pellets, wheat crops, waste materials from agricultural residues and municipal solid as shown in **Figure 2.3**. Ethanol is considered as the most abundant and easy to handle. Therefore, ethanol

steam reforming appears to be an interesting alternative for the hydrogen gas production [38]. The overall ethanol steam reforming reaction is shown below:

Ethanol steam reforming: $CH_3CH_2OH + 3H_2O \longrightarrow 2CO_2 + 6H_2$ (2.8)
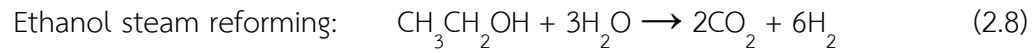
It is obvious that 6 mol of hydrogen are produced from 1 mol of ethanol fed. CO_2 is also the main product produced from this reaction. However, ethanol steam reforming is very complex reaction and several reactions may take place during ethanol steam reforming, depending on operating conditions and the catalytic system used. The possible reactions taking place in ethanol steam reforming reaction could be summarized as follows [39]:

Dehydration: $\quad$ $CH_3CH_2OH \longrightarrow CH_2CH_2 + H_2O$ $\hfill$ (2.9)

Polymerization: $\quad$ $CH_2CH_2 \longrightarrow coke$ $\hfill$ (2.10)

Decomposition: $\quad$ $CH_3CH_2OH \longrightarrow CH_4 + CO + H_2$ $\hfill$ (2.11)

$\quad$ $2CH_3CH_2OH \longrightarrow CH_3COCH_3 + CO + 3H_2$ $\hfill$ (2.12)

Methane steam reforming: $\quad$ $CH_4 + 2H_2O \longrightarrow CO_2 + 4H_2$ $\hfill$ (2.13)

Dehydrogenation: $\quad$ $CH_3CH_2OH \longrightarrow CH_3CHO + H_2$ $\hfill$ (2.14)

Decarbonylation: $\quad$ $CH_3CHO \longrightarrow CH_4 + CO$ $\hfill$ (2.15)

Acetaldehyde steam reforming: $CH_3CHO + H_2O \longrightarrow CO + 3H_2$ $\hfill$ (2.16)

Acetone steam reforming: $\quad$ $CH_3COCH_3 + 3H_2O \longrightarrow 3CO + 6H_2$ $\hfill$ (2.17)

Water gas shift: $\quad$ $CO + H_2O \longrightarrow CO_2 + H_2$ $\hfill$ (2.18)

Methanation: $\quad$ $CO + 3H_2 \longrightarrow CH_4 + H_2O$ $\hfill$ (2.19)

$\quad$ $CO_2 + 4H_2 \longrightarrow CH_4 + 2H_2O$ $\hfill$ (2.20)

Methane decomposition: $\quad$ $CH_4 \longrightarrow C + 2H_2$ $\hfill$ (2.21)

Boudouard reaction: $\quad$ $2CO \longrightarrow CO_2 + C$ $\hfill$ (2.22)

Oxidation: $\quad$ $CH_3CH_2OH + H_2O \longrightarrow CH_3COOH + 2H_2$ $\hfill$ (2.23)

Acetic acid steam reforming: $CH_3COOH + 2H_2O \longrightarrow 2CO_2 + 4H_2$ $\hfill$ (2.24)

Ethene is an undesirable product and well-known as a precursor for carbon formation. It can be produced from dehydration reaction. Acetone is another by-product which usually forms at reaction temperatures below 500 °C.

2.4.1 Reaction mechanism

The reaction mechanism of ethanol steam reforming has been widely discussed in the literature and different reaction pathways for ethanol steam reforming are presented in **Figure 2.4** The most acceptable pathway reaction mechanism for ethanol steam reforming is based on two main pathways: (2.9) dehydration to ethylene and (2.14) dehydrogenation to acetaldehyde.

Acetaldehyde then decomposes to carbon monoxide and methane. Carbon monoxide can further react with water to produce CO_2 and H_2 (WGS). Methane reforming can also promote the formation of hydrogen. In addition, dehydration to ethylene is the way to form undesired product, coke. Coke can lead to catalyst deactivation as well as blocked or constrained flow through the reactor [37, 39].
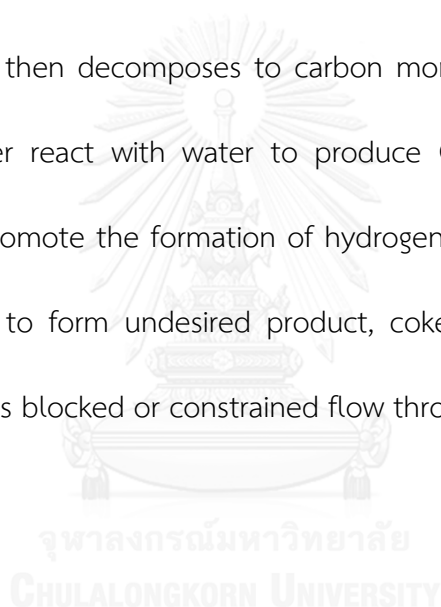
(a)
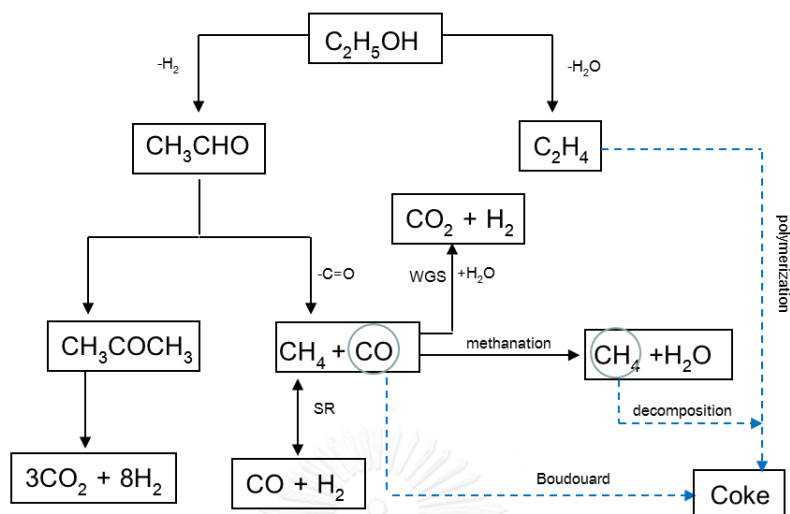
(b)
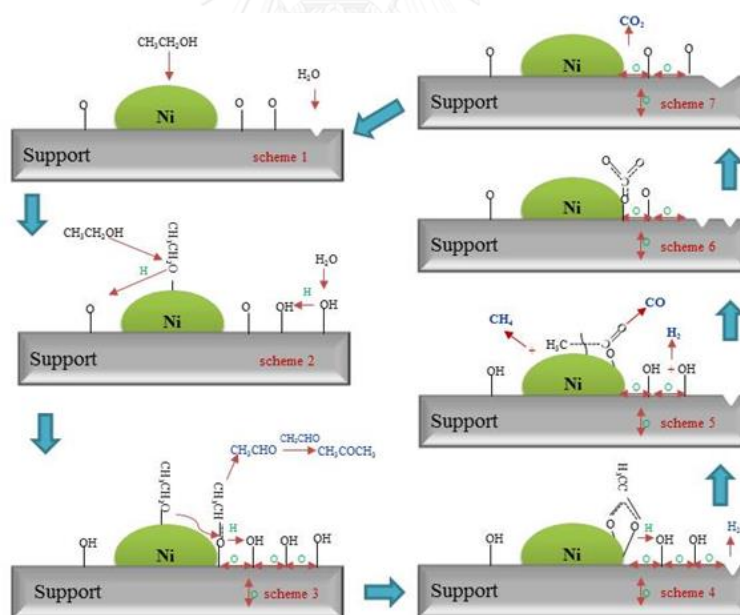
Figure 2.4 (a) The different reaction pathways for ethanol steam reforming and (b) reaction mechanism of ethanol steam reforming over Ni-based catalyst **[40]**

2.4.2 The operating parameters controlling selectivity for ethanol steam reforming

The influence several factors on the efficiency of ethanol steam reforming including reaction temperature, water-to-ethanol ratio and feed flow rate as well as the nature of the catalyst. The effect of reaction conditions on ethanol conversion and the product distributions has been studied in the literature and it will be now briefly described.

2.4.2.1 Temperature

Ethanol steam reforming is like conventional steam reforming, endothermic and thermodynamically favored at high temperature. Therefore, ethanol conversion and selectivity of product are controlled mainly by thermodynamics. The calculation of the thermodynamic equilibrium composition out of ethanol steam reforming is illustrated in **Figure 2.5**. It is clear that the major products are hydrogen, CO, CO_2, and methane. The production of methane is favored at low temperature due to methanation reaction. In contrast, the yield of CH_4 decreases at higher temperature because the reverse of methanation reaction becomes favorable, leading to increase H_2 yield [41, 42].
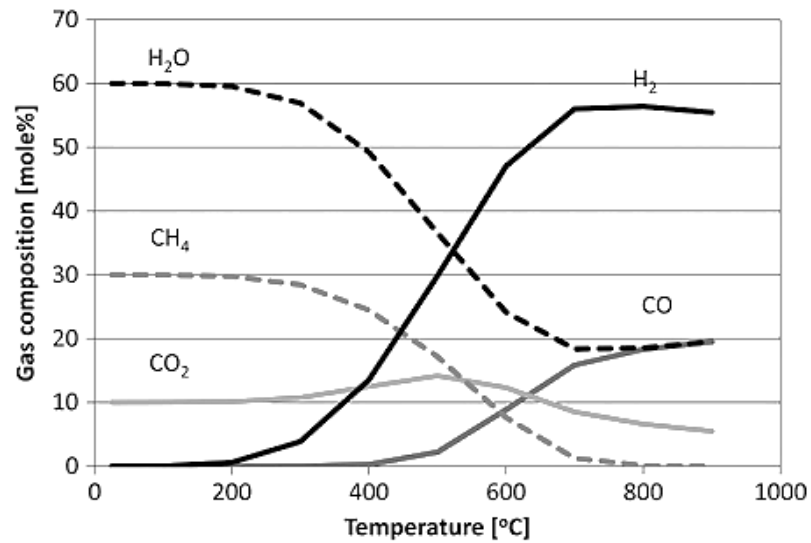
Figure 2.5 Influence of reaction temperature on product composition in ethanol steam reforming at atmospheric pressure S/C of 1.5 **[41]**

2.4.2.2 Steam-to-carbon ratio (S/C)

Steam-to-carbon ratio also affects ethanol conversion and selectivity of product, especially hydrogen yield. The ethanol steam reforming reaction has been conducted using steam-to-carbon ratios ranging from 1 to 15. An increase in the amount of water is generally found to increase the conversion of ethanol. The effects of water-to-ethanol ratio and the pressure are shown in **Figure 2.6**. It is seen that increasing steam-to-carbon ratio will increase hydrogen yield and CO_2, while CO formation decreased. This suggested that the increase of steam-to-carbon ratio lead to increase ethanol reforming reaction and/or the WGS reaction. It has been reported in literature that the rates of formation of by-product such as ethylene and

acetaldehyde could be reduced by increasing steam-to-carbon ratio because the acetaldehyde decomposition reaction is favored a high amount of water. However, the adding high amounts of water could lead to increase operating energy costs for evaporating of water [39].
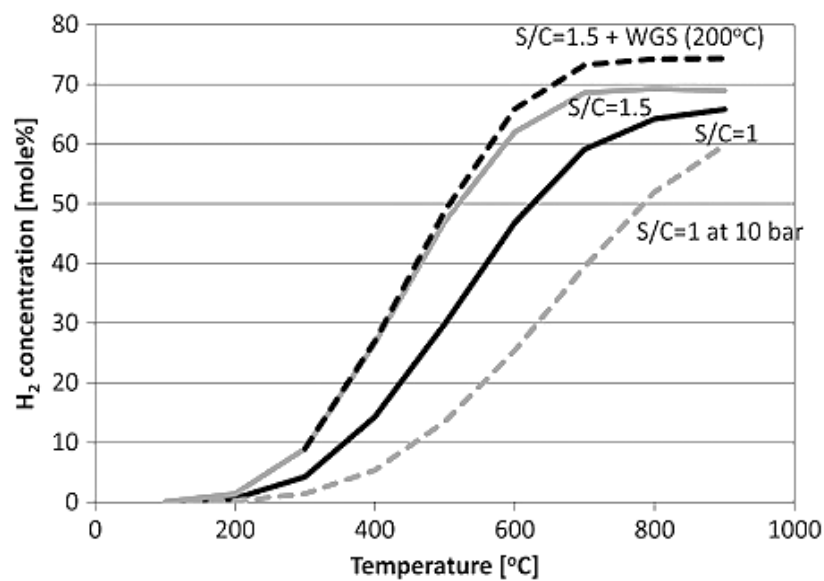
Figure 2.6 Influence of steam-to-carbon ratio and pressure on the equilibrium H_2 concentration **[39]**

2.4.2.3 Feed flow rate

Conversion and product distribution are also influenced by feed flow rate. The effect of feed flow rate on ethanol conversion and selectivity of product has been investigated extensively in the literature. A decreasing in flow rate is found to increase H_2 yield and ethanol conversion which attribute to the increase of the contact time. By increasing the feed flow rate, ethanol conversion decreases. This indicates that the

increase of feed can result in increasing contact time. However, the production of undesirable CH_4 also increases with the increase in the flow rate [40].

2.5   Acetic acid steam reforming

Acetic acid represents as a promising alternative platform chemical from biomass. It is the major part of components in bio-oil and noninflammable unlike ethanol. Therefore, it has been chosen as a typical model for study steam reforming for hydrogen gas production [42]. Acetic acid steam reforming offers much information for developing efficient catalysts and providing suitable conditions for hydrogen production from real bio-oil steam reforming. The overall acetic acid steam reforming reaction may be demonstrated as following [43]:

$$\text{Acetic acid steam reforming:} \quad CH_3COOH + 2H_2O \longrightarrow 2CO_2 + 4H_2 \quad (2.25)$$

Acetic acid steam reforming is an endothermic reaction, so it requires a high temperature. Several reactions occur simultaneously during acetic acid steam reforming depending on the catalysts used and reaction conditions. The possible reactions taking place in acetic steam reforming reaction could be summarized as follows [43]:

Ketonization: $2CH_3COOH \longrightarrow CH_3COCH_3 + CO_2 + H_2O$ (2.26)

Acetone steam reforming: $CH_3COCH_3 + 2H_2O \longrightarrow 3CO + 5H_2$ (2.27)

Decomposition 1: $CH_3COOH \longrightarrow CH_4 + CO_2$ (2.28)

Decomposition 2: $CH_3COOH \longrightarrow 2H_2 + CO_2 + C$ (2.29)

Dehydration: $CH_3COOH \longrightarrow CH_2CO + H_2O$ (2.30)

Ketene steam reforming: $CH_2CO + H_2O \longrightarrow 2CO + 2H_2$ (2.31)

Ketene coupling: $2CH_2CO \longrightarrow C_2H_4 + 2CO$ (2.32)

WGS: $CO + H_2O \longrightarrow CO_2 + H_2$ (2.33)

Methanation: $CO + 3H_2 \longrightarrow CH_4 + H_2O$ (2.34)

$CO_2 + 4H_2 \longrightarrow CH_4 + 2H_2O$ (2.35)
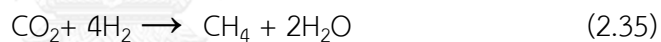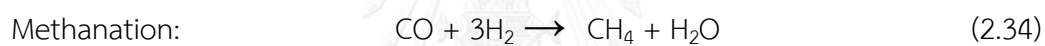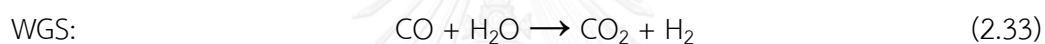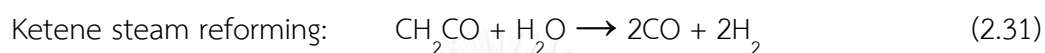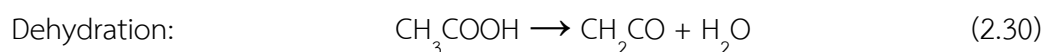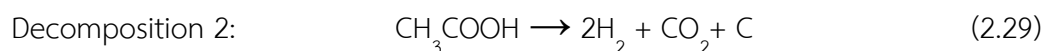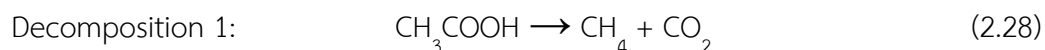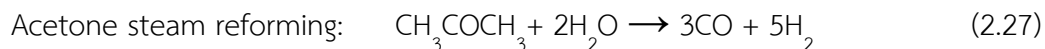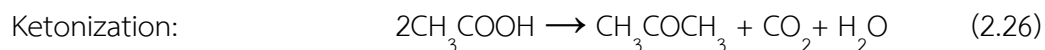
Experimental studies on acetic acid steam reforming are generally conducted at temperatures. The complete conversion is achieved at temperature between 400 and 800 °C, depending on temperature, pressure, steam-to-carbon ratio and a catalyst. The equilibrium product composition in acetic acid steam reforming is showed in **Figure 2.7**. It is observed that the highest hydrogen yield can achieve at 600 °C. However, further increase of temperature tends to reduce hydrogen yield due to the unfavorable equilibrium of WGS reaction.
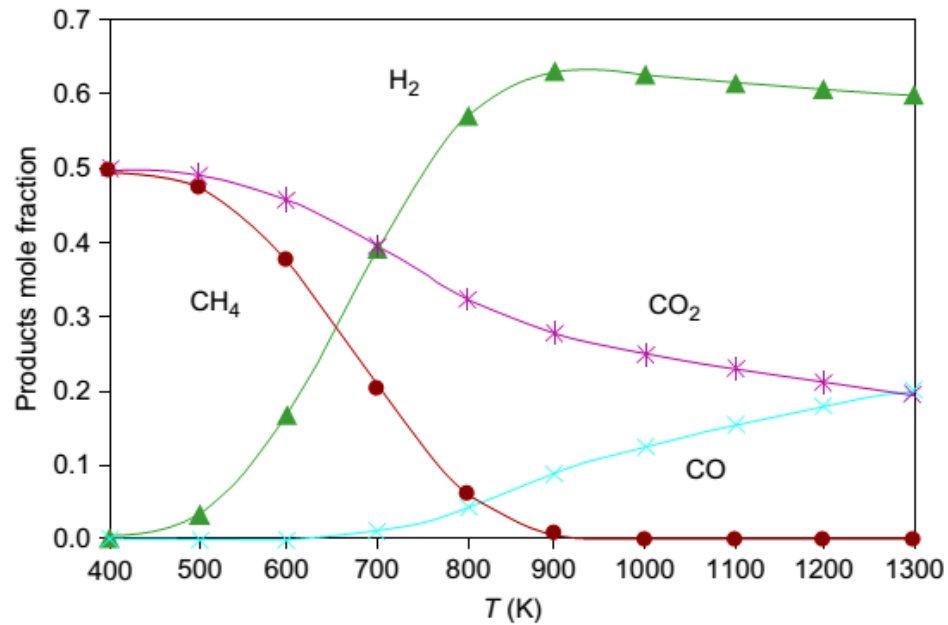
Figure 2.7 Equilibrium product compositions as function of the temperature in acetic acid steam reforming at 1 bar and S/C-ratio of 3 **[44]**

2.5.1 Reaction mechanism

The mechanism of acetic acid steam reforming reaction proposed by Z. Li et al.[45] is shown in **Figure 2.7**. The dissociation of acetic acid occurred though the two main pathways. Pathway I was the C–O cleavage to produce the acyl species. The decomposition of acyl species led to form CO* and methyl (where * denotes a vacant site). Pathway II represented H–O cleavage to form the acetate species [46]. The decomposition of acetate species resulted in forming adsorbed methyl and CO_2. Methyl species was a significant intermediate in this process. The formation of gaseous products, CH_4, CO, CO_2 and acetone can be obtained via methyl species.

(a)
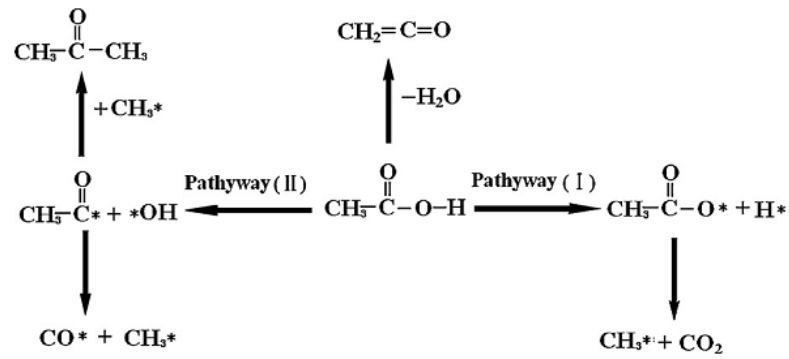
(b)
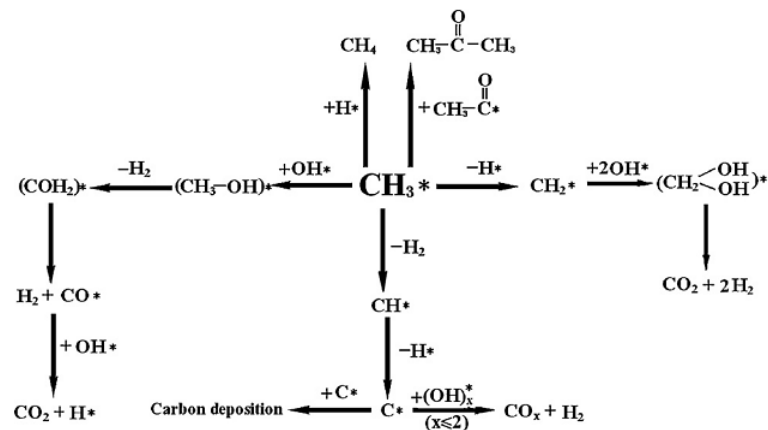
Figure 2.8 Mechanism of acetic acid steam reforming according to Z. Li et al **[45]**

2.6   Catalysts used for steam reforming

Catalyst plays a significant factor for ethanol conversion and product distribution. Different types of catalysts can activate different reaction paths. Therefore, the selection of the appropriate catalyst is extremely important.

2.6.1 Oxide catalysts

Llorca et al. [47] studied ethanol steam reforming by using different oxide catalysts such as MgO, γ-Al_2O_3, SiO_2, ZnO. The results showed that highly effective production of hydrogen was observed in ZnO catalyst. The use of ZnO catalyst significantly decreased the CO content (CO is a poison for the catalysts) of the gas stream to very low contents. The decomposition of ethanol to acetone, the ethanol steam reforming and WGS reaction were the main reactions. γ-Al_2O_3 is an acidic catalyst which favors dehydration of ethanol to form ethylene. In case of MgO, it is a basic catalyst and favored dehydrogenation of ethanol.

2.6.2 Transition metal catalysts

Many catalysts including transition metals (i.e., Co, Ni, Fe, and Cu) and noble metals (Pt, Pd, Ru, Rh and Ir) have been tested in reforming reaction. Among metal catalysts, so far, Ni has been commonly studied because of its high activity for breaking C-C bond and the favorable commercial aspects of Ni: low cost and widely available. However, the drawback of Ni catalyst is the rapid deactivation by the carbon or coke formation on the catalyst surface and sintering due to high temperatures required, leading to short catalyst lifetimes [48, 49]. Several approaches have been developed to resist the formation of carbon on active site during steam reforming. The addition of small amounts of alkali metals (Ca, Mg and K) or other metals (La, Co, Ce and Zr)

into Ni catalysts can suppress carbon deposition by promoting the carbon gasification [39, 42]. The addition of a basic material like an alkaline or alkaline earth mineral has been found to improve coking resistance by activating water. This lead to form OH- or O-species. Both OH- or O-species can react with the carbon on the surface of catalyst to form CO as shown in **Figure 2.9.** Furthermore, the addition of alkali could prevent sintering since alkali could decrease metal particles. Modifying Ni surfaces with a second metal, such as La, Co, Ce and Zr via alloy formation may adjust the C-C cleavage property to control the generation of coke precursors [50, 51].
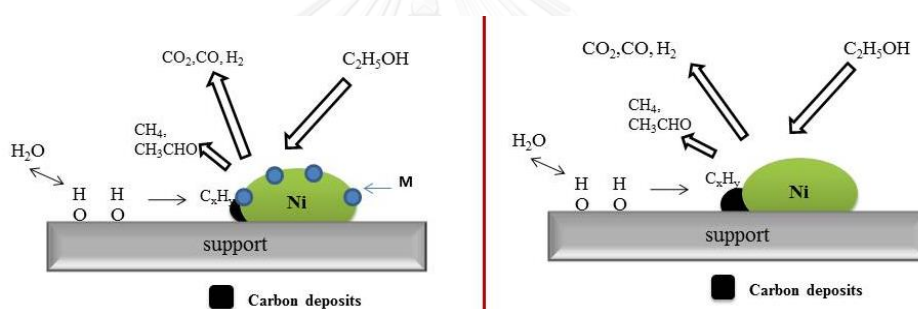
Figure 2.9 Schematic depiction of adding small amounts of M to supported Ni catalyst

2.7   Catalyst deactivation

Catalyst deactivation is the main problems in steam reforming and has a significant role in developing new catalysts for producing hydrogen. In general, carbon deposition and metal sintering are the two main problems of catalyst deactivation during steam reforming reaction [37]. In the following section, the reasons of the deactivation of catalyst in ethanol steam reforming will be discussed.

2.7.1 Carbon deposition

Several reactions may contribute to carbon deposition in ethanol steam reforming including (i) ethanol dehydration to ethylene which can polymerize to coke, (ii) acetone aldol condensation (reaction 2.37), (iii) Boudouard reaction, (iv) reverse of carbon gasification; and (v) methane and ethylene decomposition [52].

Polymerization: $\quad\quad\quad\quad CH_2CH_2 \longrightarrow coke$ $\quad\quad\quad\quad\quad$ (2.36)

Acetone: $\quad\quad\quad\quad 2CH_3COCH_3 \longrightarrow (CH_3)_2C(OH)CH_2COCH_3$

$\quad\quad\quad\quad\quad\quad\quad\quad \longrightarrow (CH_3)_2C = CHCOCH_3 + H_2O$ $\quad\quad$ (2.37)

Boudouard reaction: $\quad\quad 2CO \longrightarrow CO_2 + C$ $\quad\quad\quad\quad\quad\quad$ (2.38)

Reverse carbon gasification: $\quad CO + H_2 \longrightarrow C + H_2O$ $\quad\quad\quad$ (2.39)

Methane decomposition: $\quad CH_4 \longrightarrow C + 2H_2$ $\quad\quad\quad\quad\quad$ (2.40)

Ethene decomposition: $\quad CH_2CH_2 \longrightarrow 2C + 2H_2$ $\quad\quad\quad\quad$ (2.41)
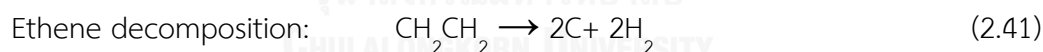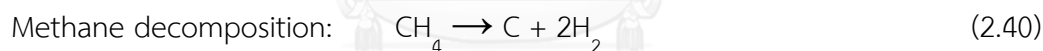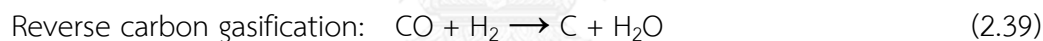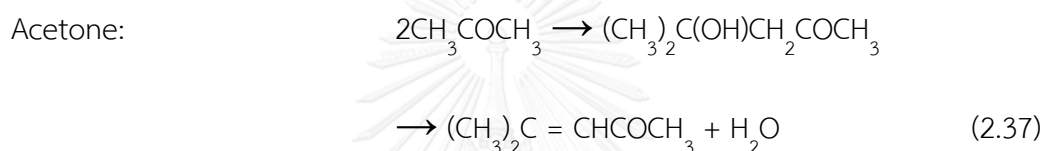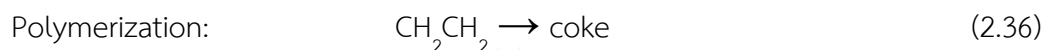
Carbon deposition rate are dependent on reaction conditions and the catalyst used. The Boudouard reaction and reverse carbon gasification are favored at a low reaction temperature while higher temperatures favor the carbon formation via the decomposition of hydrocarbons. Carbon deposition over Ni has been well-studied in the literature [53, 54]. According to these studies, there were three main types of carbon formed on Ni during steam reforming process: amorphous, filamentous and

encapsulating carbon (**Figure 2.10**). Amorphous carbon formed at low temperatures

between 200 – 500 ºC, while the high formation of filamentous carbon was favored at

higher temperature [44].
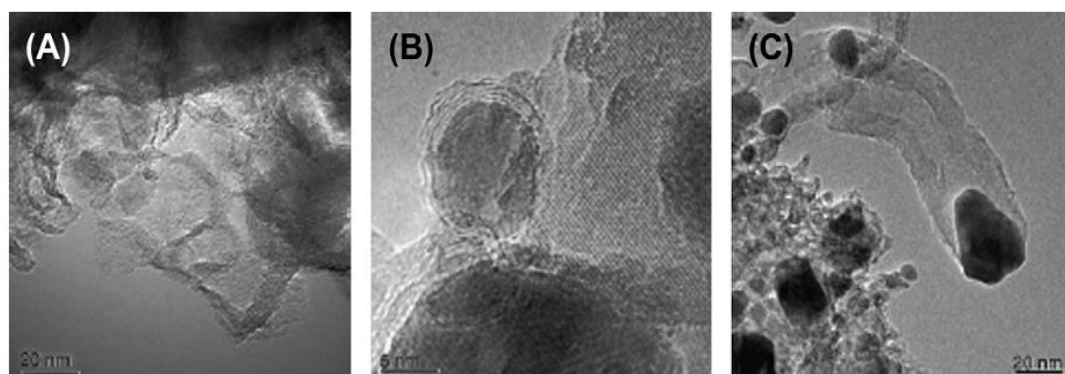
Figure 2.10 SEM images of different types of carbon formed over a Ni/MgAl$_2$O$_4$ catalyst (A) amorphous, (B) encapsulating, and (C) filamentous carbon. **[55]**

The growth of filamentous carbon is believed to occur as carbon species diffuse

into the Ni particles until the solution and form nickel carbide (Ni-C). The Ni-C is

metastable active carbide between nickel metal and graphite, which transform into

encapsulating nickel particle [56]. Carbon will deposit on the surface of nickel until the

concentration of carbon is high and enough to push Ni off the surface of support to

form CNTs or CNFs as shown in **Figure 2.11**. The formation of CNFs and CNTs occur

simultaneously during reforming. As for CNFs, the nucleation occurs over the whole of

metal-support interface thought diffusion resulting in the formation of a full fiber

(**Figure 2.11(b)**). The formation of CNFs generally occurs at low temperature when

nucleation rate is slow and carbon atoms could reach the whole interface of metal

and support. As for CNTs, the nucleation is restricted surrounding area of the gas-metal

interface. The growth of CNTs is believed to occur at high temperature when the

nucleation rate is high. The nucleation occurs before entire interface of metal and

support, which lead to form hollow fibers [57].

(a)

(b)
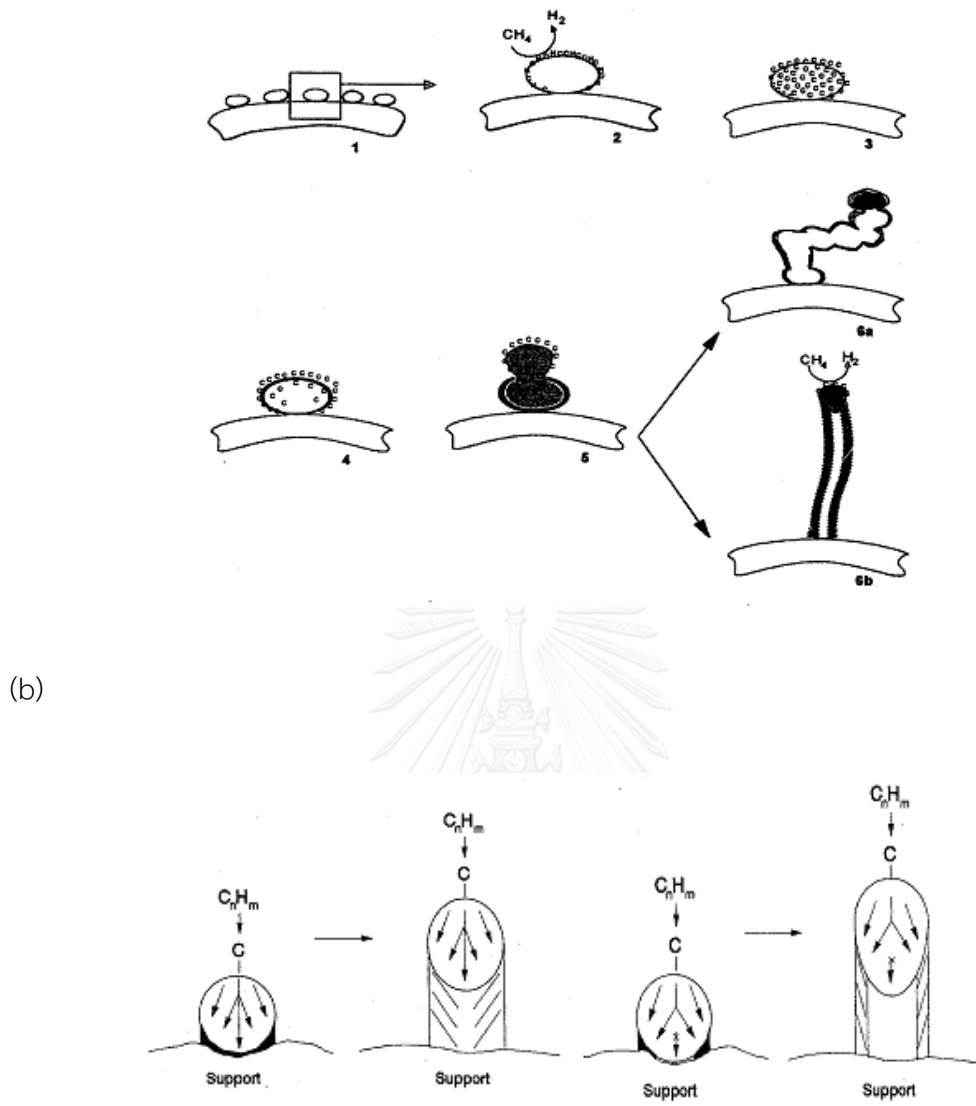
Figure 2.11 (a) The mechanism for the formation of CNTs and CNFs over a supported catalyst (b) the formation of CNFs (left) and CNTs (right) **[57]**

The mechanism for growth of encapsulating carbon is shown in **Figure 2.12**. The formation of encapsulating carbon occurs though the graphitic layers formed surround the entire surface of metal particle. The formation of encapsulating carbon can result in the catalyst deactivation. In contrast, the formation of filamentous carbon

metal catalyst would remain active during reforming reaction because the catalyst is on the top of the filament which is still accessible to reactants and gas-phase intermediates [58].
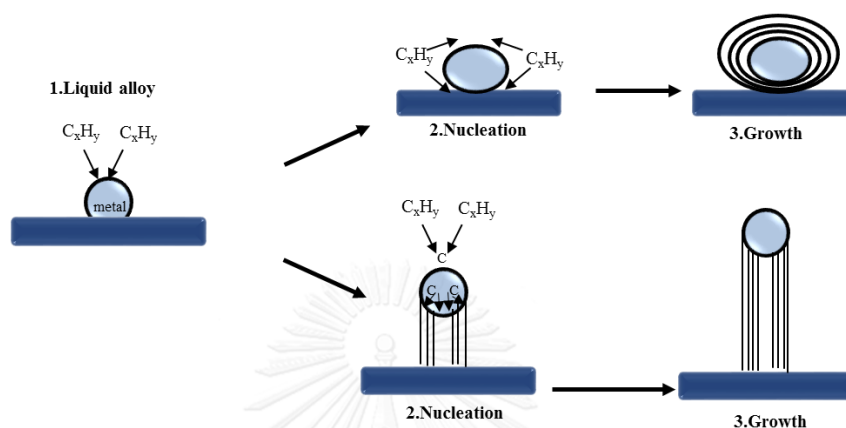
Figure 2.12 Schematic presentation of growth procedure of encapsulating and filamentous carbon **[58]**

2.7.2 Metal sintering

Metal sintering can play another major role in catalyst deactivation. Metal sintering can result in losses in the metal active surface area since the small metal active agglomerates into larger ones [53]. Sintering is affected by several factors such as temperature, composition of the gas over the catalyst, structure and composition of the catalyst support, and as metal-support interactions. The temperature and the atmosphere in contact is the most important parameters with the catalyst for sintering. The presence of high temperature would lead to accelerate substantial sintering [52, 53]. The preparation method is an important factor for determining catalytic activity

and stability during steam reforming reaction because the preparation method controls the metal particle size. Therefore, the suitable method for catalyst preparation should provide the formation of catalyst small particle size and high metal dispersion. Characteristics of the support are also responsible for the stabilization of metal particles. To avoid sintering, the support selected should be strong enough interaction with catalyst particle for stabilizing a small metal particle size during steam reforming reaction [37].

2.8   Support catalysts

The support in steam reforming should have high surface and strong enough interaction to promote metal dispersion and to stabilize a small metal particle size, which provides resistance against carbon formation. In addition, it should promote the migration of surface OH groups toward metal, which react with surface carbon species to form CO, CO_2 and H_2.

2.8.1 Alumina (Al_2O_3)

Alumina is one of the supports most commonly used as catalyst supports. This is largely because it is relatively low cost as well as has high surface areas. Unfortunately, strong acidic property of Al_2O_3 easily promotes carbon deposition through the formation of ethylene intermediate, which is a serious problem for nickel-based catalysts [59, 60].

2.8.2 Silica (SiO$_2$)

Silica has been used in many fields these including use in whitewear and glass ceramics, as a desiccant, as well as being used as a catalyst support. Silica has been widely used as catalyst support in many reactions as it is inherently neutral acidity/basicity property, high specific surface area and excellent thermal stability [60]. Bej et al. [4] have demonstrated that the catalyst performance of Ni/SiO$_2$ depended on size and the morphology of active species. The Ni nanoparticles size of 9–15 nm was found to be effective for the steam reforming of methane. Moreover, the mesoporous structure of SiO$_2$ like SBA-15 and MCM-41 with large surface areas and well-defined structure has been recently studied as support in the SRE reaction in order to reduce the blockage of metal sites as well as pore blockage. Zhang et al. [11] studied the catalytic behavior of Ni/SBA-15 catalysts synthesize by the means of ammonia evaporation and impregnation in dry reforming of methane reaction and reported that Ni/SBA15 prepared by ammonia evaporation exhibited high metallic dispersion due to strong metal–support interactions in the channel, which lead to excellent resistance to coking. However, weak interaction between Ni and SiO$_2$ can easily promote metal aggregation, which is the key parameter for catalyst deactivation.

2.8.3 Carbon nanotubes (CNTs)

Carbon nanotube (CNTs) is another type of support that has been investigated a great deal for reforming process. The advantages of being unique tubular structure

and large specific surface areas significantly enhance the dispersion of the active sites, leading to achieve small particle. The CNTs can also efficiently promote electron transfer between metallic active sites and the support to the reactants as it consists of 36 grapheme layers, involving π-electron density [18].

The structure of CNTs is shown in **Figure 2.13**. The structure of CNTs is extremely open, high porosity and low tortuosity as compared with conventional porous support. These advantages can help to prevent mass transfer limitations [18, 61].
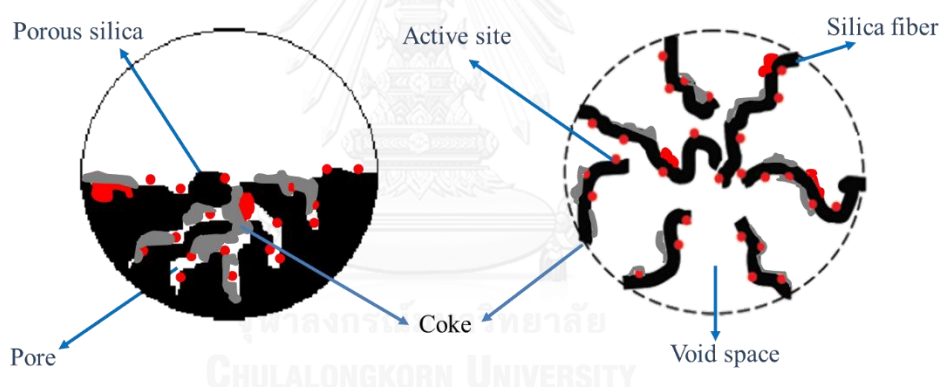
Figure 2.13 CNFs structure and conventional porous structured material **[61]**

CNTs are hydrophobic compounds and there were no any functional groups on the surface. To use CNTs for support catalyst, the surface properties of the CNTs need to be modified by oxidation treatment with acids. HNO_3 acid is commonly used in oxidation treatment. The treatment with HNO_3 acid lead to create oxygen- functional groups containing on the surface of CNTs as shown in **Figure 2.14**. The benefits of the

oxidized surface are (i) these polar functional groups can fix small metal particles, (ii) the presence of the polar functional groups enlarges the ability of polar solvent or water to maintain contact with the surface of CNTs and (iii) the treatment can eliminate any residual metal which is used to form the CNTs [61, 62].
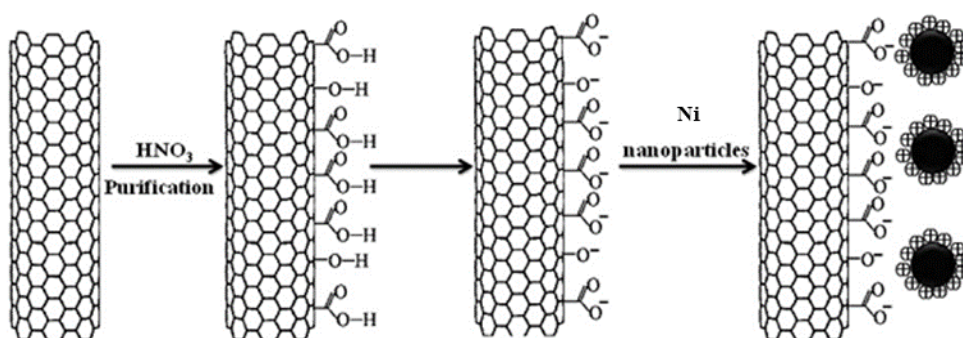
Figure 2.14 The process for Fe nanoparticles decorating on MWCNTs **[62]**

CNTs can be also applied as a part of a composite. The formation of CNTs composite lead to extend the application of CNTs, including modern materials and support catalyst in liquid and gas phase processes [63]. Recently, Chernyak et al. [20] have developed hybrid composites which comprised of CNTs and conventional porous Al_2O_3 as an alternative support for cobalt catalyst in Fischer-Tropsch synthesis and they found that the hybrid composite catalysts presented remarkable catalytic activity and stability as well as outperformed other supports Carrero et al. [64] demonstrated that the used Ni/SiO_2 catalysts were predominantly covered with CNTs and Ni metal embedded on the top of carbon nanotubes.

2.9 Electrospinning

Electrospinning technique represents as an effective technique for production of fibers from various polymeric liquids or sol-gel precursors solution by application of an electrostatic force. The diameter of fibers obtained from this technique is in ranging from a few nanometers to a few micrometers. The electrospinning setup comprises a syringe pump, a high voltage source, and a collector as shown in **Figure 2.15**. Drop of polymer solution at a needle tip is directly connected with the electrode. The solution is then applied an electric field using the high-voltage source to overcome the surface tension of polymer solution, resulting in the initiation of a jet, which is subsequently stretched to form a continuous ultrathin fiber. As the liquid jet moves to the collector, solvents with high vapor pressures evaporate, leading to a decrease in jet diameter and velocity. The properties of the materials and the electrospinning parameters such as the solution concentration, viscosity, applied voltage, and tip-to-collector distance (TCD) are the main factors that control the morphologies and textural properties of nanofibers [65, 66].
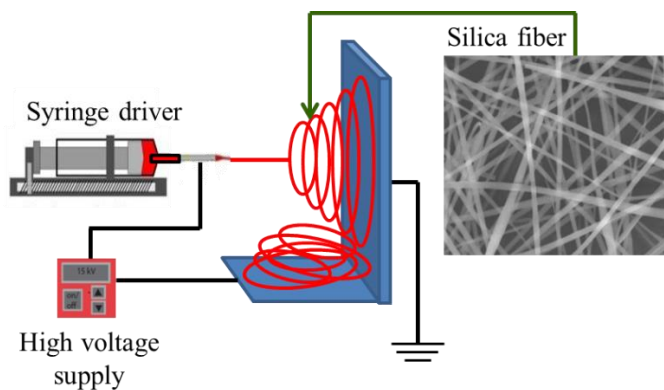
Figure 2.15 Schematic presentation of fiber formation by electrospinning

The sol-gel method is a wet-chemical technique used for the fabrication of polymer solution for electrospinning. This method involves hydrolysis of liquid precursors and formation of colloidal sols. Metal alkoxides or metal chlorides are typical precursors in sol-gel preparation. Hydrolysis of the precursors following by polycondensation reactions lead to form a colloid, as in the following reaction [67]:

Hydrolysis: $\quad\quad\quad\quad\quad$ -M-O + H$_2$O $\quad\longrightarrow$ -M-OH + ROH $\quad$ (2.42)

Alcohol condensation: $\quad$ -M-OH + XO-M- $\longrightarrow$ -M-O-M- + XOH $\quad$ (2.43)

Water condensation: $\quad$ M-OH + HO-M $\longrightarrow$ -M-O-M- + H$_2$O $\quad$ (2.44)
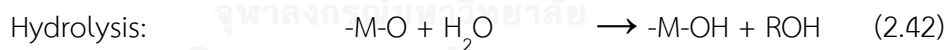
X can either be H or R (an alkyl goup).

2.10 Literature reviews

Batista *et al.* [68] investigated the catalytic activity and stability in ethanol steam reforming of cobalt supported on different supports, Al$_2$O$_3$, SiO$_2$, and MgO. The

effect of reaction temperature in the range 400 to 550 °C was also studied. The results showed that cobalt supported on alumina favored promote dehydration of ethanol to form ethylene due to the Lewis acid properties of alumina. In case of Co/SiO_2 and Co/MgO catalysts gave the highest quantity of methane.

Seelam *et al*. [69] compared the use of catalysts (Ni, Co, Pt and Rh) supported on carbon nanotubes (CNTs) and on Al2O3 in ethanol steam reforming The results showed that Co/CNTs and Ni/CNTs catalysts exhibited excellent catalytic performance. In case of Ni/CNTs, ethanol was almost full converted at reaction temperature of 400 °C. The low amount CO and CH_4 was observed in case of Co/CNTs because it promoted WGS and methane steam reforming.

Yong *et al*. [70] investigated Ni-based catalyst supported on a carbon nanofibers (Ni/CNFs) for the hydrogen production in bio-oil steam reforming at low temperature and compared the catalytic performance with Ni supported on alumina. Both catalysts were prepared by the homogeneous impregnation. The results revealed that small metal particles and high dispersion were found when used CNTs for support catalyst. Ni/CNFs exhibited relatively higher activity in bio-oil steam reforming as compared to Ni/Al_2O_3 catalyst. The maximum H_2 yield of 92.1% and carbon conversion of 94.7% were obtained at 550 °C on the 22 wt% Ni/CNFs catalyst.

The effect of different structural forms of $Ru/MgO/Al_2O_3$ such as pellets, ceramic monolith and ceramic foam on hydrogen production from bio oil steam

reforming was reported by Basagiannis *et al*. [71]. At high temperatures and low space velocities, all catalysts showed high activity and well selectivity. The pelleted catalyst exhibited the highest activity because the structure provided more efficient contact between active species and reactants. The use of MgO in the catalyst composition improved of O- and/or -OH anion activity on metal particles.

Seo *et al*. [72] reported the effect of the addition of second metals (Ni, Ce, La, Y, Cs, Fe, Co, and Mg) into mesoporous nickel–M–alumina aerogel catalysts (NiMAE) in steam reforming of natural gas (LNG). The results found that NiLaAE catalyst exhibited the smallest average nickel particles which resulted in high hydrogen yield. Furthermore, the high ability of facilitating heat and mass transfer between product in steam reforming of LNG, reactant and catalyst was obtained when added La into NiMAE catalyst.

Haasterecht *et al*. [73] explored stability and activity of different catalyst (Ni, Co, Cu and Pt) supported on carbon nano-fibers in the aqueous phase reforming of ethylene glycol. Pt/CNF, Ni/CNF and Co/CNF catalysts exhibited high ethylene glycol conversion. The Pt/CNF catalyst exhibited higher H_2 selectivity compared to Ni/CNF and Co/CNF since Pt/CNF catalyst promoted WGS reaction but Ni/CNF and Co/CNF promoted methanation reaction. On the other hand, low ethylene glycol conversion was found in case of the Cu/CNF catalyst. In case of Co/CNF catalyst, it showed rapid deactivation because of the formation of acids in liquid phase.

Silva *et al.* [74] studied the effect of cobalt particle size on catalyst stability in ethanol oxidative steam reforming reaction. In this study, an inert CNF material was used as a support for cobalt catalyst. They found that at 500 °C ethanol conversion was 85%. The lowest catalyst particle sizes seemed to easily deactivate because of oxidation of surface atoms, but the catalysts with large Co particle size (>4 nm) remained almost constant for the all the time studied.

Reubroycharoen *et al.* [17] prepared Ni catalyst supported on silica fiber by using the electrospinning. The average diameters of the fibers obtained from electrospinning were 1.28 μm - 930 nm. The Ni/silica fiber was applied in glycerol steam reforming for syngas production. The performance of the fiber catalyst was compared to a conventional Ni/SiO_2 porous catalyst. The Ni/SiO_2 fiber catalyst showed better Ni dispersion on the SiO_2 fiber when lower Ni loading percentage was applied. The activity of the fiber catalyst was higher than the Ni/SiO_2 porous catalyst as the fiber was easily reduced.

Bobadilla *et al.* [75] investigated the effect of different $NiSn/10MgO-15CeO_2-Al_2O_3$ catalyst structures (diluted powders, egg-shell pellets and monolithic catalysts) on the catalytic activity and selectivity of hydrogen in glycerol steam reforming. The results exhibited that at 1 h of experiment, all catalysts exhibited the similar activity and selectivity, however the catalyst in powder formed was rapidly deactivated. In

case of the monolith catalyst, the formation of carbon was not observed because of its strong interaction with catalyst.

GaO *et al.* [76] studied steam reforming of methanol by using La_2CuO_4 crystal nanofibers catalyst prepared by single-walled carbon nanotubes as templates and compared with the La_2CuO_4 bulk powder catalyst. The results showed that the La_2CuO_4 nanofiber exhibited higher methanol conversion, CO_2 selectivity and longtime stability than La_2CuO_4 bulk powder. The decomposition to CO and H_2 of the intermediates of HCO and H_2CO may be stabilized and prevented by oxygen vacancies and the trapped electron. While, in the case of bulk powder catalyst, the intermediate H_2COO will probably decompose to CO and H_2O. Around 100% of methanol conversion with the gaseous products H_2, CO_2 and CO was obtained in the low temperature of 140 °C.

Wang *et al.* [77] studied the effect of microstructure of fibrous NiO/CeO_2 nanocatalyst and gas flow rate on carbon formation in dry reforming of methane at 750 °C with a GHSV of 2.7×105 h^{-1}. The study finding showed that the strong interaction between NiO and CeO_2 support resulted in higher methane conversion and a decrease of the rate of carbon formation because oxygen species of CeO_2 support oxidized carbonaceous deposits on catalyst surface. Moreover, coke formation rate decreased through facilitating radical desorption by increasing the gas flow rate.

Hu *et al.* [78] studied the effect of different the molar ratio of Ni and Co catalysts and reaction conditions of on hydrogen production in acetic acid steam reforming. The molar ratios of Ni and Co of 0.25:1 revealed the highest activity. Ni catalyst exhibited high activity in breaking C–C bond, while Co had higher activity for WGS reactions than Ni. The optimum condition in term of hydrogen and acetic acid conversion was temperature of 673 K, LHSV of 5.1 h^{-1} and water to acetic acid ratio of 7.5:1. The maximum hydrogen yield was 96.3% and CO_2 selectivity was 98.1%. The use of bimetallic Ni–Co catalyst exhibited significant improve catalytic stability.

CHAPTER III

EXPERIMENTAL

3.1 Materials and reagents

Materials used in the study are listed in **Table 3.1**.

Table 3.1 List of chemicals and reagents

Chemicals	Source
Tetraethyl orthosilicate ($C_8H_{20}O_4Si$) 98.0%	Fluka
Hydrochloric acid (HCl) 37.0%	CARLO ERBA
Ethanol (C_2H_5OH) 99.9%	Merck
Acetic acid (CH_3COOH) 100%	Merck
Nickel nitrate hexahydrate $Ni(NO_3)_2.6H_2O$	Aldrich
1D silica support 20-40 mesh	Fuji Silysia
Nitrogen gas (99.99% purity)	Praxair
Hydrogen gas (99.99% purity)	Praxair
Standard synthesis gas 1% of $H_2/CO/CO_2/CH_4/C_2H_4/C_2H_6$ bal N_2	BOC scientific

3.2   Synthesis of Ni/silica fiber catalyst (NiSF)

NiSF catalyst was synthesized through the combination of sol-gel and electrospinning techniques following by conventional impregnation method [79].

SF was synthesized by sol–gel assisted electrospinning technique using tetraethyl orthosilicate (TEOS) as a Si source. First, 18 mL of TEOS was dissolved in 3 mL of deionized water (DI water) and stirred for 5 min, followed by adding 1 g of concentrated HCl. Then 9.4 mL of ethanol was added into the mixed solution under continuous stirring for additional 5 min. After that the solution was heated to 55 °C by water-bath under continuous stirring for approximately 30 min. Finally, the mixed solution was transferred into the disposable syringe equipped with 0.4 mm diameter needle. The electrospinning conditions used for synthesis of SF was a voltage of 15 kV, a feeding rate of 10 μL/h and the tip-to-collector distance (TCD) of 15 cm as presented in **Figure 3.1**. The obtained fibers were dried at 110 °C in an oven overnight and calcined at 500 °C for 2 h.
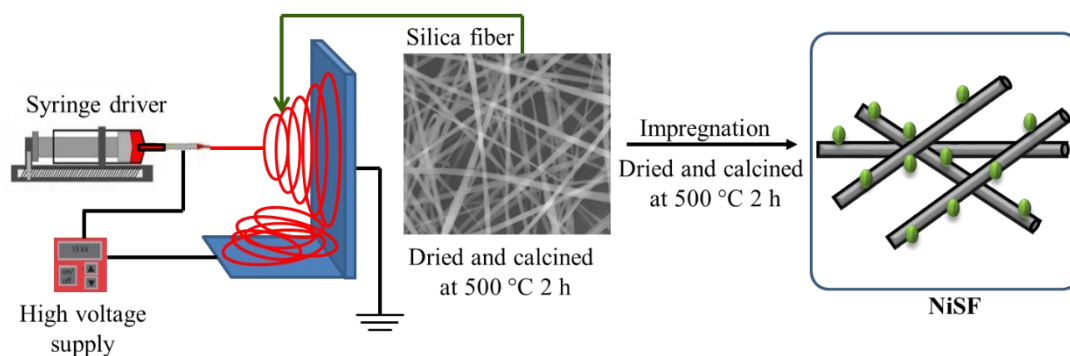
Figure 3.1 Synthesis scheme for NiSF catalyst

The NiSF catalyst with Ni loading of 10, 20 and 30 wt% was prepared by impregnation technique of using $Ni(NO_3)_2.6H_2O$ as a Ni precursor as shown in **Figure 3.1**. First, the $Ni(NO_3)_2.6H_2O$ was dissolved in DI water. The $Ni(NO_3)_2.6H_2O$ solution was impregnated onto SF. Afterwards, NiSF was obtained with dried at 110 °C overnight and calcined at 500 °C for 2 h. The NiSF catalysts with 10, 20 and 10 wt% were named as 10NiSF, 20NiSF and 30NiSF.

3.3   Catalytic performance of NiSF for co-production of hydrogen and carbon nanotubes-silica fiber (CNTs-SF-E) composite from ethanol steam reforming

The co-production of H_2 and CNTs was synthesized by ethanol steam reforming over NiSF catalyst. The catalytic performance of NiSF catalyst was conducted in a fixed-bed tube reactor as shown in **Figure. 3.2.** Before ethanol steam reforming, 0.2 g of the catalyst sample was reduced *in situ* with 10% H_2/N_2 at 400 °C for 1 h. The ethanol steam reforming was conducted at atmospheric pressure using nitrogen as carrier gas for 4 h. A water–ethanol mixture was fed into the reactor via an HPLC pump. The effects of Ni loading (10-30 wt%), space-time (W/F, 9, 12, 18, and 36 g_{cat}h/mol), reaction temperature (400-600 °C) and steam to carbon ratio (S/C, 1, 3, 6, 9, and 12) on gas production and carbon nanotubes deposits were investigated. Analysis of products was performed in a gas chromatography. A flame ionization detector (FID) was used to analyze the reaction organic products (methane, ethane, ethylene,

acetaldehyde, ethanol, and acetone). A thermal conductivity detector (TCD) was used to analyze the gaseous products: H_2, CH_4, CO, and CO_2.

Ethanol conversion (X_{EtOH}), hydrogen yield (Y_{H_2}) and selectivity were calculated as follows [20]:

$$X_{EtOH} \ (\%) = (F_{EtOH, \ in} - F_{EtOH, \ out})/ \ (F_{EtOH, \ out}) \times 100 \qquad (3.1)$$

$$Y_{H_2} \ (\%) = (moles \ H_2 \ produced \ / \ (6 \times moles \ EtOH \ converted)) \times 100 \qquad (3.2)$$

$$S_i \ (\%) = (mole \ of \ gaseous \ product \ i) \ / \ (mole \ all \ gaseous \ products) \qquad (3.3)$$
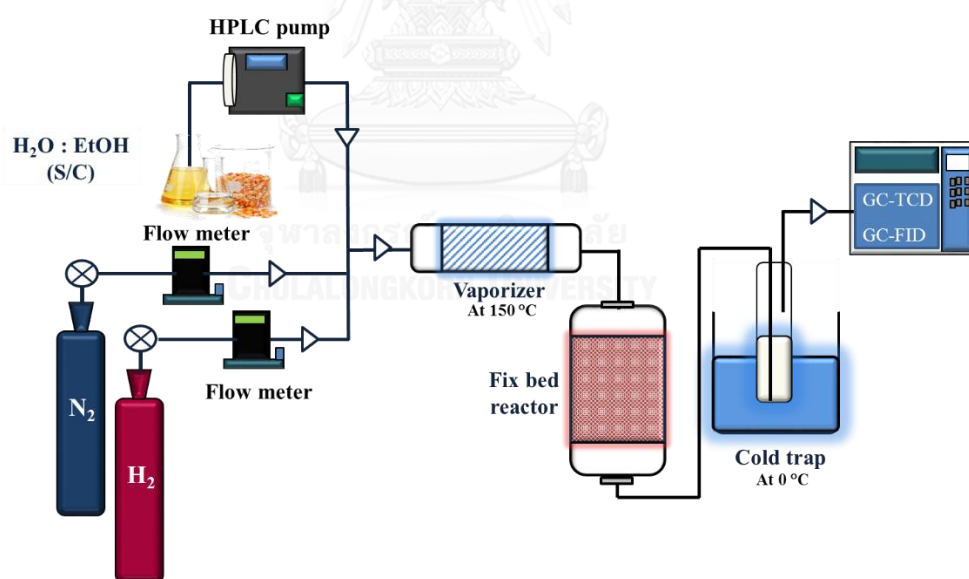
Figure 3.2 Reactor system for ethanol steam reforming

3.4   Purification of carbon nanotubes-silica fiber (CNTs-SF-E) composite

After reaction, the 30NiSF covered by CNTs was removed from the reactor. In order to eliminate Ni catalyst, it was washed with a mixture of 3 M HCl and 1 M HNO_3 solution with sonication at 40-50 °C for 4 h. Then it was rinsed with DI water until the final pH of final washing solution reached 7 and dried overnight at 110 °C to obtain CNTs-SF-E fibers as shown in **Figure 3.3**. The morphology and physical properties of CNTs-SF-E fibers were investigated by Transmission electron microscopy and N_2 physisorption.
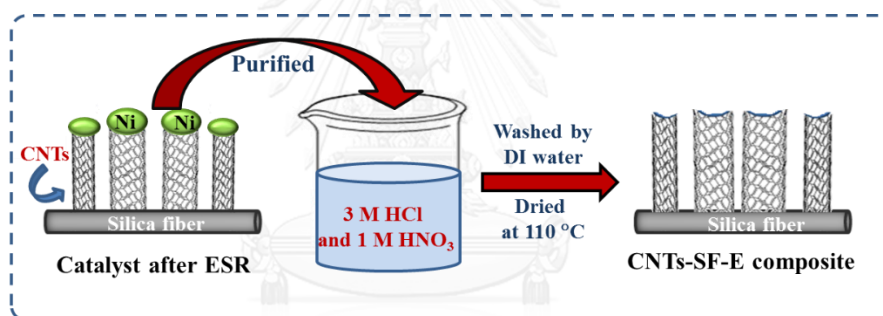
Figure 3.3 Purification scheme for CNTs-SF-E

3.5   Synthesis of NiCNTs-SF-E

NiCNTs-SF-E catalyst was prepared by impregnation of $Ni(NO_3)_2.6H_2O$ solution (Ni loading of 5 and 10 wt%) on CNTs-SF composite under sonication at 40-50 °C for 2 h. Then, the prepared catalysts were dried at 110 °C overnight and calcined at 350 °C for 4 h. The NiCNTs-SF-E catalysts with 5 and 10 wt% were denoted as 5NiCNTs-SF-E and 10NiCNTs-SF-E.

Besides, Ni/silica fiber (NiSF) and Ni/conventional porous silica (NiSP) catalysts were used as a comparison. Both catalysts were also prepared by impregnation method. A solution containing $Ni(NO_3)_2.6H_2O$ was dissolved in DI water. The $Ni(NO_3)_2.6H_2O$ solution was impregnated onto the support. Afterwards, the obtained catalyst was dried at 110 °C overnight and calcined at 500 °C for 2 h. The NiSF and NiSP catalysts with 10 wt% were denoted as 10NiSF and 10NiSP, respectively.

3.6   Catalytic performance of NiCNTs-SF-E in ethanol steam reforming

The performance of 5NiCNTs-SF-E, 10NiCNTs-SF-E, 10NiSF and 10NiSP was evaluated in ethanol steam reforming. The catalytic performance was carried out in a fixed-bed reactor with 0.2 g of the catalysts at atmospheric pressure. First, the catalysts were reduced under flowing 10 vol% H_2/N_2 at 400 °C for 1 h. Water to ethanol molar ratio of 9 was fed into the reactor through an HPLC pump under the N_2 flow. The organic products (methane, ethylene, acetaldehyde, ethanol, and acetone) were analyzed with a flame ionization detector (FID) with a Porapak-Q column. The gaseous products: H_2, CH_4, CO, and CO_2 were analyzed by a thermal conductivity detector (TCD) with a TDX-01 column.

Ethanol conversion (X_{EtOH}), hydrogen yield (Y_{H_2}) and selectivity were calculated as follows [20]:

$$X_{EtOH} \ (\%) = (F_{EtOH, \ in} - F_{EtOH, \ out})/ \ (F_{EtOH, \ out}) \times 100 \qquad\qquad (3.4)$$

$$Y_{H_2} \text{ (\%) = (moles } H_2 \text{ produced / (6 } \times \text{ moles EtOH converted)) } \times 100 \qquad (3.5)$$

$$S_i \text{ (\%) = (mole of gaseous product } i) \text{ / (mole all gaseous products)} \qquad (3.6)$$

3.7   Synthesis of carbon nanotubes-silica fiber composite from acetic acid steam reforming (CNTs-SF-A)

Carbon nanotubes-silica fibers composite (CNTs-SF-A) was prepared by using acetic acid steam reforming over NiSF as presented in **Figure 3.4**. The CNTs-SF-A composite was prepared by acetic acid steam reforming over NiSF at Ni loading of 30 wt% (30NiSF) at 600 °C and water to acetic acid molar ratio of 1, in a tubular reactor for 4 h, under N_2 flowing at 20 mL/min. During reaction, ethanol was converted to CNTs deposited on the surface of SF. After 4 h, the reaction was stopped and the 30NiSF covered by CNTs was removed from the reactor. Then it was washed by a mixture of 3 M HCl and 1 M HNO_3 solution with sonication at 40-50 °C for 4 h to eliminate Ni metal and other impurity. Finally, it was filtrated and washed with DI water and dried overnight at 120 °C to obtain CNTs-A-SF composite.
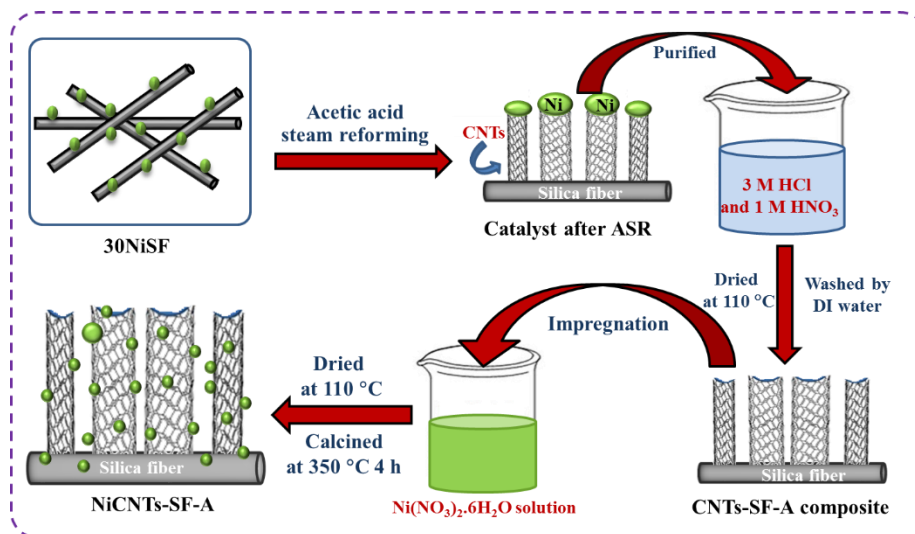
Figure 3.4 Synthesis scheme for CNTs-SF-A

3.8   Synthesis of NiCNTs-SF-A

Ni supported on CNTs-SF-A catalyst was prepared by impregnation method of Ni(NO$_3$)$_2$.6H$_2$O solution on CNTs-SF composite under sonication at 40-50 °C for 2 h with metal loading of 10 wt% **(Figure 3.4)**. Then, the catalysts were dried at 110 °C for 12 h and calcined at 350 °C for 4 h. The CNTs-SF-A catalysts with 10 wt% were denoted as 10NiCNTs-SF-A.

3.9   Catalytic performance of NiCNTs-SF-A in acetic acid steam reforming

The performance of 10NiCNTs-SF-A was evaluated in acetic acid steam reforming. The catalytic performance was carried out in a fixed-bed reactor with 0.2 g of the catalysts at atmospheric pressure. First, the catalysts were reduced under flowing 10 vol% H$_2$/N$_2$ at 400 °C for 1 h. Water/acetic acid molar ratio of 9 was fed into

the reactor through an HPLC pump under the N_2 flow. The organic products (methane, ethylene, acetaldehyde, ethanol, and acetone) were analyzed with a flame ionization detector (FID) with a Porapak-Q column. The gaseous products: H_2, CH_4, CO, and CO_2 were analyzed by a thermal conductivity detector (TCD) with a TDX-01column.

Acetic acid conversion (X_{AAc}), hydrogen yield (Y_{H_2}) and selectivity were calculated as follows [Ni-CoASR]:

$$X_{AAc} \text{ (%)} = (F_{AAc, \text{ in}} - F_{AAc, \text{ out}})/(F_{AAc, \text{ out}}) \times 100 \tag{3.7}$$

$$Y_{H_2} \text{ (%)} = (\text{moles } H_2 \text{ produced} / (4 \times \text{moles Acetic acid converted})) \times 100 \tag{3.8}$$

$$S_i \text{ (%)} = (\text{mole of gaseous product } i) / (\text{mole all gaseous products}) \tag{3.9}$$

3.10   Catalyst characterization

3.10.1 N_2 physisorption

N_2 adsorption and desorption isotherms were determined using a Micromeritics ASAP 2020. The specific surface area was determined using Brunauer–Emmett–Teller (BET) equation, and the pore volume and pore diameter of the catalysts were obtained from desorption branch of isotherms using the Barrett-Joyner-Halenda (BJH) method.

3.10.2 X-ray diffraction (XRD)

The X-ray diffraction (XRD) patterns of the catalysts were recorded on a Philips model X'Pert diffractometer with nickel filtered and CuK_α as the radiation source

$(\lambda = 1.54 \text{ Å})$ operated at 40 kV and 40 mA at room temperature. Scherrer equation was utilized to calculate the crystallite sizes of nickel metal.

3.10.3 Scanning electron microscopy (SEM)

Morphologies of the supports and the fresh and spent catalysts from ethanol/acetic acid steam reforming were analyzed by using a field emission scanning electron microscope (FE-SEM, JEOL JSM-7610F) equipped with energy dispersive X-ray spectrometer (EDX) at 20.0 kV. The average diameter of the fiber and the particle size of nickel metal of fiber catalyst were obtained from a SemAfore program. The actual metal content in the catalysts was determined by Energy dispersive X-ray spectrometer (EDX).

3.10.4 Transmission electron microscopy (TEM)

Transmission electron microscopy (TEM, JEOL 2100F) was used to observe the surface morphology appearance of carbon deposited on the catalyst from ethanol/acetic acid steam reforming.

3.10.5 Temperature programmed reduction of hydrogen (H$_2$-TPR)

Temperature programmed reduction of hydrogen (H$_2$-TPR) analysis was performed in a quartz reactor under a mixture flow of 5 vol% H$_2$ in N$_2$. The temperature of the reactor was increased linearly from 100 °C to 900 °C at a heating rate of 10.0

°C/min. Determination of percentage of nickel reduction of catalyst was calculated as follows:

$$Reduction\ degree\ (\%) = 100 \quad x \quad \frac{mol\ of\ H_2\ consumption_{\ measured}}{mol\ of\ H_2\ consumption_{\ calculated}}$$

3.10.6 Thermal analysis (TG/DTA)

Thermal analysis (TG/DTA) was conducted on METTLER TOLEDO STARe system, TGA/DSC1 Module in order to study the weight changes and to evaluate the yield of CNTs deposition on the SF support and the spent catalysts.

3.10.7 Raman spectroscopy

The Raman spectra of carbon deposited on the catalyst from ethanol steam reforming was obtained using a Fourier Transform Raman spectrometer (PerkinElmer).

CHAPTER IV
RESULTS AND DISCUSSION

The study in this chapter is divided into three parts. The first part is the investigation of co-production of hydrogen and carbon nanotubes-silica fiber (CNTs-SF-E) composite from ethanol steam reforming. NiSF was as a catalyst in this study. The effects of Ni loading, W/F, reaction temperature and S/C on the reaction activity as well as H_2 production and CNTs-SF characteristics of the NiSF catalyst were investigated. The second part describes the use of composite CNTs-SF as a support for the Ni-based catalyst to produce hydrogen gas production from ethanol steam reforming. The catalytic performance of NiCNTs-SF-E catalyst was investigated and compared with that of Ni/silica fiber catalyst (NiSF), and Ni/silica porous catalyst (NiSP). The third of the study focuses on acetic acid steam forming. A carbon nanotubes-silica fibrous composite (CNTs-SF-A) was synthesized by acetic steam reforming and it was used as a support for acetic acid steam reforming. The synthesized catalyst was compared with   NiCNTs-SF-E, NiSP and NiSF.

4.1   Co-production of hydrogen and carbon nanotubes-silica fiber (CNTs-SF) composite from ethanol steam reforming.

In this part, Ni/silica fiber catalyst (NiSF) prepared by sol–gel method assisted electrospinning technique following by conventional impregnation method was used as a catalyst for the simultaneous production of H_2 and CNTs from ethanol steam

reforming. Results of the catalyst characterization and catalytic performance were discussed. The catalytic performance with different effects such as Ni loading, W/F, temperature and S/C was also discussed.

4.1.1 Catalyst Characterization

The surface morphologies of SF, 10NiSF, 20NiSF, and 30NiSF are shown in **Figure 4.1**. The fiber surface was smooth with average diameter of 171.5 nm (**Figure 4.1 (a)**) as estimated by SemAfore program. The SEM images in **Figure 4.1(b-d)** reveal Ni metal particles decorated on the silica fiber. The size of NiO particles tended to increase and became more aggregative with the increase of Ni loading. The average particles size of the catalysts measured by SemAfore was presented in **Table 4.1**. The size of NiO particles increased significantly with the increase of NiO loading, reaching 27 nm at Ni loading of 30 wt%.
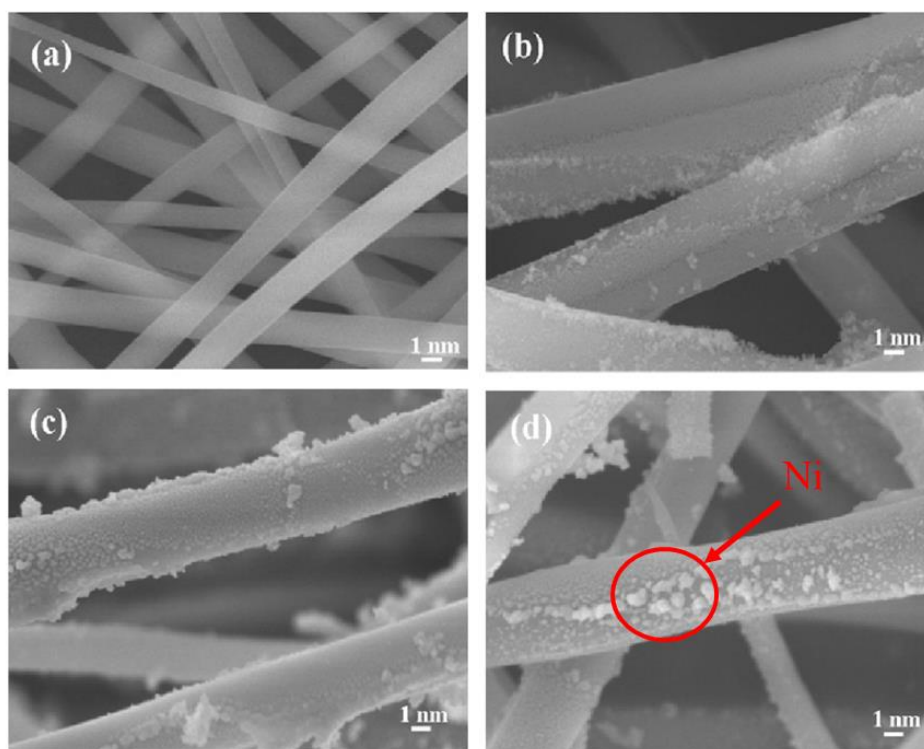
Figure 4.1 SEM images of the fresh catalysts, (a) SF, (b) 10NiSF, (c) 20NiSF, and (d) 30NiSF

The specific surface area and pore volume of the supports and the fresh catalysts are also presented in **Table 4.1**. The actual contents of Ni as determined by EDX were fairly similar and close to the theoretical Ni loading. The surface area of SF was quite low (3 m^2/g) and pore volume was 0.0003 cm^3/g, suggesting that the obtained SF was a non-porous structure. After adding Ni to the support, an evidence of increase in the surface area and pore volume as Ni content rising was observed. The highest surface area of 19 m^2/g was obtained at Ni loading of 30 wt%. This might be

due to that the presence of Ni with loadings up to 30 wt% was covered all of SF

surfaces, which was useful in improving the surface area [17].

Table 4.1 Textural properties of the supports and the fresh catalysts

Samples	Surface area (m^2/g)	Pore volume (cm^3/g)	Pore diameter (nm)	Ni $(wt\%)^a$	d_{XRD} $(nm)^b$	d_{SEM} $(nm)^c$
SF	3	0.0003	2.2	-	-	171.5
10NiSF	5	0.0108	49.0	11	20.2	14.7
20NiSF	8	0.0196	30.4	18	24.5	24.6
30NiSF	19	0.0754	18.6	32	26.6	27.0

[a] Determined by EDS

[b] Average Ni particles sizes determined XRD using Debye–Scherrer equation.

[c] Average Ni particles sizes determined by using SemAfore program.

The XRD patterns of SF and the catalysts with different Ni loading are displayed

in **Figure 4.2**. The broad diffraction peaks located at 2θ value of 21.3° were assigned

to amorphous SiO_2 support. The diffraction peaks at 2θ value of 36.8, 42.8, 62.4, 75.4

and 79° indicated the characteristic peak of NiO [79]. The peak intensity of NiSF

catalysts tended to increase with increasing amount of metal employed. The NiO

crystal size estimated by Scherrer formula using the NiO (2 0 0) peak is presented in

Table 4.1. The crystal sizes of all samples were in the range of 20.2 - 26.6 nm. The

crystal size of NiO became bigger as the content of Ni increased. The aggregation of NiO was the main responsible for the increase of NiO crystal sizes at higher Ni loadings [80]. This result was in agreement with the results of SEM.
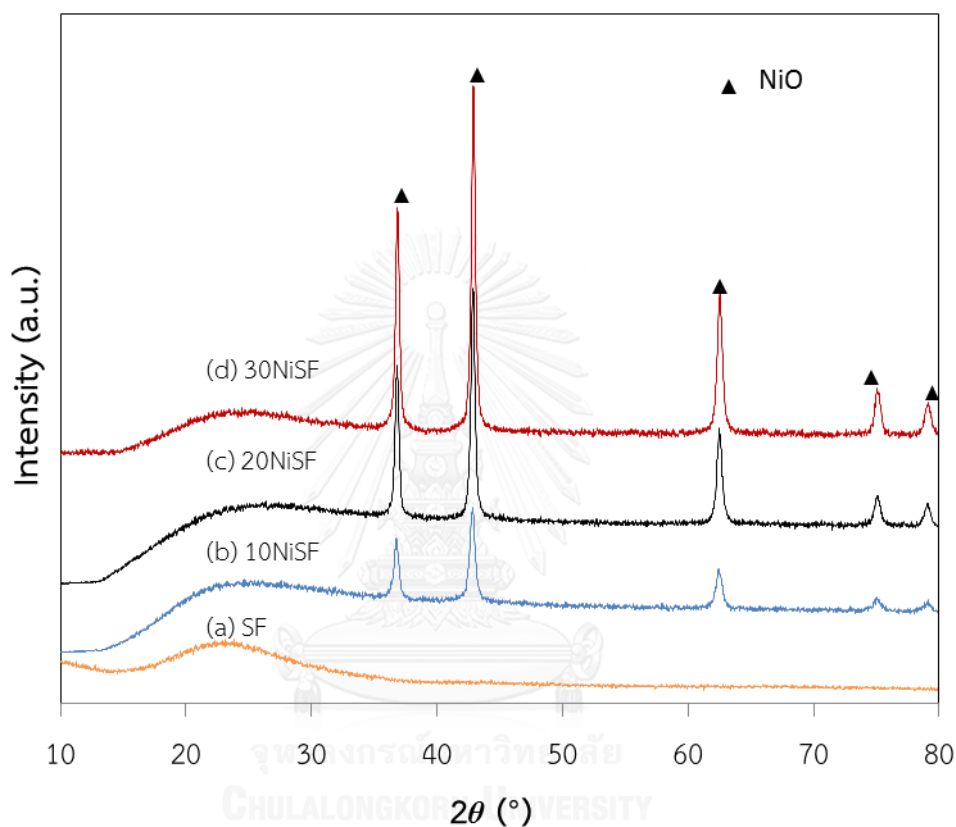
Figure 4.2 XRD patterns of the fresh catalysts, (a) SF, (b) 10NiSF, (c) 20NiSF, and (d) 30NiSF

Figure 4.3 displayed the H_2-TPR profiles of the fresh catalysts. All of catalysts consisted of two major reduction peaks. The first peak at low temperature in the range of 310-440 °C was assigned to the reduction of NiO with large particles which had no or weak interaction with the SiO_2 support. The second peak at high temperature in the

range of 450-530 °C corresponded to the reduction of NiO with small particles or well distributed which strongly interacted with the SiO_2 support [81]. The intensity of reduction peaks became stronger when Ni loading increased from 10 to 30 wt%. This could be assigned to extent a percentage of Ni concentration in the catalyst. In addition, the main reduction peaks shifted toward higher temperature regions with increasing Ni loading. This was probably due to that at lower Ni loading, Ni species may highly disperse. On the other hand, Ni tended to aggregate when the metal loading increased. This introduced to limit diffusion of hydrogen in nickel oxides phase, resulting in a high reduction temperature [82].
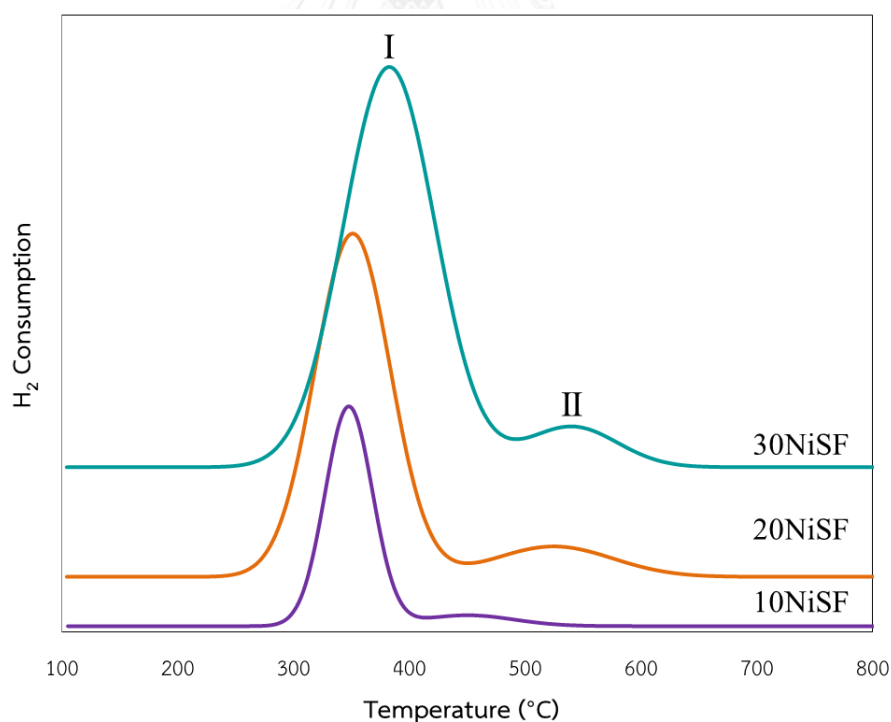
Figure 4.3 H_2-TPR profiles of the fresh catalysts, 10NiSF, 20NiSF, and 30NiSF

4.1.2 Catalytic performance

The catalytic performance of the prepared catalysts was investigated with different effects on the production of H_2 and CNTs such as Ni loading, W/F, temperature and S/C.

4.1.2.1 Hydrogen obtained from ethanol steam reforming

4.1.2.1.1 Effect of Ni loading

Figure 4.4 illustrates ethanol conversion and product distribution over NiSF with different Ni loading (10, 20 and 30 wt%) at 600 °C, W/F of 9 g_{cat}h/mol and S/C of 1. It was observed that conversion increased gradually with increasing Ni loading and reached complete at Ni loading of 20 wt%. The dominant products measured in the outlet gas from ethanol steam reforming were H_2, CH_4, CO and CO_2. H_2 yield seemed to decrease slightly as Ni loadings increased from 10 to 20 wt%, while CO selectivity decreased gradually. In addition, methane concentration increased gradually with increasing Ni loading, reaching 36% at Ni loading of 30 wt%, suggesting the presence of methanation reaction. It was well-known that methanation reaction was favored with large nickel particle size [82]. Therefore, H_2 was consumed resulting in decrease in H_2 yield. The results implied that the increase of metal loading did not effectively improve H_2 yield but led to produce more undesirable by-product CH_4.
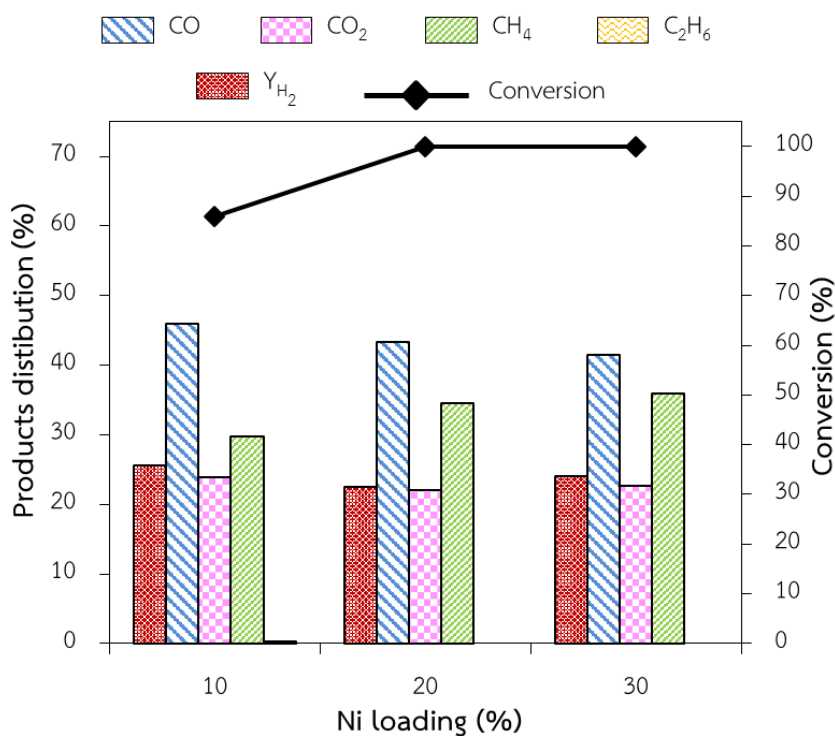
Figure 4.4 Ethanol conversion and hydrogen yield of NiSF with different Ni loading at 600 °C, W/F of 9 g_{cat}h/mol and S/C of 1

   4.1.2.1.2 Effect of W/F

   The effect of W/F on ethanol conversion and hydrogen yield in ethanol steam reforming over NiSF catalyst is displayed in **Figure 4.5**. The W/F was varied from 9 to 36 g_{cat}h/mol by changing feed flow rate of ethanol. It can be seen that ethanol conversion reached almost 85% at W/F of 9 g_{cat}h/mol. As W/F increased, ethanol conversion increased as expected and was fully complete at W/F of 18 g_{cat}h/mol. Hydrogen yield and CO selectivity also increased slightly with increasing W/F from 9 to 18 g_{cat}h/mol. The selectivity of CH_4 showed opposite tendency, decreasing its product as W/F increased. The fact was that a large W/F meant high contact time which

promoted C-C bond cleavage. Therefore, decomposition of ethanol (reaction 4.1) was favored, resulting in high H_2 yield and CO selectivity [83]. The high contact could also lead to occur methane reforming (reaction 4.2) as a result low methane selectivity was obtained.

$$C_2H_5OH \longrightarrow H_2 + CO + CH_4 \qquad\qquad (4.1)$$

$$CH_4 + H_2O \longrightarrow CO + 3H_2 \qquad\qquad (4.2)$$

$$C_2H_5OH \longrightarrow C_2H_4 + H_2O \qquad\qquad (4.3)$$

$$CO + H_2O \longrightarrow H_2 + CO_2 \qquad\qquad (4.4)$$

However, H_2 yield and CO selectivity had almost no changed when W/F increased from 18 to 36 $g_{cat}h/mol$, implying that decomposition of ethanol and methane reforming reached equilibrium.
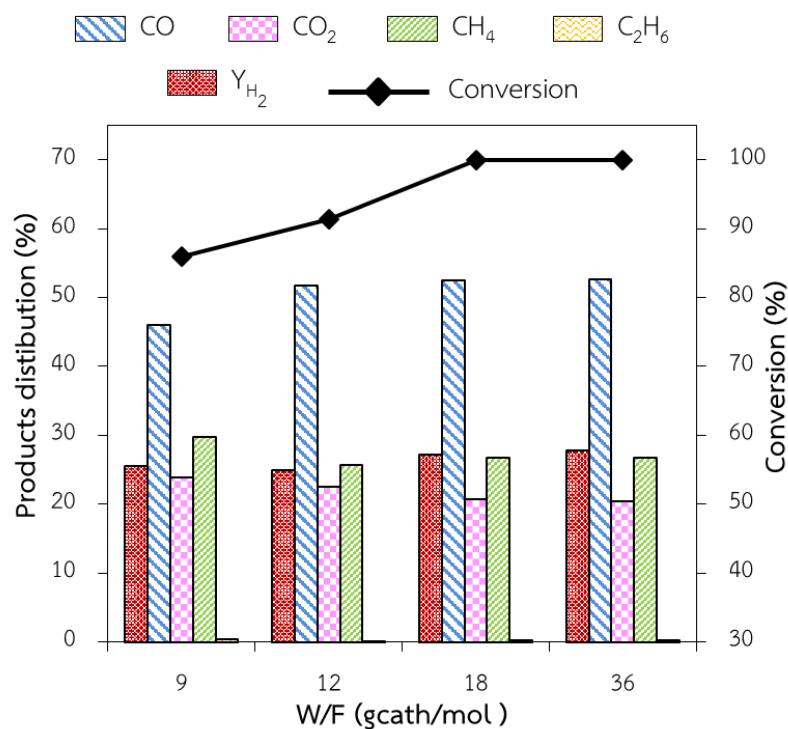
Figure 4.5 Ethanol conversion and hydrogen yield of 10NiSF with different W/F at 600 °C and S/C of 1

4.1.2.1.3 Effect of temperature

The effect of reaction temperature on ethanol conversion and product distribution over NiSF catalyst was studied in the range between 400 and 600 °C as shown in **Figure 4.6**. At 400 °C, ethanol conversion was about 52% and the negligible amount of C_2 product like ethane was detected at 400 °C. On further increasing reaction temperature, ethanol conversion increased gradually and reached full conversion at 600 °C. In product distribution, hydrogen yield and CO_2 selectivity also increased obviously when reaction temperature increased from 400 to 600 °C. A

maximum of H_2 yield of 28% was obtained at temperature of 600 °C. In contrast, ethane and CH_4 selectivity tended to decrease gradually. It has been reported that capability in cleaving of C-C bond of Ni was weaken at low temperatures and dehydration of ethanol to ethylene (reaction 4.3) and decomposition (reaction 4.1) were favored, so low conversion of ethanol and high ethane selectivity were obtained. With increasing temperature, the WGS (reaction 4.3) and methane steam reforming reactions (reaction 4.2) proceeded, resulting in the increase of H_2 yield and CO_2 selectivity [84].
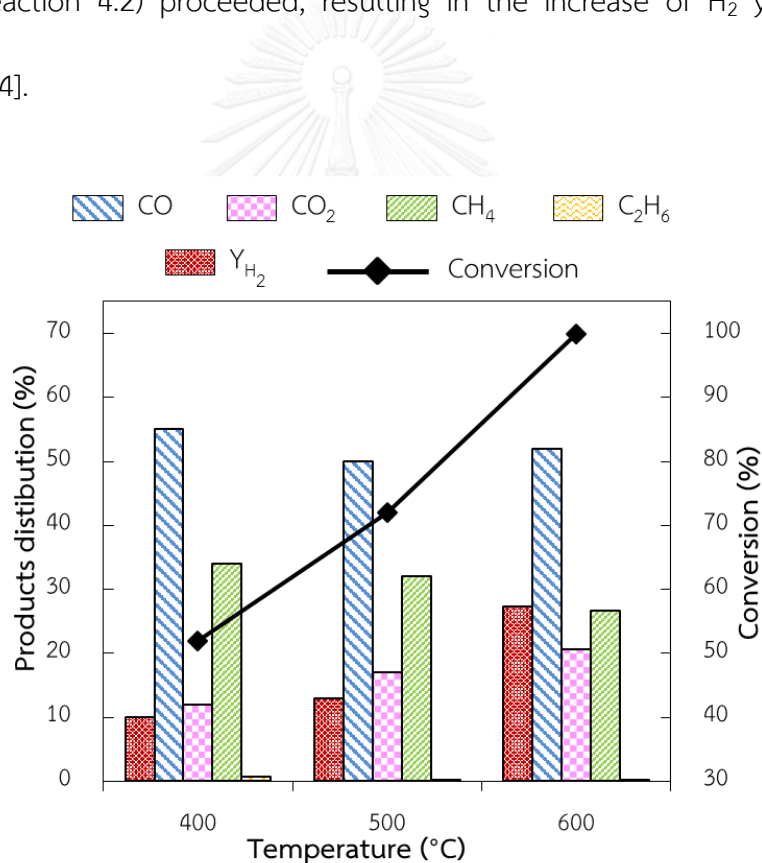
Figure 4.6 Ethanol conversion and hydrogen yield of 10NiSF at different temperature at W/F of 18 g_{cat}h/mol and S/C of 1

4.1.2.1.4 Effect of S/C molar ratio

The influence of S/C molar ratio on catalytic performance of steam reforming reaction over NiSF catalyst was studied at 600 °C with different S/C ratios of 1, 3, 6, 9 and 12, respectively as shown in **Figure 4.7**. Ethanol conversion was complete in the whole range of S/C studied. However, H_2 yield and CO_2 increased progressively as S/C ratio increased. The highest H_2 yield of 55% was achieved at 9:1. In contrast, the selectivity to CO and CH_4 decreased gradually when S/C ratio increased. The results revealed that the addition more water in feed exhibited positive effect on H_2 yield. It has been reported that WGS reaction was unflavored at low S/C ratio, as a results the high selectivity to CO and CH_4 were obtained. By increasing S/C ratio, WGS and methane steam reforming reactions were promoted, which resulted in an increase of H_2 and CO_2 concentration, associated with the gradual decrease of CH_4 and CO concentration [4]. However, further increase the ratio to 12 did not obviously improve H_2 yield as well as change the concentration of CO and CO_2, implying ethanol steam reforming and WGS reached to equilibrium [8].

Base on the results above, it can be concluded that the optimum conditions in term of considering hydrogen production were Ni loading of 10 wt%, W/F of 18, reaction temperature of 600 °C, and S/C of 9.
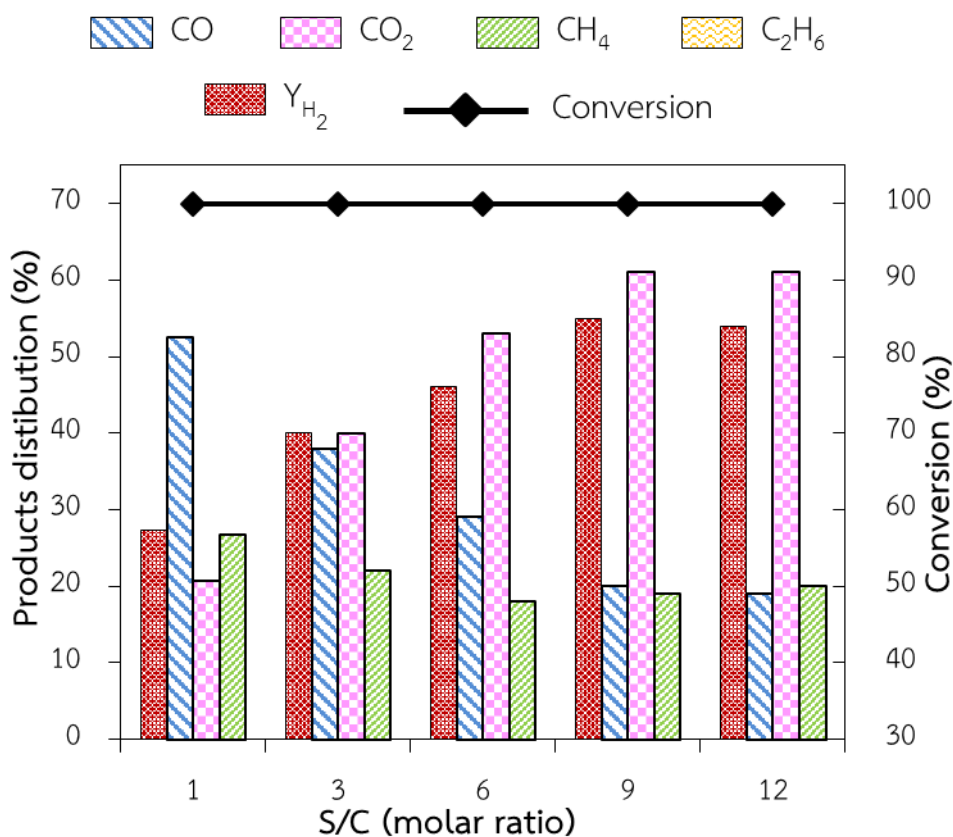
Figure 4.7 Ethanol conversion and hydrogen yield of 10NiSF with different S/C at 600 °C and W/F of 18 g_{cat}h/mol

4.1.2.2 Carbon nanotube synthesized from steam reforming of ethanol

4.1.2.2.1 Effect of Ni loadings

Figure 4.8 shows SEM images of filament carbons deposited over NiSF catalysts produced from steam reforming of ethanol with different Ni loadings of 10, 20 and 30 wt% at reaction temperature of 600 °C, W/F of 9 g_{cat}h/mol and S/C of 1. It can be seen that all SEM images revealed that filament carbons with highly entangled and wed-like formed on NiSF catalysts. Filament carbons seemed to cover on all of surface SF when

Ni loading was 30 wt%. As seen in **Figure 4.8(a) – (c),** the diameter and size of the

filament carbons became large when Ni loading increased. This result indicated that

the morphology of carbon products was affected apparently by the loading amounts

of Ni. It has been reported that the diameter of filament carbons formation strongly

depends on the size of active metal particles. The larger size of metal particles is likely

to form the larger size of filament carbons, whereas the smaller size of metal particles

is likely to form the smaller size of filament carbons [85]. TEM image of the used 30NiSF

catalyst is also shown in **Figure 4.8 (d).** It can be clearly seen that the filament carbons

was multi-walled carbon nanotubes. The average outer diameter of CNTs was in range

of 22-30 nm which was closer to the average NiO particle sizes obtained by XRD. The

yield of CNTs deposited on the catalysts was calculated from the weight loss of carbon

deposition by TG/DTA analysis and the results are presented in **Figure 4.9**. Total yield

of carbon produced from ethanol steam reforming on the catalysts was in range of 26-

36%. The yield of carbon increased slightly as Ni loading increased. This result was

supposed by the specific surface area and pore volume of the spent catalyst as

presented in **Table 4.2**. Both surface area and pore volume showed an increasing

trend with increase in Ni loading. This suggested that the amount of carbon could play

an important role in increase of specific surface area of the spent catalysts since carbon

is well-known for its high surface, which was beneficial for further enhancement of the

catalytic activities of the catalyst.
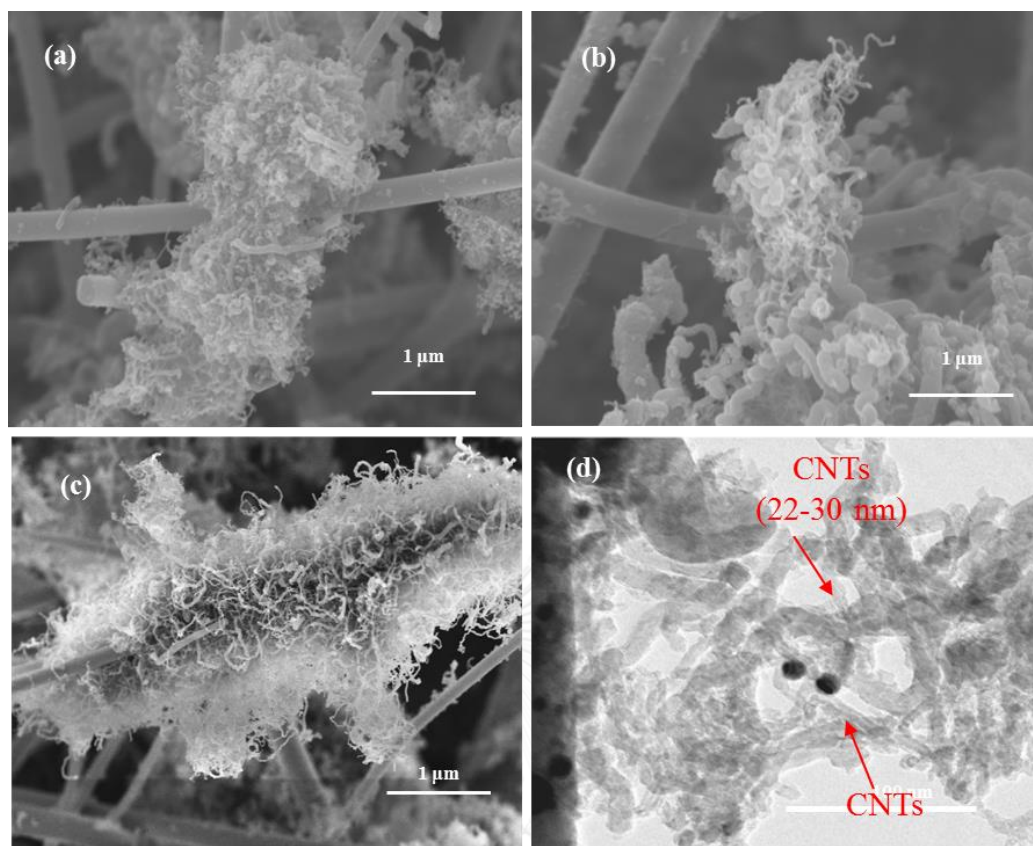
Figure 4.8 SEM images of carbon deposited over NiSF catalysts produced from steam reforming of ethanol with different Ni loading: (a) 10NiSF, (b) 20NiSF, and (c) 30NiSF at 600 °C, W/F 9 and S/C 1
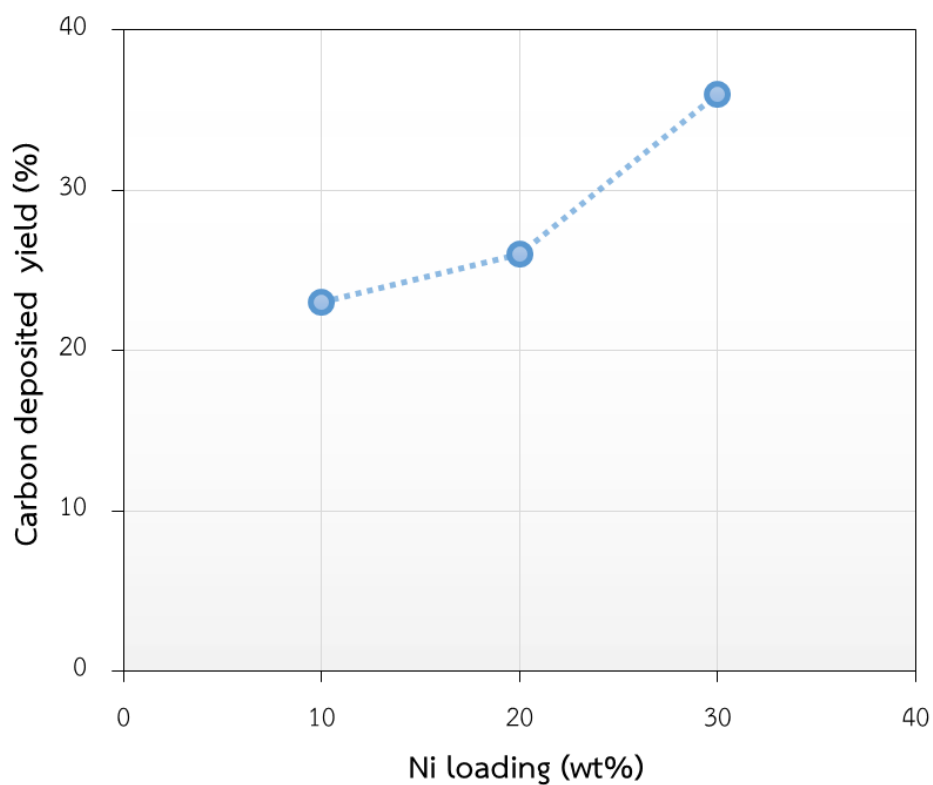
Figure 4.9 Carbon yield on NiSF catalyst produced from ethanol steam reforming with different Ni loading at 600 °C, W/F of 9 g_{cat}h/mol and S/C of 1

Table 4.2 The specific surface area of the spent catalysts

Samples	Surface area (m^2/g)	Pore volume (cm^3/g)	Pore diameter (nm)
10NiSF	33.6	0.077	9
20NiSF	46.7	0.104	26
30NiSF	116.7	0.287	12

4.1.2.2.2 Effect of W/F

The total amount of CNTs deposited on 10NiSF catalyst produced from steam reforming of ethanol at different W/F of 9, 12, 18 and 36 g_{cat}h/mol (S/C of 1 and temperature of 600 °C) are also shown in **Figure 4.10**. It was observed that total carbon deposited on the catalyst varied between 8 and 23%. When W/F increased from 9 to 36 g_{cat}h/mol, an evident decrease in carbon yield was observed and the lowest carbon yield of 8% was obtained at W/F of 36 g_{cat}h/mol due to the increase of contact time between reactants and metal catalyst surface. According to literature, it has been reported that the capability of breaking C-C bond was weakened at lower W/F due to lower contact time [86]. **Figure 4.11** shows the yield of gaseous carbon products and ethanol conversion and hydrogen yield produced from ethanol steam reforming at different W/F. It was observed that gaseous carbon products increased with the increase of W/F from 9 to 36 g_{cat}h/mol, while the amount of simultaneous carbon decreased significantly. This result implied that steam reforming of ethanol in the study occurred though carbon intermediates, which reacted with water to produce gas products when contact time increased. This was reasonable to suppose that high amount of carbon was favored at lower contact time.

Figure 4.10 Carbon yield on NiSF catalyst produced from ethanol steam reforming of 10NiSF with different W/F at 600 °C and S/C of 1
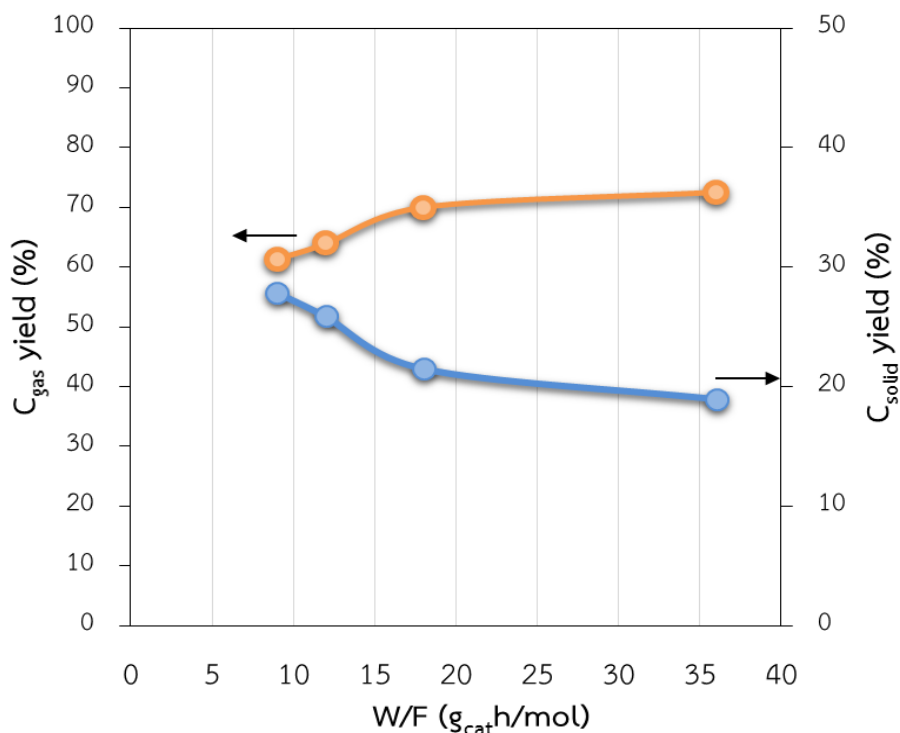
Figure 4.11 The yield of gaseous carbon products and CNTs produced from ethanol steam reforming at different W/F

4.1.2.2.3 Effect of temperatures

TG/DTA curves of carbon deposited over 10NiSF catalyst at different temperatures, 400, 500, and 600 °C (W/F of 18 g_{cat}h/mol and S/C of 1) are shown in **Figure 4.12.** The catalyst at reaction temperature of 400 °C, three weight loss stages were observed. The first stage at 460-530 °C can be associated with the oxidation of amorphous carbon. The second weight loss stage was obtained at temperature range of 530-577 °C, which was assigned to the decomposition of carbon with disordered structures. The third weight loss stage at temperature between 597 and 670 °C was the decomposition of stable multiwall of CNTs [87]. There were two weight loss stages

for the used catalyst at reaction temperature of 500 °C, which was assigned to the decomposition of less stable CNTs and stable CNTs. On the contrary, at the reaction temperature of 600 °C only CNTs were observed. In addition, the total carbon of 18% was found on 10NiSF catalyst when the reaction was conducted at 400 °C as shown in **Figure 4.13.** The total carbon content on the catalyst with reaction at 500 and 600 °C was about 15 and 13%, respectively. The results indicated that at lower temperature produced mixture of amorphous carbon, SMWTs and MWCNTs, while reaction performed at higher temperature formed mainly MWCNTs. According to the previous report, dehydration of ethanol to C_2H_4 was favored at low reaction temperature because the ability in cleaving of C-C of Ni was weakened. Therefore, the presence of amorphous carbon formation at low temperature could be attributed to polymerization of C_{2+} products. On the contrary, the main routes for formation of CNTs involved methane and/or the Boudouard reaction which were favored at high reaction temperature [50] as following:

$$C_2H_5OH \longrightarrow C_2H_4 \longrightarrow n(C_2H_4) \longrightarrow CNFs \text{ or } CNTs \tag{4.5}$$

$$CH_4 \longrightarrow C + 2H_2 \tag{4.6}$$

$$2CO \longrightarrow CO_2 + C \tag{4.7}$$
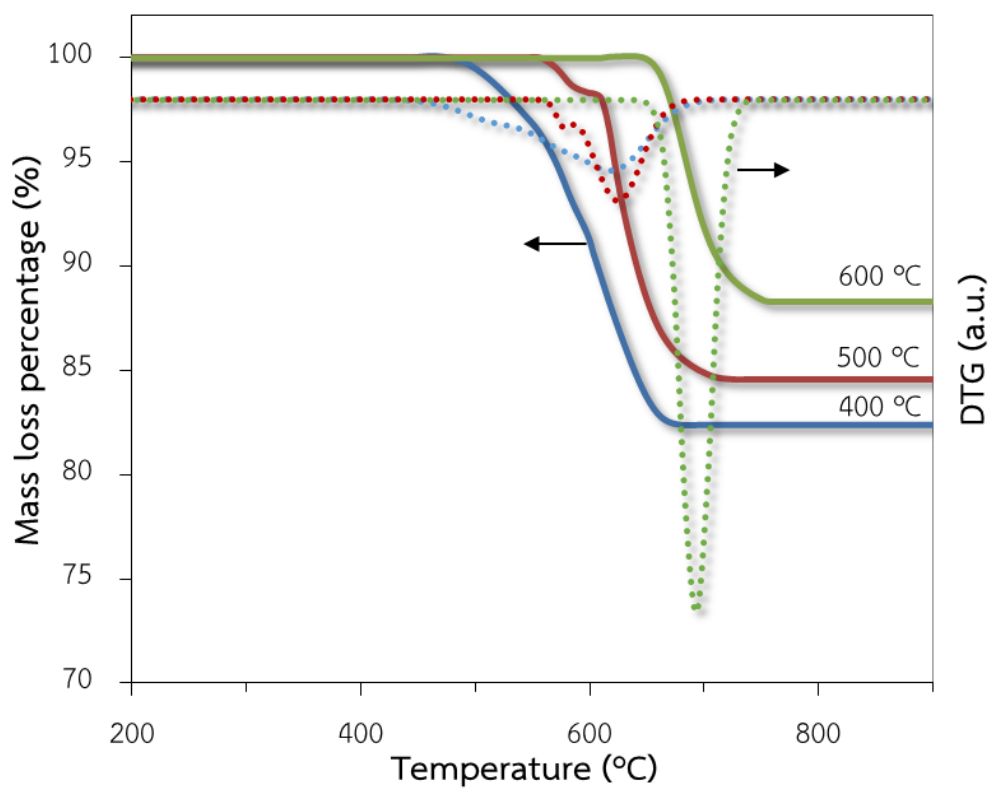
Figure 4.12 TG/DTA curves of carbon deposited over 10NiSF catalysts produced from steam reforming of ethanol at different temperatures: 400, 500, and 600 °C
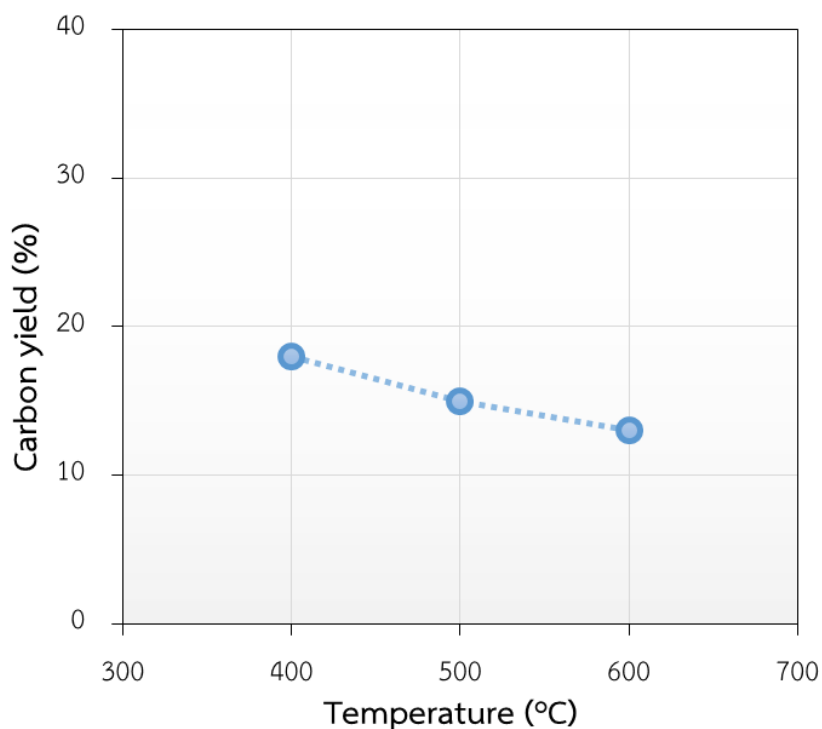
Figure 4.13 Carbon yield on NiSF catalyst produced from ethanol steam reforming of 10NiSF at different temperature at W/F of 18 g_{cat}h/mol and S/C of 1

Raman analysis was further used to characterize carbon formed by steam reforming of ethanol on the catalyst at different temperatures and results are shown in **Figure 4.14**. In the spectrum, two Raman peaks were observed at 1210-1360 cm^{-1} and 1550-1660 cm^{-1} which was attributed to D band and G band. The D band corresponded to disordered carbon structures in the CNTs. The G band was attributed to highly structural order in the CNTs. The intensity ratio (I_G/I_D) was also associated with the structure of CNTs. The high I_G/I_D ratio indicated highly organized structure of the produced nanotubes [58]. The order of the I_G/I_D ratio calculated from **Figure 4.14** was as follows: 400 °C (I_G/I_D = 0.79) < 500 °C (I_G/I_D = 0.90) < 600 °C (I_G/I_D = 0.92). The result

indicated that the I_G/I_D ratio increased with the increase of reaction temperature, implying that high-quality nanotubes were formed at reaction temperature of 600 ℃.
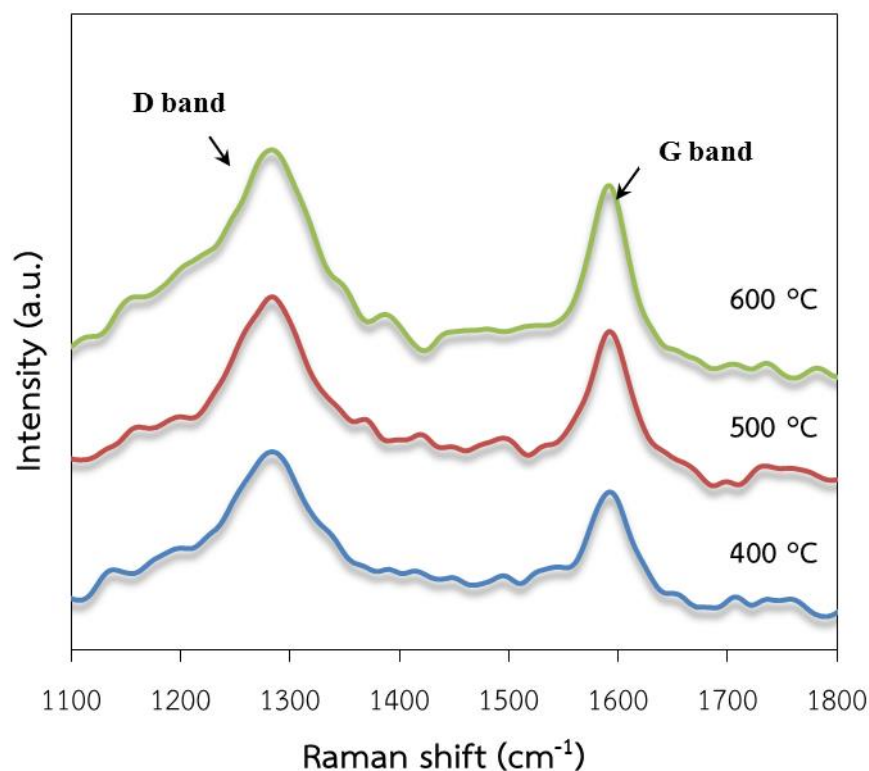
Figure 4.14 Raman spectra of carbon deposited over 10NiSF at different temperatures: 400, 500, and 600 ℃

4.1.2.2.4 Effect of S/C

The yield of CNTs deposited on 10NiSF catalyst with different S/C ratios ranged from 1 to 12 (W/F of 18 g_{cat}h/mol and reaction temperature of 600 ℃) is shown in **Figure 4.15**. The yield of carbon was about 13% at S/C of 1. On further increasing S/C, the yield of CNTs dropped a little to 8% at S/C of 12. These results suggested that high amount of carbon was obtained at lower S/C molar ratio. This result was probably

attributed to that at high water content could promote gasification of carbon as well as could facilitate steam reforming and WGS reaction resulting in high CO_2 concentration.
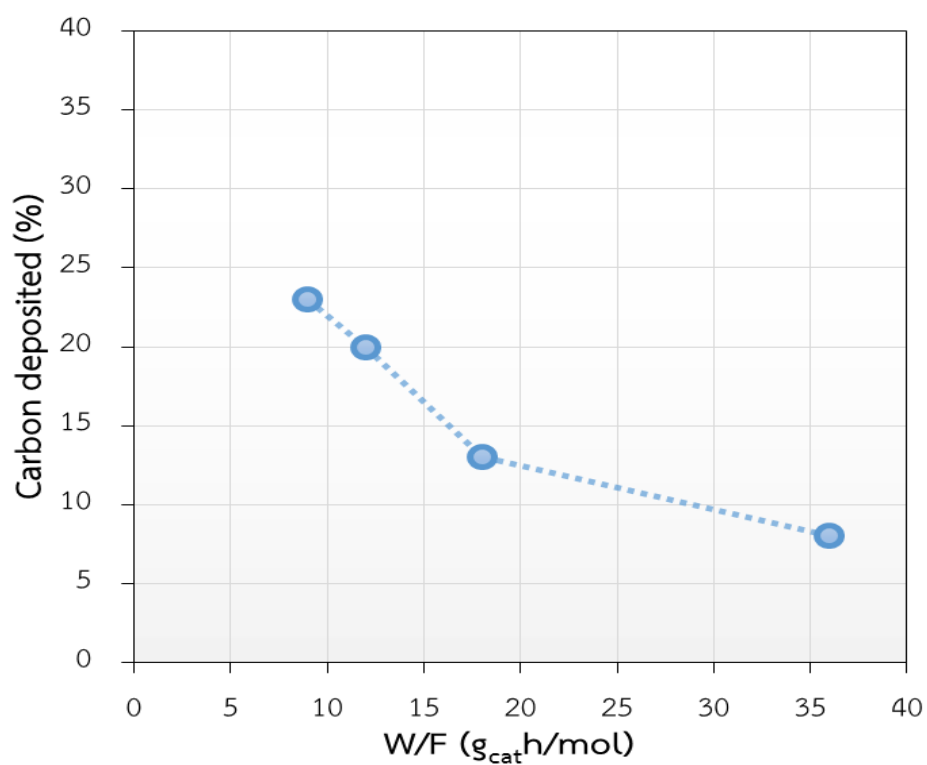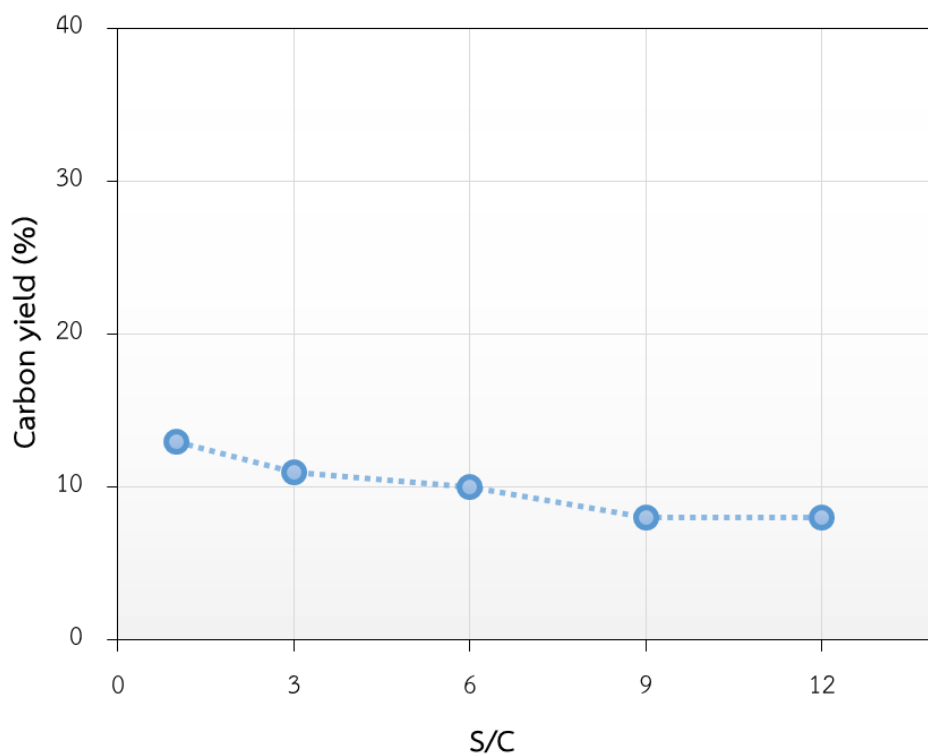

Figure 4.15 Carbon yield on NiSF catalyst produced from ethanol steam reforming of 10NiSF with different S/C at 600 °C and W/F of 18 $g_{cat}h/mol$
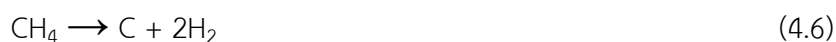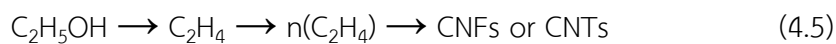
According to the results mentioned, it can be concluded that Ni loading of 30 wt%, W/F of 9, S/C of 1 and reaction temperature of 600 °C were found to be effective conditions for ethanol steam reforming to synthesize CNTs.

4.1.3 Purification of CNTs-SF-E

After reaction the CNTs-SF-E was purified by treatment with acids to remove the Ni catalysts. After purification scanning electron microscopy with Energy dispersive X-ray spectrometer was used to measure composition of CNTs-SF-E after acid treatment and the results are shown in **Figure 4.16**. The CNTs-SF-E composite after purification composed of carbon 64%, oxygen 23% and silicon 9.5%. Ni catalyst was not observed in by EDX analysis suggesting that metal removal was achieved.

Figure 4.17 shows TEM images of purified CNTs on SF produced from steam reforming of ethanol at Ni loading of 30 wt%, temperature of 600 °C, W/F of 9 g_{cat}h/mol and S/C of 1. It can be seen that the SF was fully covered by CNTs with large and small diameters. The average diameter of CNTs on SF was approximately 20-30 nm which was close to the average NiO particle sizes obtained by XRD. The inner diameters of carbon nanotubes were between 5-11 nm.
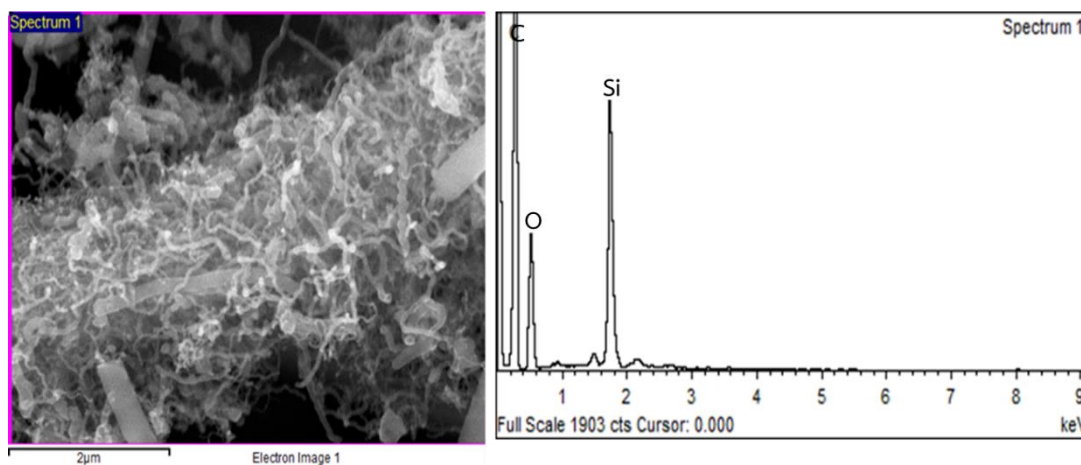
Figure 4.16 Elemental compositions of CNTs-SF-E after purification
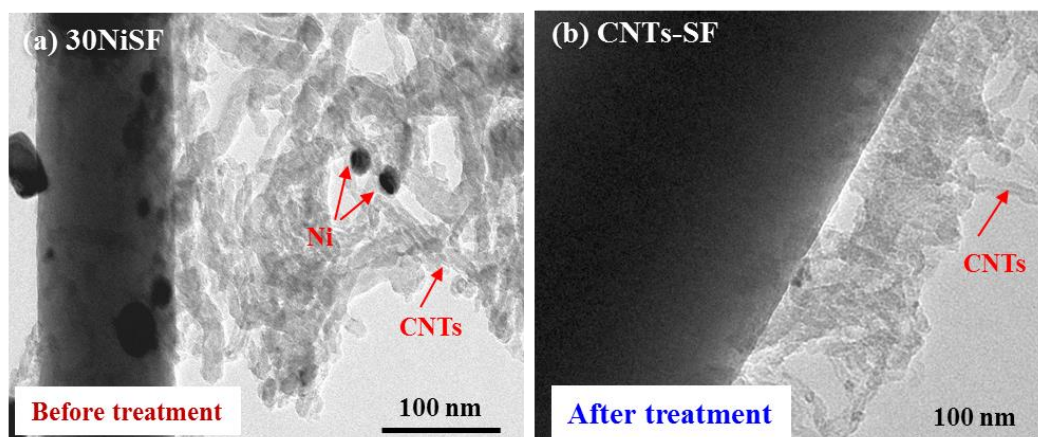
Figure 4.17 Transmission electron microscopy of the catalyst (a) before and (b) after treatment

TG/DTA was used to analyze the types and yield of carbon deposited on silica fiber as shown in **Figure 4.18**. The result showed that the CNTs-SF composite exhibited only one peak at temperature range of 600-700 °C, which attributed to oxidation temperature of CNTs [88]. Additionally, total weight loss of CNTs-SF composite was about 10 wt%, indicating that the amount of CNTs over silica fiber produced from ethanol steam reforming was 10 wt%.
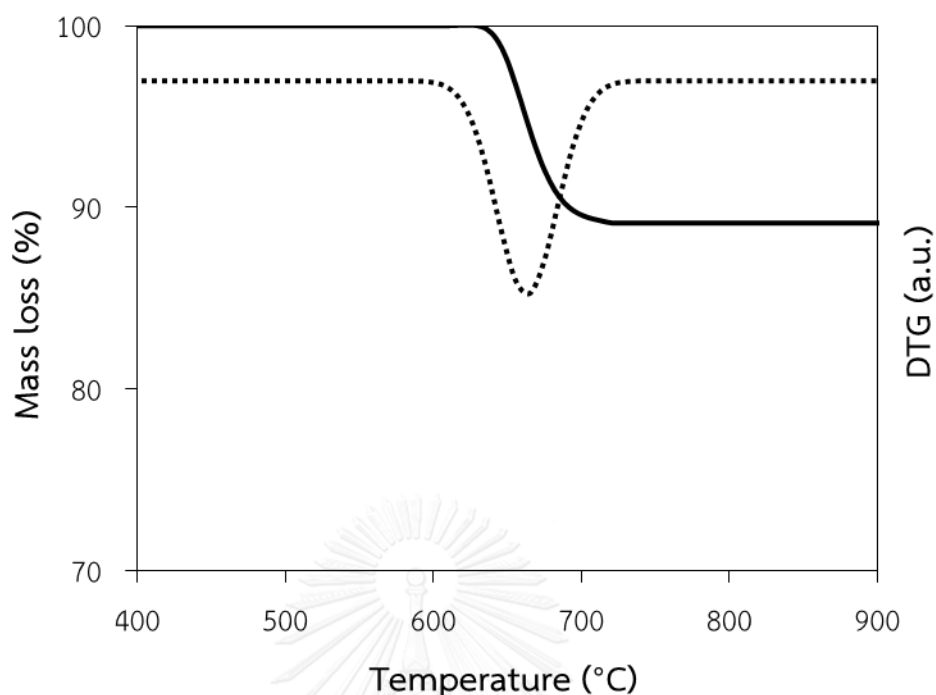
Figure 4.18 TG/DTA profile of the CNTs-SF-E

The specific surface area of the spent 30NiSF catalyst was 116 m^2/g **(Table 4.2)**, while specific surface area of CNTs-SF-E after treatment with acids was 157 m^2/g. This might be due to that the treatment led to open the tube tip, which allowed the nitrogen adsorption in the intertubular pores of CNTs resulting in increase in surface area [89].

4.2 Ni supported on CNTs-SF-E fiber catalysts for ethanol steam reforming

CNTs-SF-E produced by ethanol steam reforming from the first part was used as a support for Ni catalyst. Results of the catalyst characterization, catalyst performance and comparison of the ethanol steam reforming reaction with NiSF and

NiSP were discussed. Results of catalytic stability and characterization of spent catalysts were also discussed.

4.2.1 Characterization of NiCNTs-SF-E

The N_2 adsorption-desorption isotherms of the catalysts are depicted in **Figure 4.19**. The SP and 10NiSP revealed IV isotherms with H1-typed hysteresis loops appearing at large relative pressure in the *P/P$_0$* range from 0.70 to 1.00, which indicated a typical characteristic of mesoporous structure with cylinder pores [90]. As for the SF and 10NiSF, the shapes of N_2 adsorption and desorption were linear with relative pressure of *P/P$_0$* of 0, suggesting that the SF and 10NiSF were a nonporous material. CNTs revealed Type II adsorption isotherms, which was agreement with the work of Li et al [89]. **Table 4.3** summarizes the specific surface area, pore volume and average pore size of the all catalysts. The pure SP showed the highest specific surface area of 240 m^2/g and large pore volume (1.16 cm^3g^{-1}), while surface area of the SF was quite small (3 m^2/g) and pore volume was 0.001 cm^3g^{-1}.The small specific surface area of SF was attributed to the non-porous structure, which was confirmed by the N_2 adsorption-desorption isotherms. The specific surface area of CNTs-SF-E was 157 m^2/g, while the surface area decreased after adding Ni to the supports due to blockage of pore entrances by Ni [91]. In contrast, the surface area of Ni/SF increased slightly from 3 to 5 m^2/g after adding Ni to SF support. The increase of surface area after adding Ni to the supports could be attributed to the deposition of Ni on the supports, which was

in agreements with TEM results. Klaigaew et al. [80] also found that the increase of surface area after addition of catalyst was likely due to covering of the catalyst on support's surface.
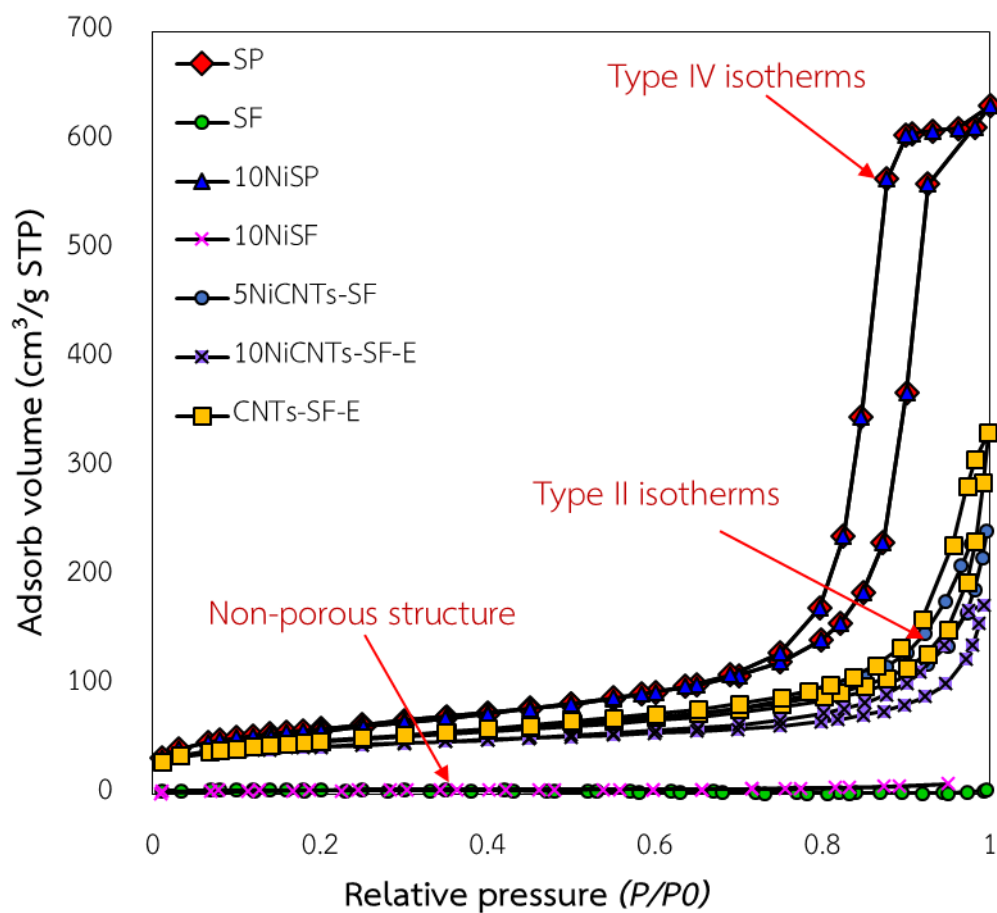
Figure 4.19 Nitrogen adsorption–desorption isotherm curves at 77 K for SP, SF, 10NiSP, 10NiSF, 5NiCNTs-SF-E, 10NiCNTs-SF-E and CNTs-SF-E

Table 4.3 The specific surface area of the supports and the fresh catalysts

Samples	Surface area (m^2/g)	Pore volume (cm^3/g)	Pore diameter (nm)	Ni (wt%)[a]
SP	236	1.160	11.8	-
SF	3	0.001	12.5	-
CNTs-SF-E	157	0.508	13.6	-
10NiSP	240	1.170	11.8	11.25
10NiSF	5	0.013	7.4	11.12
5NiCNTs-SF-E	152	0.362	10.9	3.90
10NiCNTs-SF-E	132	0.245	10.7	11.34

[a] Determined by EDS

The XRD patterns of the supports and the catalyst are shown in **Figure 4.20**. The peaks located at 2θ = 36.8, 42.8, 62.4, 75.4 and 79° for all catalysts could be attributed to the (1 1 1), (2 0 0), (2 2 0), (3 1 1) and (2 2 2) planes of cubic structure of NiO. The broad diffraction peak at approximately 21.3° (1 0 0) was assigned to amorphous SiO_2 [81].The strong peak located at 25.9° and the weaker ones at 2θ = 42.6° in the CNTs-SF-E catalyst was attributed to the graphite of CNTs [92]. Weak diffraction peak of NiO was observed in the CNTs-SF-E catalyst, indicating that a better dispersion of NiO crystallites on the CNTs-SF-E catalyst. The average Ni particle sizes calculated from XRD patterns by using Scherrer's equation (**Table 4.4**). It can be observed that particle sizes of NiO increased with increasing Ni loading due to the

aggregation of Ni metal at higher loadings. The metal size for the CNTs-SF-E catalyst

was quite small (6.8-7.3 nm) while the average crystal size of Ni particles over 10NiSP

and 10NiSF catalysts were about 14 nm and 22 nm, respectively. The high dispersion

and small average crystal size of Ni particles over the fibrous CNTs-SF-E suggested that

the presence of CNTs on silica fiber could significantly enhance metal dispersion. This

may be due to that CNTs-SF-E possessed a large number of oxygen functional groups

along with the defects of CNTs structure, which could effectively stabilize the highly

metal dispersion [5].

Table 4.4 The average nickel particle sizes of supports and catalysts

Samples	d_{XRD} (nm)[a]		d_{TEM} (nm)[b]	
	Fresh	Spent	Fresh	Spent
SP	-	-	-	-
SF	-	-	-	-
CNTs-SF-E	-	-	-	-
10NiSP	14.0	29.4	10.7	32.5
10NiSF	20.2	30.1	15.0	25.6
5NiCNTs-SF-E	6.8	9.2	5.0	9.4
10NiCNTs-SF-E	7.3	11.5	8.7	15.2

d_{XRD}[a] = average nickel particle sizes derived from diffraction line in XRD corresponding to NiO

(2 0 0) plane at 42.8° for fresh and spent catalysts.

d_{TEM}[b] = average Ni particles sizes estimated on the transmission electron microscopy for fresh and

spent catalysts.
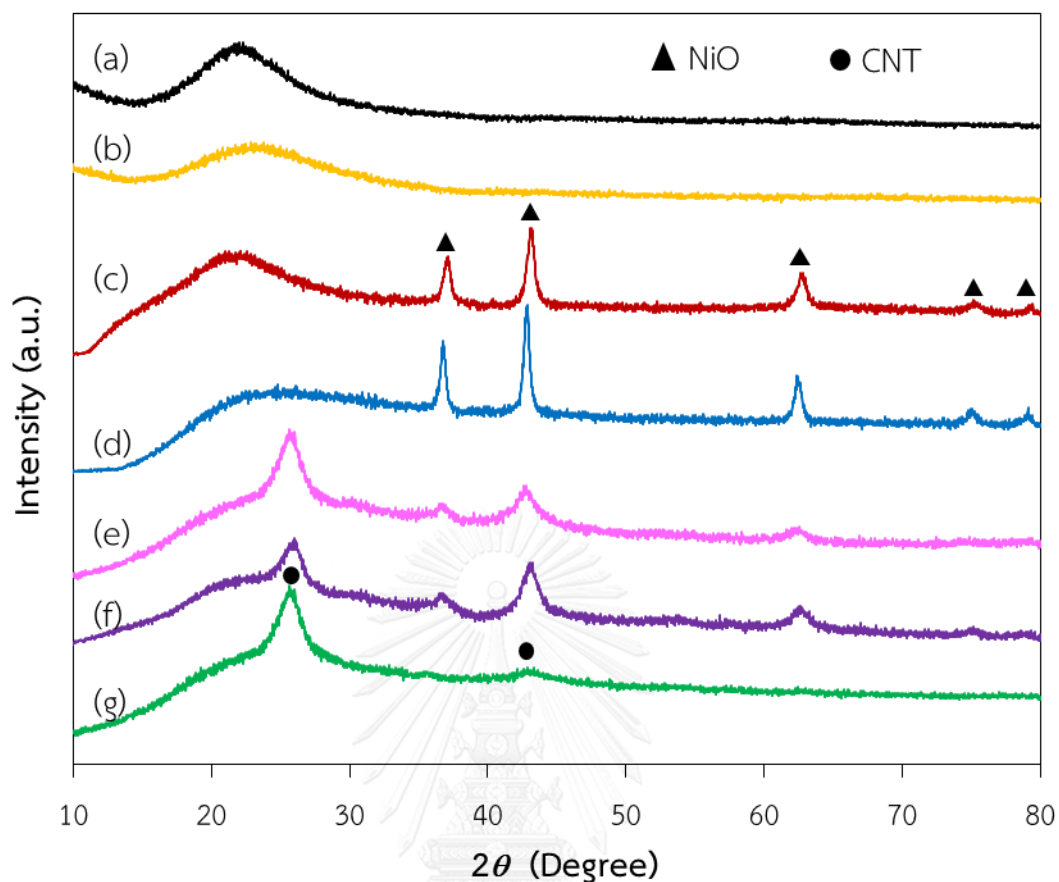
Figure 4.20 XRD patterns of the fresh catalysts (a) SP, (b) SF, (c) 10NiSP, (d) 10NiSF, (e) 5NiCNTs-SF-E, (f) 10NiCNTs-SF-E and (g) CNTs-SF-E

The reduction performance of the prepared catalysts was investigated by H_2-TPR analyses and the profiles are showed in **Figure 4.21.** There were two reduction peaks for 10NiSP and 10NiSF. The first peak of 10NiSF appeared at about 380 °C and 10NiSP centered at 420 °C could be assigned to the reduction of NiO having weak interactions with the support. It can be clearly seen that the first reduction peaks for Ni^{2+} to metallic Ni on SF catalysts shifted towards lower temperatures compared to 10NiSP, indicating that NiO clusters on the fiber catalysts were easier to be reduced.

The second weak reduction peak in all curves was associated with the reduction NiO species having strong interaction with support or smaller NiO particles. The temperature peak of 10NiSP could be ascribed to reduction of NiO particles confined within the mesopores [5]. , In case of 10NiCNTs-SF catalyst, there were three apparent reduction peaks. The first peak was assigned to the reduction of NiO on surface of SF. The second peak was corresponded to the reduction of bound and highly dispersed NiO on the exterior walls of the CNTs [93]. The presence of the third peak above 500 °C was assigned to the overlapping peaks of the reduction NiO species having strong interaction with support or smaller NiO particles and the gasification of CNTs via a reaction of H_2 with the carbon support.
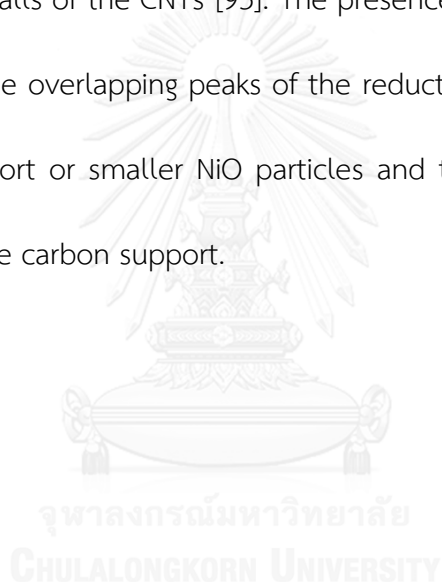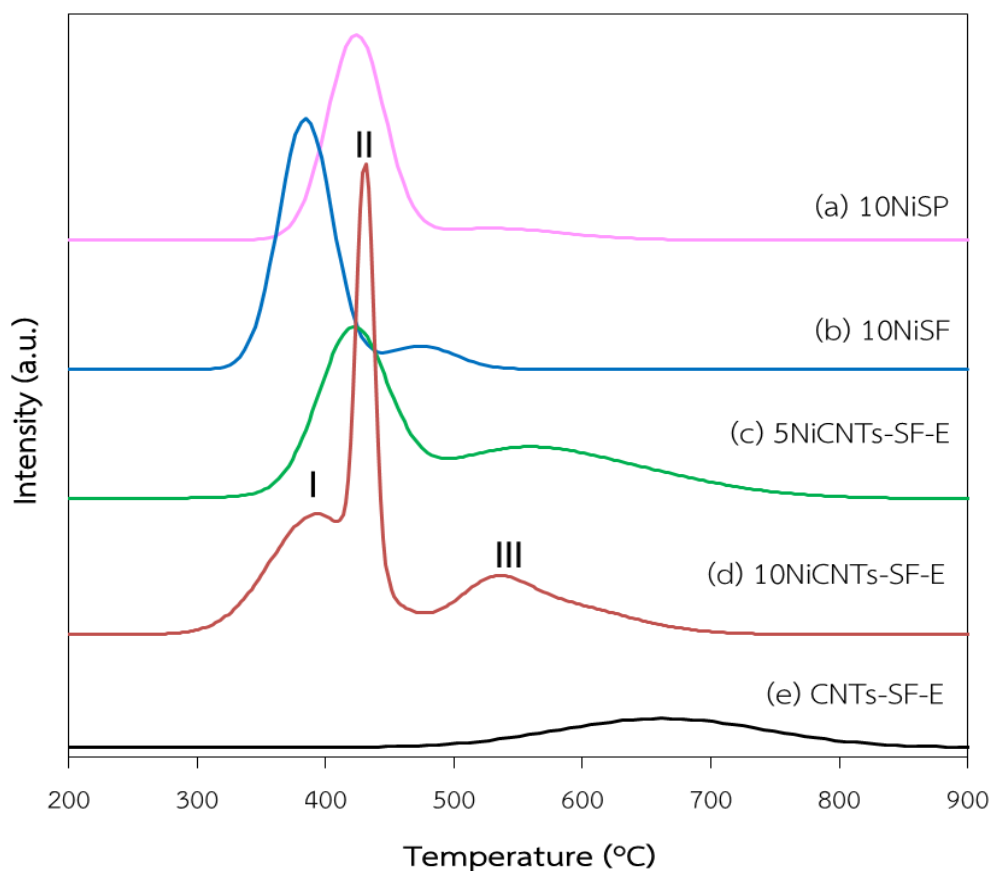
Figure 4.21 H_2-TPR profiles of the fresh catalysts (a) 10NiSP, (b) 10NiSF, (c) 5NiCNTs-SF-E, (d) 10NiCNTs-SF-E and (e) CNTs-SF-E

Figure 4.22 shows typical TEM images from (a) 10NiSP, (b) 10NiSF, (c) 5NiCNTs-SF-E and (d) 10NiCNTs-SF-E. Clearly, some small nickel nanoparticles (the dark dots in the TEM photos) were apparently located on the silica surface. The average particle size of metal estimated from TEM was about 10.7 nm, while the particles of 10NiSF catalyst were average size of 15 nm. In case of the CNTs-SF-E catalysts, it can be seen that most of the Ni metal particles were evenly dispersed on outside of the nanotubes. As for Ni loading content of 5 wt%, the average particle size of the metal phase was

about 5 nm, which was similar to the value derived from the XRD results by the

Scherrer's equation (**Table 4.3**). The increasing of Ni-loading from 5 to 10 wt% **(Figure**

4.22. (d)), the average Ni particle size slightly increased from 5.0 nm to 8.7 nm.
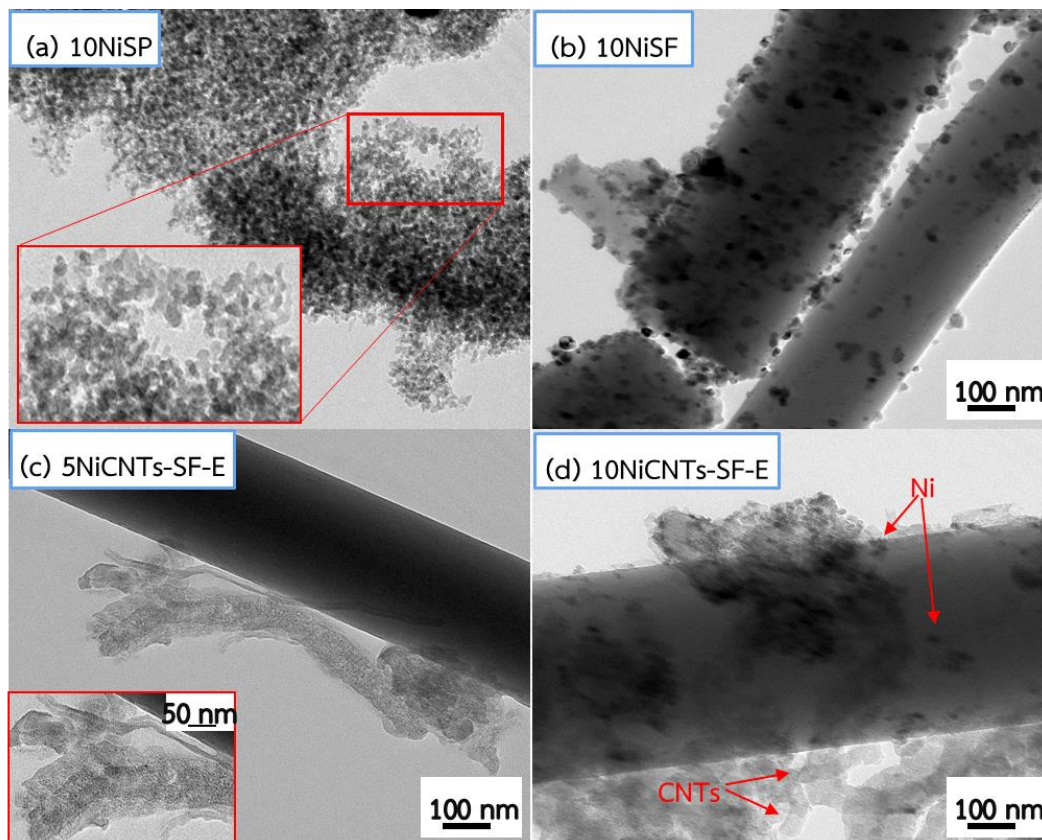
Figure 4.22 TEM images of the fresh catalysts (a) 10NiSP, (b) 10NiSF, (c) 5NiCNTs-SF-E
and (d) 10NiCNTs-SF-E

4.2.2 Catalytic performance

The effect of temperature on ethanol conversion and products distribution of

5NiCNTs-SF-E, 10NiCNTs-SF-E, 10NiSF, and 10NiSP was studied in the range between

300 and 500 °C is illustrated in **Figure 4.23**. At 350 °C, the order of activity in ethanol

conversion over all samples was as follow: 10NiCNTs-SF-E > 10NiSF > 10NiSP = 5NiCNTs-SF-E. With increasing temperature, the conversion of ethanol overall Ni-based catalysts increased significantly. Ethanol conversion on 10NiCNTs-SF reached complete conversion at low temperature as 400 °C. In contrast, the complete ethanol conversion over 10NiSF and 10NiSP could be accomplished at 450 and 500 °C, respectively. The order of catalytic activity of the investigated catalysts was found as 10NiCNTs-SF-E > 10NiSF > 10NiSP = 5NiCNTs-SF-E. The 10NiCNTs-SF-E catalyst exhibited significantly higher ethanol conversion as compared with the other catalysts, indicating that the CNTs-SF-E composite as a support could improve catalytic activity. H_2, CO_2, CO and CH_4 were the dominant products measured in the outlet gas steam from steam reforming of ethanol. Acetaldehyde and trace of ethylene and ethane were detected overall the tested catalysts at low temperatures. The presence of acetaldehyde was produced from decomposition of ethanol. The trace of ethylene suggested the dehydration of ethanol, while negligible amount of ethane was ascribed to hydrogenation of ethane. At low temperature, C_2 product (ethylene, ethane and acetaldehyde) were detected on all catalysts due to weaker ability of breaking the C-C bond of Ni at low temperatures. As reaction temperature increased, acetaldehyde selectivity and CH_4 decreased significantly, while the concentration of H_2 and CO_2 increased. This can be explained by a change in the favorability of steam reforming and water gas shift reactions when temperature increased, as a result ethanol was

converted completely and selectivity of H_2 and CO_2 increased significantly [94]. In addition, the decrease of methane concentration at higher temperature could be attributed to the occurrence of methane reforming reaction [59]. The CNTs-SF-E catalyst exhibited relatively higher activity catalytic performance than 10NiSP and 10NiSF catalysts at low temperature, primarily due to small Ni metal particles and highly dispersed on the support resulting in excellent capability to access Ni active sites. The maximum H_2 yield on 10NiCNTs–SF-E was 50% at reaction temperature of 500 °C, while the maximum H_2 yield for was 47% for 10NiSF under the same condition. The order of H_2 yield at 500 °C was as follows: 10NiCNTs-SF-E > 10NiSF > 10NiSP >5NiCNTs-SF-E. The CNTs-SF-E catalyst exhibited higher H_2 yield than other tested samples at low temperature rang. Although 5NiCNTs-SF-E exhibited the lowest H_2 yield, the activity and selectivity of this catalyst was quite similar to 10NiSP. It was clearly seen that the catalytic performance of the catalysts were enhanced by using the CNTs-SF-E supported catalyst. This may be due to that CNTs-SF-E had large specific surface areas and were inherently tubular structure, could efficiently enhance active Ni metal dispersion as well as improve capability to facilitate the adsorption of reactants [95, 96]. According to present characterization results, it was clearly that the catalytic performance could be matched well with several factors. First, the CNTs-SF-E revealed high surface area and nickel metal dispersion as shown in **Table 4.3** and observed by hydrogen temperature-programmed reduction (**Figure 4.21**) and TEM images (**Figure 4.22**). In addition, the surface of CNTs-SF-E had highly crystalline form of graphite and

the formation of carbonyl groups which could enhance interaction between the active species with the CNTs-SF-E resulting in high active species dispersion, which may delivered the highest initial activity. Similar results have been obtained by López et al. [97]. Second, the average Ni metal particles on the CNTs-SF-E catalysts (about 7.3 nm) exhibited obviously smaller than the particle sizes on 10NiSP (about 14 nm) and 10NiSF (about 20 nm). Indeed, high catalytic activities of ethanol steam reforming correlated with the decrease of the crystallite size [98]. In addition, the unique tubular structure together with electronic properties of CNTs may facilitate capability of electrons transfer between the support and active species and adsorbed the reactants, which resulted in accelerating the catalytic properties of Ni particles [99]. Therefore, the high catalytic activities and production of H_2 on the CNTs-SF-E catalyst could be attributed to alteration of the catalyst properties.
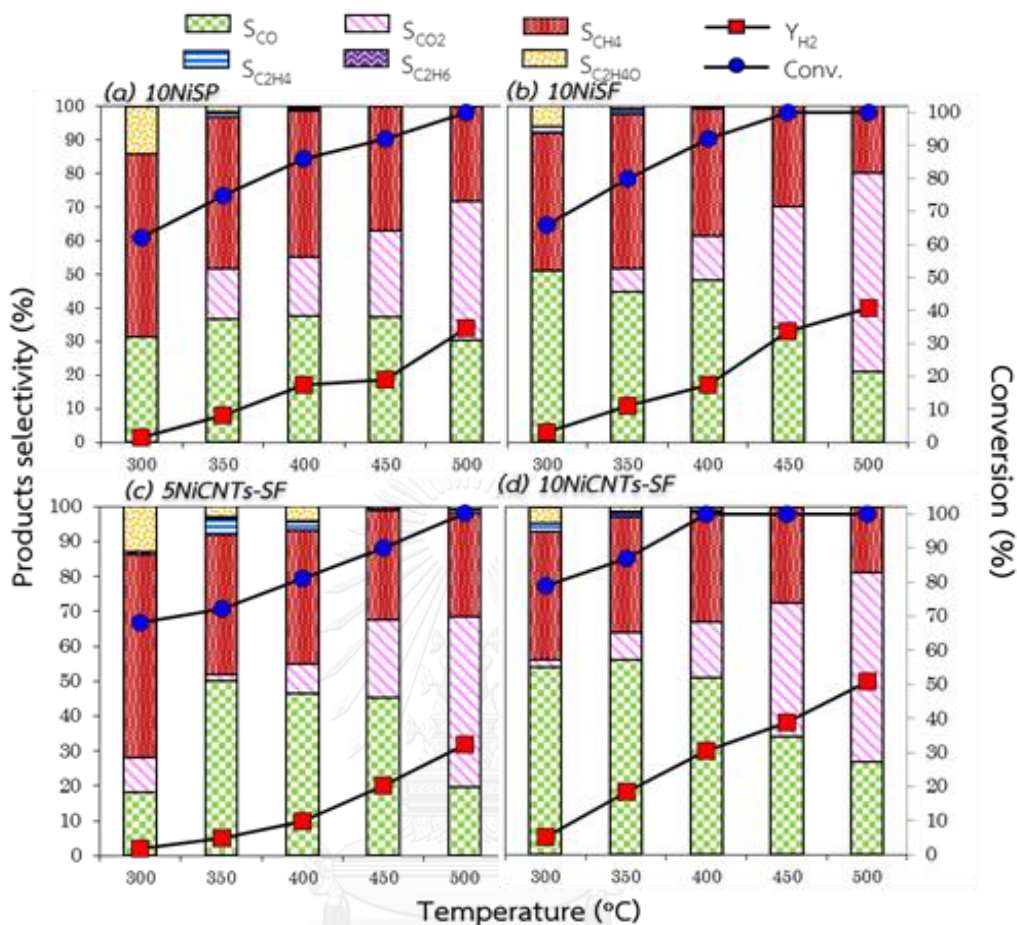
Figure 4.23 Influence of reaction temperature on ethanol conversion and products distribution over (a) 10NiSP, (b) 10Ni/SF, (c) 5NiCNTs-SF-E, and (d) 10NiCNTs-SF-E for SRE reaction at W/F = 18 g_{cat}h/mol, S/C = 9

4.2.3 Catalytic stability and characterization of spent catalysts

The stability performance of catalysts was tested for 22 h at 450 °C and the results are displayed in **Figure 4.24**. The conversion for all catalysts except 10NiSP almost remained at a constant for all time on steam. In contrast, an apparent decline of catalytic activity was observed for 10NiSP catalyst. The results suggested that the

fiber catalysts could improve catalytic stability. The fiber catalysts which were inherently unique tubular structure could be the main reason for superior catalytic stability compared to conventional porous Ni catalyst. The unique tubular structure of fiber catalysts possessed high accessibility of Ni active sites, which could improve contact between Ni metal and reactants and thus kept high activity and stability [99]. This will be discussed in TEM and TG/DTA results.
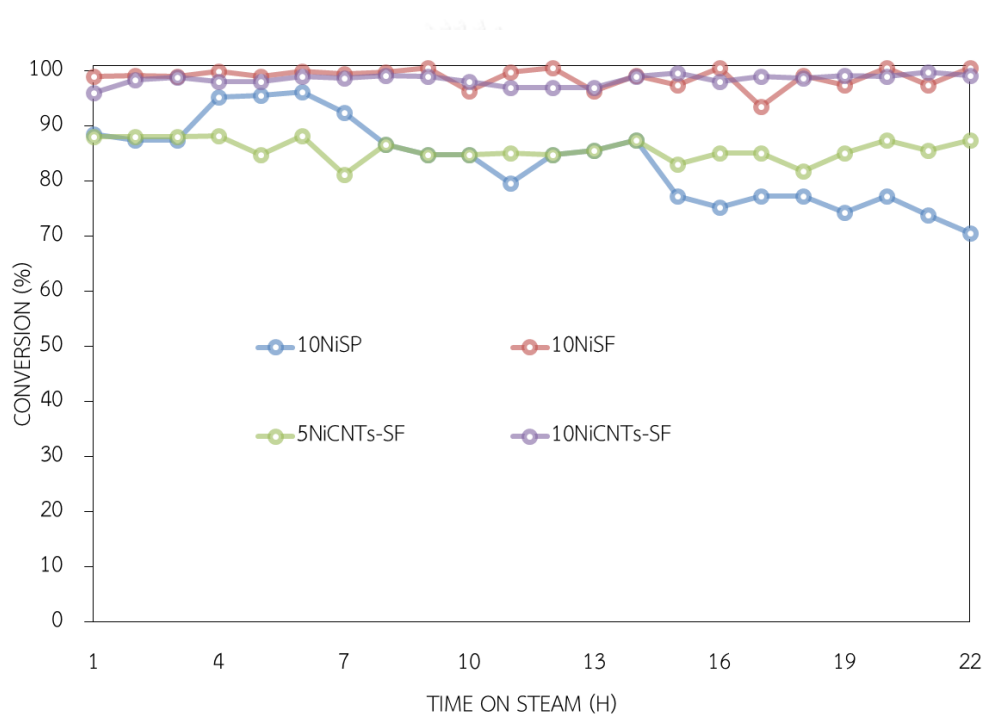
Figure 4.24 Time on steam profiles of the catalysts with reaction conditions: T = 450 °C, S/C = 9, and W/F = 18 g_{cat}h/mol

The catalysts after reaction at 450 °C for 22 h were analyzed by TEM, as showed in **Figure 4.25**. The spent 10NiSP catalyst was mostly surrounded by amorphous carbon and some carbon nanotubes were observed. Over fiber catalysts, carbon nanotubes

were mainly formed and large Ni particles were observed at the top of carbon nanotubes. The presence of Ni particles on the top of carbon nanotubes over the fiber catalysts indicated that Ni particles were still more accessible to reactants. Therefore, it was the reason why the fiber catalysts exhibited excellent catalytic stability. On the contrary, active sites of 10NiSP were formed and covered by carbon, leading to loss their activity and decrease catalytic activity after 14 h of the experiment. In addition, the large Ni particles approximately 28 nm and 25 nm were found on 10NiSP and 10NiSF, respectively, while, the average Ni particles of 5NiCNTs-SF-E and 10NiCNTs-SF-E were 9.2 and 11.5 nm, respectively. The large Ni particles could be attributed to the sintering and movement of active Ni species on the external surface of the catalyst due to relative with interaction between metal with support [100]. The average Ni particles of the CNTs-SF-E catalysts were negligible changed, suggesting that the migration and sintering of Ni particles over the CNTs-SF-E supported catalysts were effectively suppressed. This was mainly attributed to the stronger of the metal-support interaction, which could effectively stabilize Ni^0 particles, leading to keep highly dispersed of Ni on the CNTs-SF-E catalysts, as shown in H_2-TPR and XRD results.
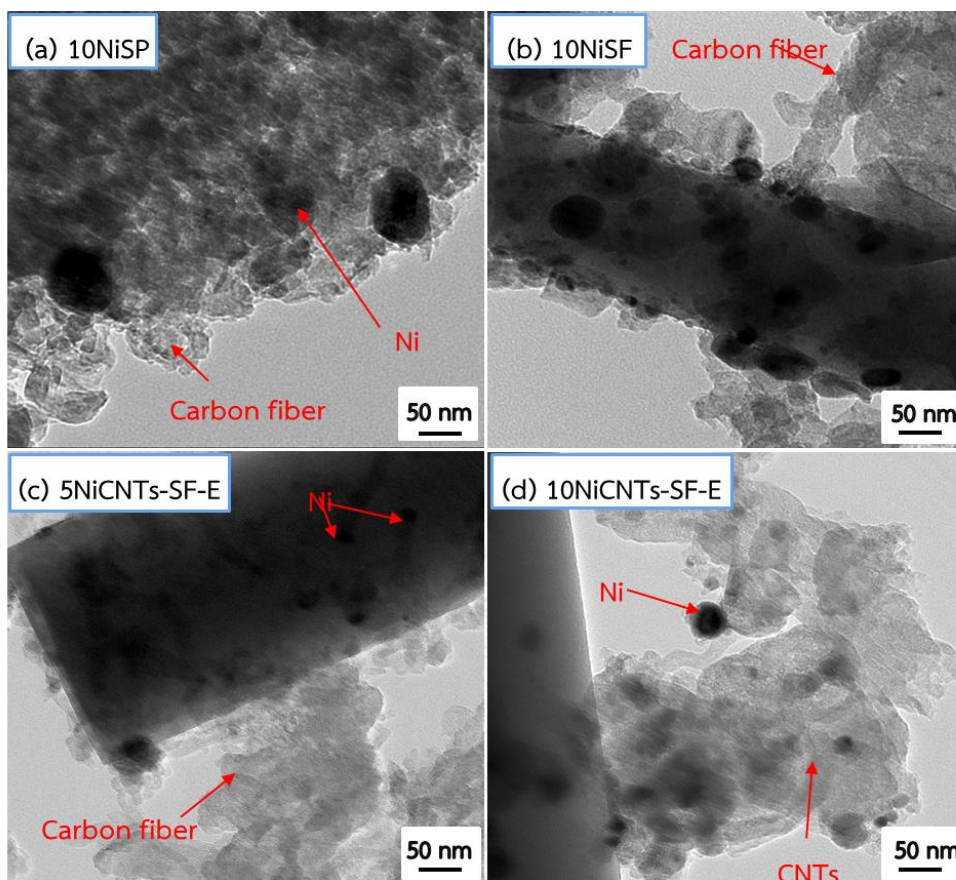
Figure 4.25 TEM images of the spent catalysts (a) 10NiSP, (b) 10NiSF, (c) 5NiCNTs-SF-E and (d) 10NiCNTs-SF-E

The XRD patterns of spent catalysts are presented in **Figure 4.26**. The reflection peaks of all catalysts observed at 2θ of 26 and 42° were assigned to the graphite of CNTs [36]. The peaks located at 2θ = 44, 51 and 73° for all catalysts could be attribute to metallic Ni phases after reduction. The intensity of carbon peak over 10NiSP was comparatively higher than that of the carbon peak in 10NiSF, indicating that carbon formation was more significant over 10NiSP. The average Ni crystallite sizes of all catalysts increased after the SRE reaction as following sequence: 10NiSF (30.1 nm) >

10NiSP (29.5 nm) > 10NiCNTs-SF-E (11.5 nm) > 5NiCNTs-SF-E (9.2 nm), as also shown in

Table 4.4. The large particle sizes of spent catalysts without CNTs could be assigned

to sintering due to weak the metal-support interaction [50]. In contrast, the Ni

crystallite sizes of the CNTs-SF-E catalysts were negligible changed after 22 h of the

experiment, which was in good agreement with TEM results. This suggested that the

CNTs-SF-E catalysts were excellent anti-sintering performance.
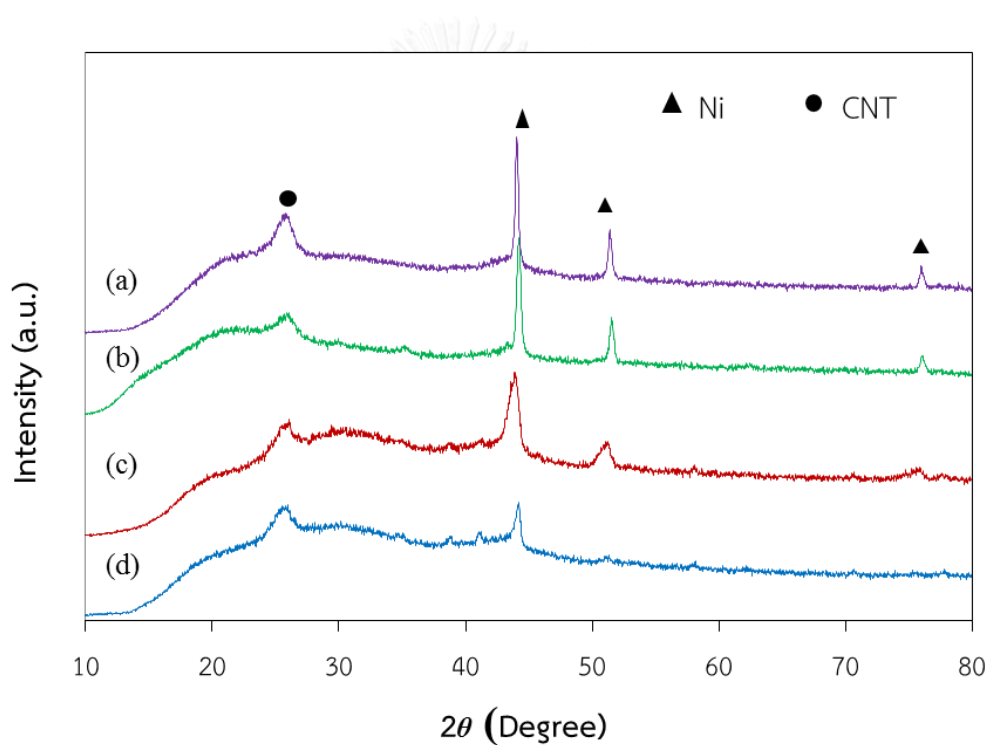
Figure 4.26 XRD patterns of the spent catalysts (a) 10NiSP, (b) 10NiSF, (c) 5NiCNTs-SF-E and (d) 10NiCNTs-SF-E

Thermogravimetric and differential thermal analysis (TG/DTA) was carried out

in order to quantify the amounts of carbon deposited on spent catalysts as shown in

Figure 4.27. According to the literature [88], there are two types of carbon deposition

on catalyst during steam reforming reaction which was amorphous carbon and graphitized carbon, such as CNTs. The amorphous carbon is generated by polymerization reactions of C_2+ products ($C_2H_4 \longrightarrow n(C_2H_4)$) and CNTs is formed by the decomposition of methane ($CH_4 \longrightarrow C + 2H_2$) and/or the Boudouard reaction ($2CO \longrightarrow CO_2 + C$) [39]. In addition, oxidation temperature of amorphous carbon was below 500 °C, whereas CNTs started to burn at temperature range 500-750 °C [88]. In our case, 10NiSP had three distinct weight loss stages in the temperature ranges between 400-550 °C, 550-690 °C and 690-800 °C. The weight loss at the first peak was attributed to the decomposition of amorphous carbon, as evidenced by TEM. The weight loss at the second peak was assigned to the removal of CNTs of larger size (less-stable CNTs) and stable SWNTs, which were consistent with the former reports [88]. The weight loss at the third peak was assigned to CNTs with smaller size (stable CNTs). In case of 10NICNTs-SF-E, only one oxidation peak was observed above 600 °C oxidation, which was assigned to the oxidation temperature of CNTs. In case of 10NiSF and 10NiCNTs-SF-E catalysts, there were two weight loss stages at approximately 690-700 °C and 700-800 °C. The results suggested that amorphous carbon was not formed on both fiber catalysts. This further confirmed only the high thermal stability of multiwall carbon nanotubes deposited over the fiber catalysts. This result was consistent with the TEM results. Moreover, stable CNTs were found to be increased and shifted to higher temperatures for 10NiCNTs-SF catalyst due to CNTs formation

after steam reforming reaction. The amount of coke formation over spent 10NiSP and 10NiSF was 45% and 30%, while approximately 5% and 10% was observed on spent 5NiCNTs-SF-E, and 10NiCNTs-SF-E, respectively. It was well-known that the amorphous carbon on Ni surface could significantly decrease the accessibility of active Ni sites by blocking the active site of metal, which led to deactivation of catalyst activity [50]. The oxidation temperature peak of spent 10NiSP catalyst exhibited the presence of amorphous, stronger intensity and larger peak area compared to that of the fiber catalysts, suggesting that more carbon deposition was formed on10NiSP surface. This should be the reason of the decrease of the catalytic activity on 10NiSP after 14 h of the experiment.
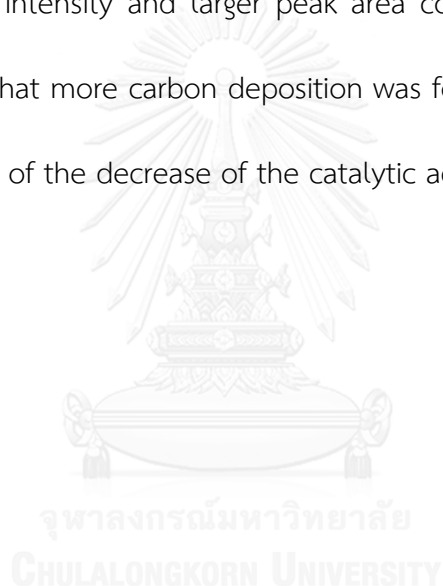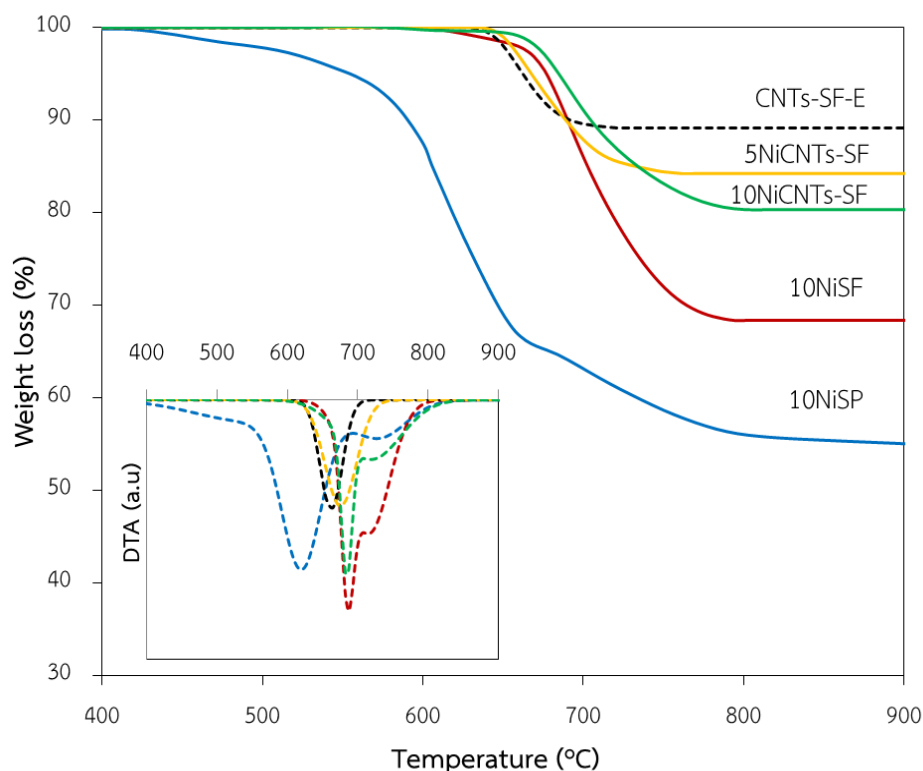
Figure 4.27 TG/DTA profiles of the spent catalysts

Combining the characterization techniques of used catalysts from TEM, XRD and TG/DTA, it can be concluded that the fiber catalysts exhibited lower amount of carbon deposition than conventional porous catalyst due to tubular structure, which enhanced accessibility of Ni active sites. However, the carbon deposition on 10NiSF was more severe compared to the CNTs-SF catalysts, confirmed by TEM, suggesting that 10NiCNTs-SF-E was more effective in suppressing the carbon formation. The excellent coking-resistance ability of the CNTs-SF-E catalysts could be associated with stronger metal to support interaction. As TEM and XRD results of used catalysts

revealed pronounced metal sintering for 10NiSF after 22 h reaction due to a weaker interaction between metal with support and lower metal dispersion. Comparatively, the CNTs-SF catalysts had a stronger interaction between metal with support and a better metal dispersion as oxygen groups along with the defects of CNTs structure may also prevent sintering in the catalytic reaction [87]. Therefore, the CNTs-SF-E catalysts exhibited excellent coking-resistance ability compared to 10NiSF catalyst. Moreover, the unique tubular structure and large area of π-electron cloud of the CNTs could improve electrons transfer between the support and active species and adsorbed the reactants which could accelerate the rate of carbon gasification, thus improving the catalytic stability [95]. In addition, carbon deposition on CNTs-SF-E catalysts took place on active interface between nickel and coexisted CNTs as well as continuously lifted up nickel metal clusters, resulting in the tube-length extension of the existing CNTs following the tip-growth mechanism. Therefore, carbon formation over the CNTs-SF catalysts had no effect on losses of active Ni species and the stability, achieving improved long-term stability.

4.3 Synthesis of carbon nanotubes-silica fibrous composite (CNTs-SF-A) by acetic acid steam reforming and its use as a novel catalyst support for acetic acid steam reforming

In this section a carbon nanotubes-silica fibrous composite (CNTs-SF-A) was synthesized by acetic steam reforming using the optimum condition from the first part.

CNTs-SF-A was characterized by TEM, TG/DTA, XRD and BET and applied as a support for Ni-based catalyst to produce hydrogen production from acetic acid steam reforming.

4.3.1 Synthesis of CNTs-SF-A by acetic acid steam reforming acid

The CNTs-SF-A was synthesized by acetic steam reforming using Ni loading of 30 wt%, W/F of 9 g_{cat}h/mol, reaction temperature of 600 °C and S/C of 1. **Figure 4.28 (a)** shows TEM images of the spent 30NiSF catalyst. Different morphologies of carbon were formed by acetic acid steam reforming were obviously observed. These carbons could be classified into two types on the basis of the structures. One was CNTs with a broad diameter distribution. The outer diameter was in range of 20-50 nm and inner diameters were between 5-11 nm. Another type was thick filaments rolled up into shapeless tangles and capsules around metal particles. The morphology of carbon synthesized from ethanol steam reforming was obviously different as shown in **Figure 4.28 (b)**. There were mainly thick-walled tubes with narrow diameters range of 22-30 nm and metal particles were seen on the tips of tubes. It was clearly seen that the CNTs produced from acetic acid steam reforming was larger outer diameters and a shorter length as compared to CNTs obtained from ethanol steam reforming. In addition, most of the product consisted of curled shape structures. According to the growth mechanism of CNTs, the carbon species dissolved in the metal particle and diffused through it until carbon surface supersaturation on the metal particles and

further precipitated in form of carbon filament [57]. On the other hand, if the carbon species on the metal particles were not enough it would precipitate surround on the metal particles and cover the whole surface of the particle eventually [101]. It had been reported that different carbon sources played an important role to determine the morphology of carbon deposits. Although feeding C atom by ethanol is the same as acetic acid, acetic acid contains more oxygen atoms than ethanol. Different oxygen atoms of both feed could make them exhibit different behaviors in carbon formation. It is known that oxygen atoms have been suggested to remove carbon formation on the catalyst surface [102-104]. In case of acetic acid containing two oxygen atoms, carbon formation on nickel particles might be attacked by two oxygen atoms which led to decrease the carbon contents on surface of nickel particles. Therefore, carbon contents on nickel particles did not enough to form CNTs.
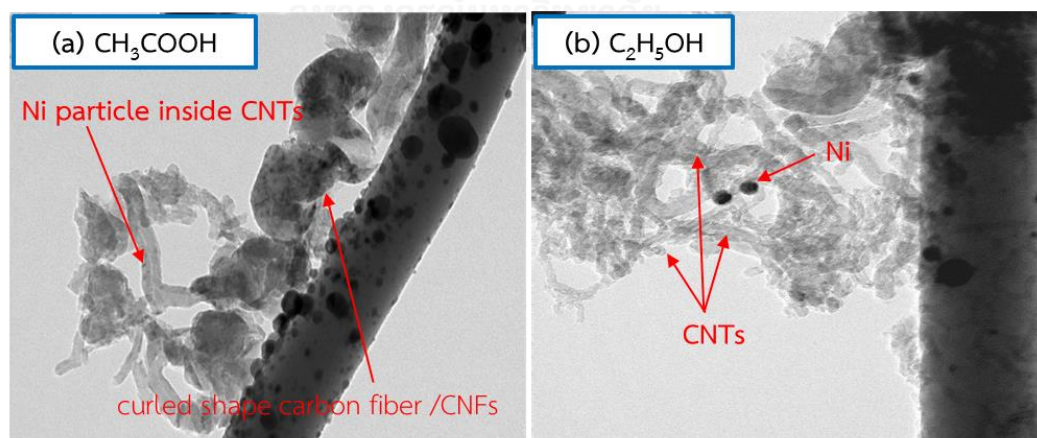
Figure 4.28 TEM images of CNTs formed by acetic acid steam reforming (a) and ethanol steam reforming (b) over 30NiSF at 600 °C

Thermogravimetric and differential thermal analysis (TG/DTA) of 30NiSF catalysts after acetic acid steam reforming and ethanol steam reforming is presented in **Figure 4.29**. Both samples exhibited one weight loss stage above at approximately 650 °C. The amount of carbon formation over 30NiSF after acetic acid steam reforming was 40%, while approximately 60% was observed on 30NiSF after ethanol steam reforming. The results indicated that the amount of carbon formation produced from acetic acid steam reforming was relatively higher than that from ethanol steam reforming.
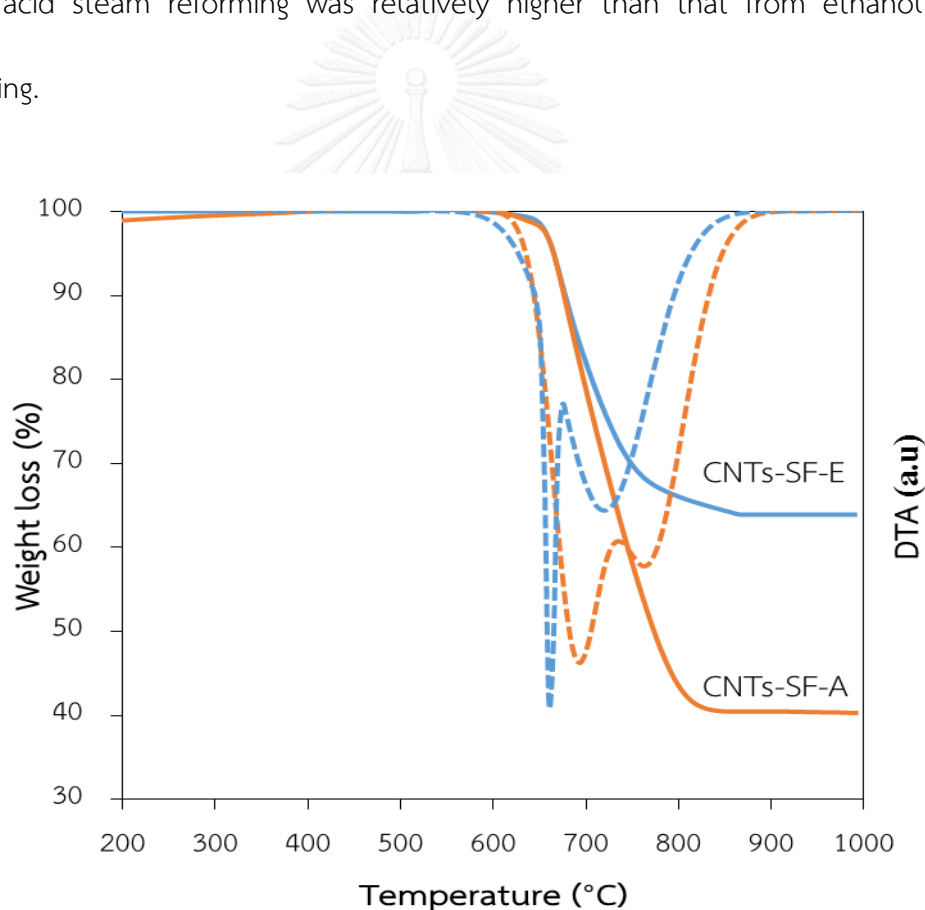
Figure 4.29 TG/DTA profiles of the spent 30NiSF from ethanol steam reforming and acetic acid steam reforming

4.3.2 Purification of NiCNTs-SF-A

After reaction the NiCNTs-SF-A were purified by treatment with acids to remove the Ni catalysts to obtain CNTs-SF-A. After purification scanning electron microscopy with Energy dispersive X-ray spectrometer was used to measure composition of CNTs-SF-A after acid treatment and the results are shown in **Figure 4.30**. The CNTs-SF-A composite after purification composed of carbon 86.19%, oxygen 11.16%, silicon 2.30% and chlorine 0.35%. The results indicated that Ni catalyst was not observed by EDX analysis suggesting that metal removal was achieved. However, 0.35% of chlorine from HCl was still found.
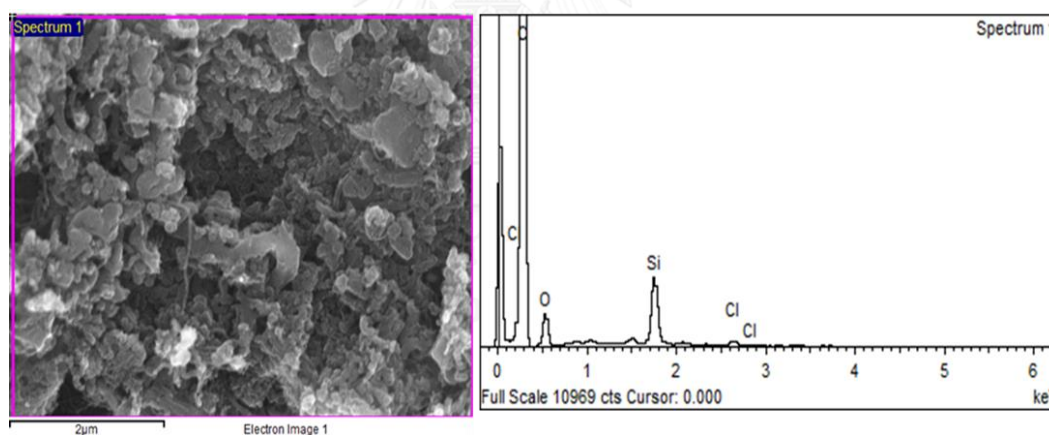
Figure 4.30 Elemental compositions of CNTs-SF-A after purification

Figure 4.31 shows SEM images of purified CNTs-SF-A produced from acetic acid steam reforming at Ni loading of 30 wt%, W/F of 9 g_{cat}h/mol, reaction temperature of 600 °C and S/C of 1. It can be seen that the SF was fully covered by CNTs with large

and small diameters. The average diameter of CNTs-SF-A was approximately 35-50 nm, while the average diameter of CNTs-SF-E was 20-30 nm. It was clearly seen that the CNTs produced from acetic acid steam reforming was larger as compared to CNTs produced from ethanol steam reforming and aggregated together, which was consistent with the TEM results.
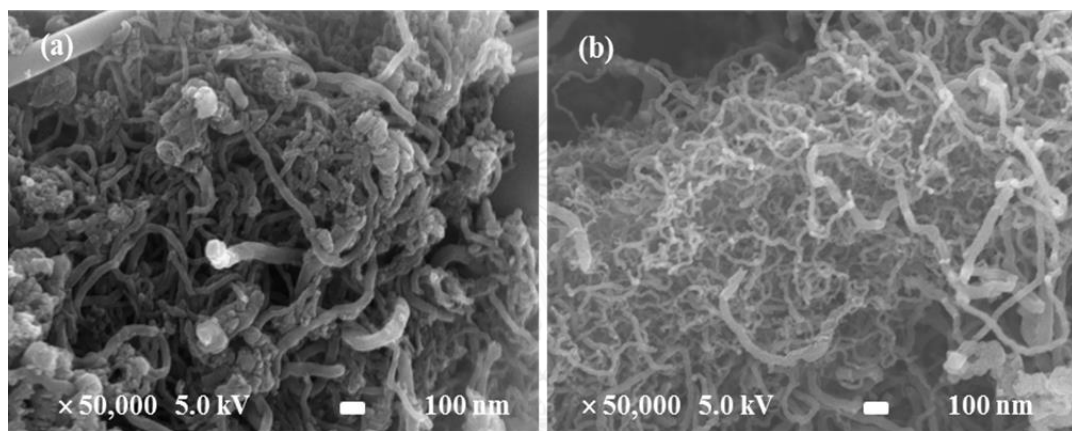
Figure 4.31 SEM images of CNTs formed by steam reforming of (a) acetic acid and (b) ethanol.
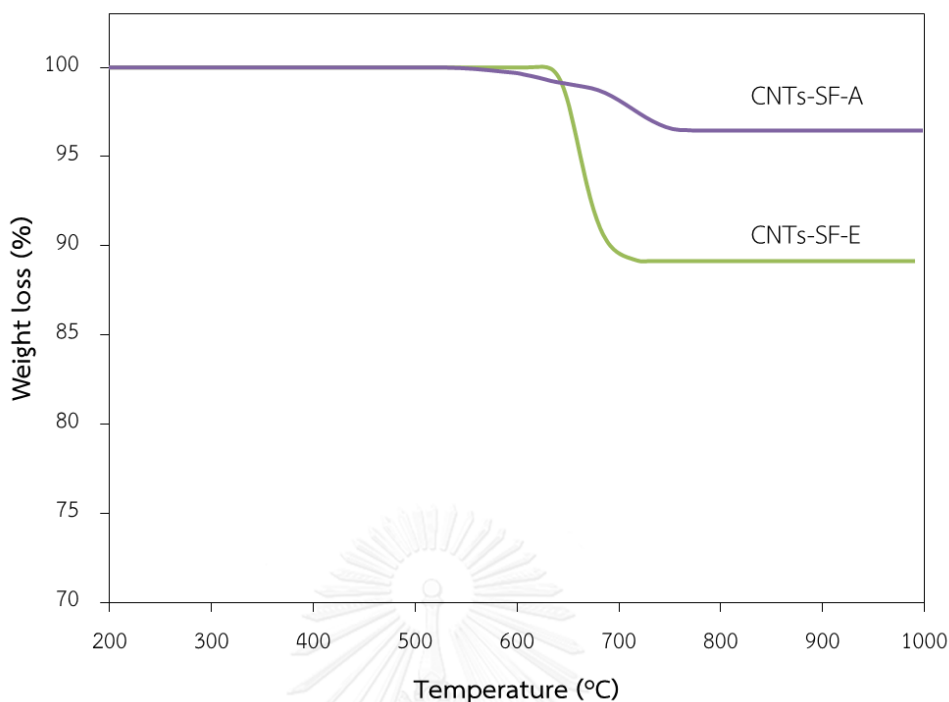
Figure 4.32 TG/DTA profiles of CNTs-SF-A and CNTs-SF-E

Figure 4.32 shows TG–DTA analysis of CNTs-SF-A and CNTs-SF-E. The result showed that the CNTs-SF-A and CNTs-SF-E composites exhibited only one peak at temperature range of 600-700 ℃, which attributed to oxidation temperature of CNTs. Total weight loss of composite obtained from acetic acid steam reforming before treatment with acids was about 60% **(Figure 4.29)**, while total weight loss after treatment was about 5 wt%. In case of the composite produced from ethanol steam reforming, the amount of carbon before treatment was 40 wt% **(Figure 4.29)** but after treatment was approximately 10 wt%. The decrease of carbon after treatment was attributed to the elimination of carbon impurity. It can be also seen that the amount

of carbon deposition before treatment in case of acetic acid was relatively higher as compared to ethanol. However, after treatment the amount of carbon from acetic acid was lower than that from ethanol. The results indicated that carbon deposition produced from acetic acid may mainly consist of unstable carbon with having interaction with silica fiber and/or without interaction with silica fiber that could be easily removed by acids [105].

The specific surface area of 30NiSF catalyst after acetic acid steam reforming and CNTs-SF-A as shown in **Table 4.5**. The results demonstrated that the specific surface of 30NiSF increased significantly from 19 to 133 m^2/g after acetic acid steam reforming. The total pore volume of 30NiSF also increased after the reaction. The specific surface area of CNTs-SF-A after removing Ni increased slightly from 133 to 175 m^2/g. This might be due to that the treatment led to open the tube tip, which allowed the nitrogen adsorption in the intertubular pores of CNTs resulting in increase in surface area [89, 105].

Table 4.5 The specific surface area of spent 30NiSF and CNTs-SF-A

Samples	Surface area (m^2/g)	Pore volume (cm^3/g)	Pore diameter (nm)
30NiSF	133	0.29	9.5
CNTs-SF-A[a]	175	0.40	10.5

[a] purified CNTs-SF produced from acetic acid steam reforming over 30NiSF

4.3.3 Synthesis of NiCNTs-SF-A

CNTs-SF-A produced by acetic steam reforming was used as a support for Ni catalyst. Results of the catalyst characterization, catalyst performance and comparison of the acetic steam reforming reaction with NiSF and NiSP were discussed. Results of characterization of spent catalysts were also discussed.

4.3.4 Characterization of NiCNTs-SF-A

The specific surface area and pore volume of the supports and the catalysts are presented in **Table 4.6**. The results demonstrated that BET surface area of SP, CNTs-SF-E and CNTs-SF-A was slightly reduced when loaded with 10 wt% Ni. These results suggested that the incorporation of Ni particles into the supports led to significantly decrease the specific surface area of the supports due to partial blockage of pore surface by NiO [91]. The specific surface area of the SF was quite small due to a non-porous structure [80].

Table 4.6 The specific surface area of the supports and the catalysts

Samples	Surface area (m²/g)	Pore volume (cm³/g)	Pore diameter (nm)
SP	236	1.160	11.8
SF	3	0.001	12.5
CNTs-SF-E	157	0.508	13.6
CNTs-SF-A	175	0.400	10.5
10NiSP	240	1.170	11.8
10NiSF	5	0.013	7.4
10NiCNTs-SF-E	132	0.245	10.7
10NiCNTs-SF-A	141	0.360	10.3

[a] Determined by EDS.

Figure 4.33 shows the XRD patterns of the supports and catalysts. The characteristic peaks of NiO were observed at 2θ of 36.8, 42.8, 62.4, 75.4 and 79° [11]. The broad diffraction peaks at 21.3° were associated with amorphous SiO_2 [81]. The peaks of located at 2θ of 26.2 and 42.5° were the characteristic peaks of the graphite structure of the CNTs [92]. The crystallite particles size of Ni can be calculated from XRD patterns by using Scherrer's equation (**Table 4.7**). The Ni particle size of NiCNTs-SF-A and NiCNTs-SF-E was 7.4 and 7.3, respectively. This indicated that the Ni particle size of these two samples is almost equal. The Ni particle sizes of 10NiSP and 10NiSF

catalysts were about 14 nm and 22 nm, respectively. Comparing with Ni particle sizes, NiCNTs-SF-A and NiCNTs-SF-E catalysts were smaller than 10NiSP and 10NiSF catalysts. These suggested that the presence of CNTs on SF could significantly enhance metal dispersion [96].

Table 4.7 The average nickel particle sizes of supports and catalysts

Samples	d_{XRD} (nm)[a]		d_{TEM} (nm)[b]	
	Fresh	Spent	Fresh	Spent
SP	-	-	-	-
SF	-	-	-	-
CNTs-SF-E	-	-	-	-
CNTs-SF-A	-	-	-	-
10NiSP	14.0	n.d	10.7	n.d
10NiSF	20.2	16.2	15.0	24.0
10NiCNTs-SF-E	7.3	7.1	8.7	11.2
10NiCNTs-SF-A	7.4	6.8	9.2	14.2

d_{XRD}[a] = average Ni particle sizes derived from diffraction line in XRD corresponding to NiO (2 0 0) plane at 42.8° for fresh and spent catalysts.

d_{TEM}[b] = average Ni particles sizes estimated on the transmission electron microscopy for fresh and spent catalysts.

n.d = Not detected.
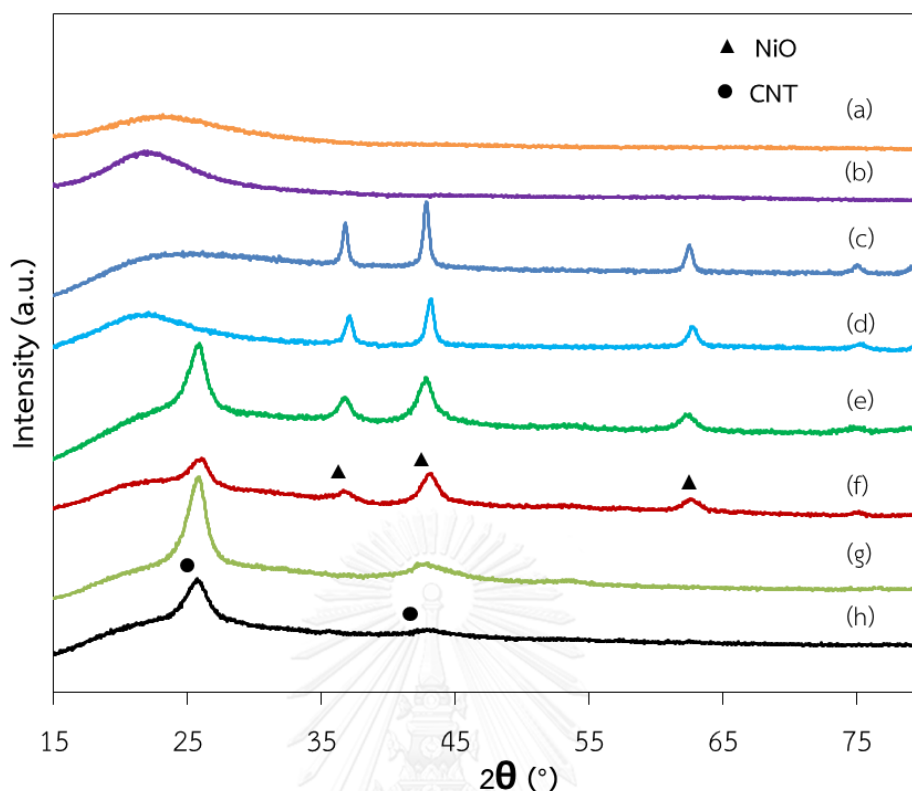
Figure 4.33 XRD patterns of the fresh catalysts (a) SF, (b) SP, (c) 10NiSF, (d) 10NiSP, (e) 10NiCNTs-SF-A, (f) 10NiCNTs-SF-E (g) CNTs- SF-A and (h) CNTs-SF-E

Figure 4.34 shows typical TEM images from (a) 10NiSP, (b) 10NiSF, (c) 10NiCNTs-SF and (d) 10NiCNTs-SF-A. Clearly, the silica surface was covered by some small nickel nanoparticles (the dark dots in the TEM photos). As for 10NiCNTs-SF-E and 10NiCNTs-SF-A, most of nickel nanoparticles were located outside of CNTs and CNFs. Nickel nanoparticles observed on 10NICNTs-SF-E was quite uniform dispersion, while some particles aggregated nickel nanoparticles was observed on 10NiCNTs-SF-A. The average size of nickel nanoparticles estimated from TEM is presented in **Table 4.7**. It can be seen that 10NiSF had nickel nanoparticles of 15 nm, while the smaller size of nickel

nanoparticles was obtained by using the support with the presence of CNTs on structure. The average size of nickel nanoparticles of 10NiCNTs-SF-E and 10NiCNTs-SF-A was about 8.7 nm and 9.10 nm, respectively. It can be seen that the support with the presence of CNTs on structure provided smaller size and good dispersion of nickel particles. This may be due to that pre-treatment of CNTs with acids could generate suitable location on the substrate for the nucleation and growth of small metal particles [93, 96].
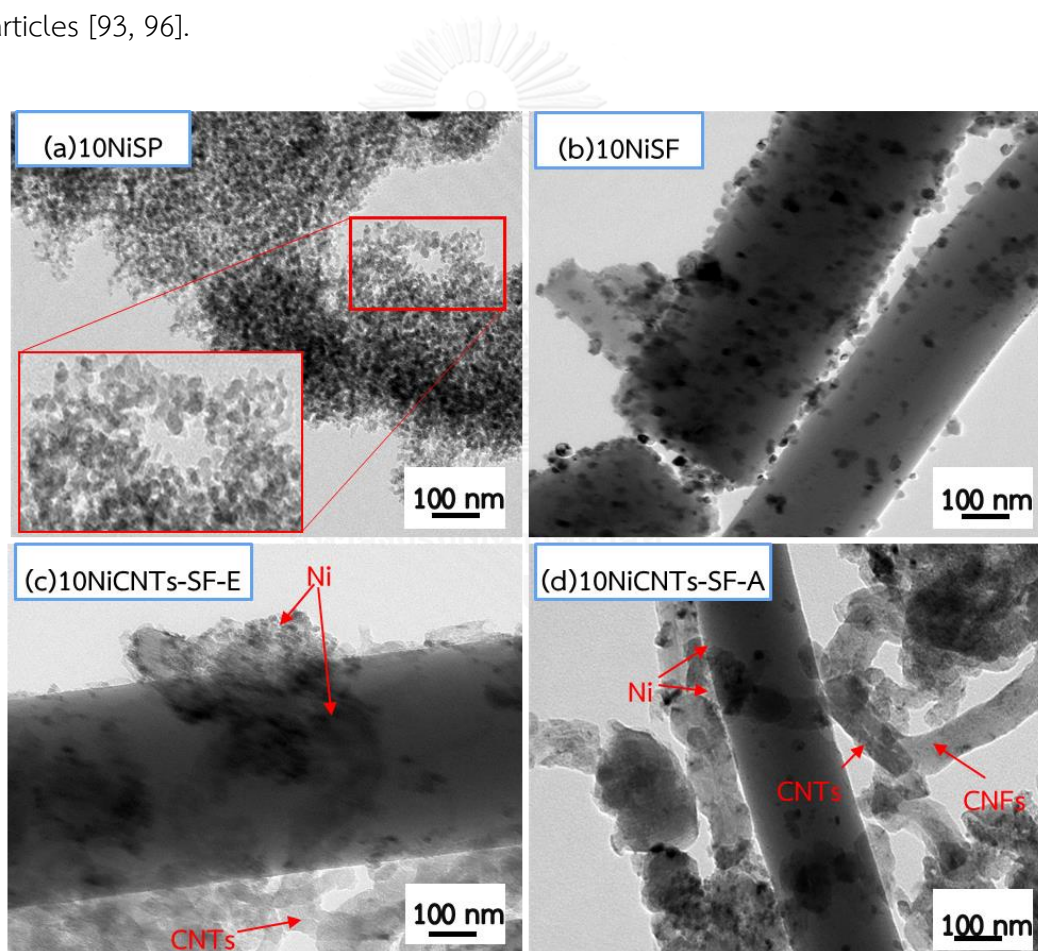
Figure 4.34 TEM images of the fresh catalysts (a) 10NiSP, (b) 10NiSF, (c) 10NiCNTs-SF-E and (d) 10NiCNTs-SF-A

4.3.5 Catalytic performance

The catalytic testing for acetic acid steam reforming of Ni with different supports is shown in **Table 4.8.** It can be seen that acetic acid conversion 10NiSP, 10NiSF and 10NiCNTs-SF-A was quite similar, while 10NiCNTs-SF-E exhibited really high activity. A maximum acetic acid conversion of 99% was achieved with 10NiCNTs-SF-E. The high activity of 10NiCNTs-SF-E was attributed to the presence of CNTs on the catalyst surface. From TG/DTA results above, the amount of CNTs on surface of 10NiCNTs-SF-E was higher as compared with 10NiCNTs-SF-A. Therefore, the highest activity of 10NiCNTs-SF-E might be related to CNTs on the catalyst surface since CNTs consists of graphene layers, involving π-electron density, which can efficiently promote electron transfer between metallic active sites and the support to the reactants [93, 96]. The main products observed in gas phase were H_2, CO, CO_2, and CH_4. All catalysts exhibited low H_2 yield. The formation of CO and CH_4 would greatly diminish H_2 yields in steam reforming. The presence of CH_4 suggested that decomposition of acetic acid (Eq. (4.11)) and methanation (Eq. (4.12)) proceeded due to low reaction temperature. Moreover, the formation of CO is an intermediate product that produced from incomplete acetic acid steam reforming or decomposition of acetic acid (Eq. (4.10)). CO may also be produced via the ketene (CH_2CO) intermediate and its further reaction to produce ethylene (Eq. (4.13 and 4.14)) [43].

Acetic acid steam reforming   : $CH_3COOH + 2H_2O \longrightarrow 2CO_2 + 4H_2$ (4.8)

Water gas shift : $CO + H_2O \longrightarrow CO_2 + H_2$ (4.9)

Decomposition : $CH_3COOH \longrightarrow 2CO + 2H_2$ (4.10)

: $CH_3COOH \longrightarrow CO_2 + CH_4$ (4.11)

Methanation : $CO + 3H_2 \longrightarrow CH_4 + H_2O$ (4.12)

Ketene : $CH_3COOH \longrightarrow CH_2CO + H_2O$ (4.13)

: $2CH_2CO \longrightarrow C_2H_4 + 2CO$ (4.14)
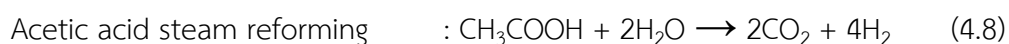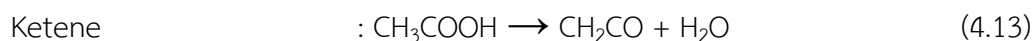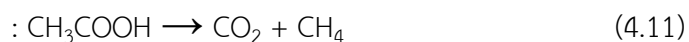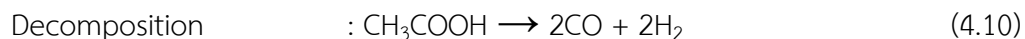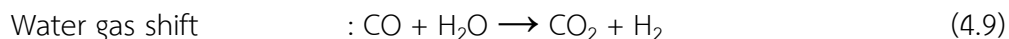
All catalysts exhibited different tendencies for the formations of CO and CH_4. A higher CO was obtained over 10NiSP and 10NiSF catalysts while a higher CH_4 was obtained over 10NiCNTs-SF-E and 10NiCNTs-SF-A. These indicated that 10NiCNTs-SF-E and 10NiCNTs-SF-A had the higher activities for the methanation reaction (Eq. (4.12)) and acetic acid decomposition reaction (Eq. (4.11)). In contrast, 10NiSP and 10NiSF catalysts were more selective to the decomposition of acetic acid to CO. The trace amounts of ethylene were also detected in the products of 10NiSP and 10NiSF catalysts. This indicated that CO was also produced via ketene (CH_2CO) intermediate and its further reaction (Eq. (4.13 and 4.14)).

Table 4.8 Catalytic testing of the catalysts at 400 °C, S/C = 9 and W/F = 18 $g_{cat}h/mol$

Catalysts	Conv.		Selectivity (%)				
		Y_{H_2}	CO	CO_2	CH_4	C_2H_4	C_2H_6
10NiSF	85	20	31.7	58.9	8.8	0.4	0.0
10NiSP	90	26	18.1	66.8	13.9	0.4	0.5
10NiCNTs-SF-E	99	27	7.7	66.2	25.7	0.0	0.2
10NiCNTs-SF-A	91	24	5.6	68.7	25.3	0.0	0.3

4.3.6 Characterization of spent catalysts

The catalysts after reaction at 400 °C for 4 h were analyzed by TEM, as depicted in **Figure 4.35**. The surface of spent 10NiSP catalyst was mostly covered by amorphous. Over fiber catalysts, carbon nanotubes were mainly formed and large Ni particles were observed at the top of carbon nanotubes. The presence of Ni particles on the top of carbon nanotubes over the fiber catalysts indicated that Ni particles were still more accessible to reactants. In addition, the large Ni particles approximately 24 nm were found on 10NiSF, while, the average Ni particles of 10NiCNTs-SF-E and 10NiCNTs-SF-A were 11.2 and 14.2 nm, respectively. The average Ni particles of 10NiSF were difficult to find because most surface 10NiSP catalyst was covered by carbon. The large Ni particles could be attributed to the sintering and movement of active Ni species on the external surface of the catalyst due to relative with interaction between metal with support [100]. The average Ni particles of the CNTs-SF-E catalyst were slightly

changed. This was mainly attributed to the stronger of the metal-support interaction, which could effectively stabilize Ni^0 particles, leading to keep highly dispersed of Ni on the CNTs-SF catalysts.
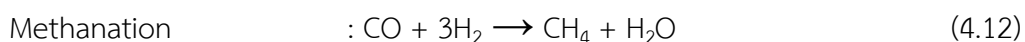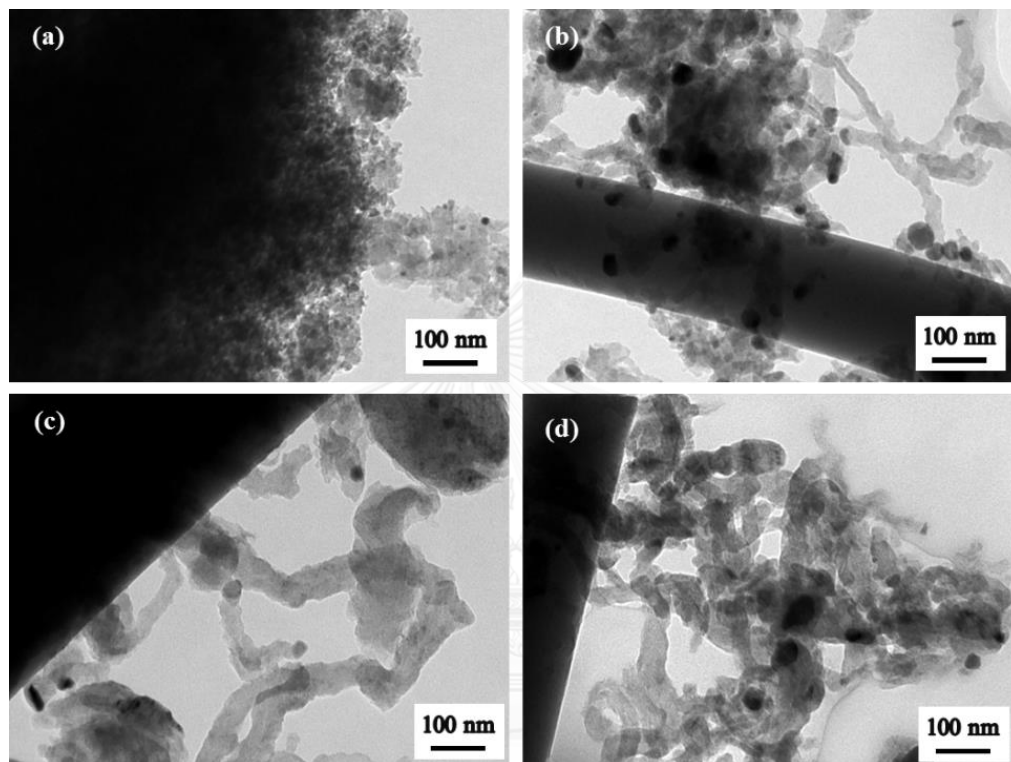

Figure 4.35 TEM images of the spent catalysts (a) 10NiSP, (b) 10NiSF, (c) 10NiCNTs-SF-E and (d) 10NiCNTs-SF-A

The XRD patterns of the spent catalysts are presented in **Figure 4.36.** The reflection peaks of all catalysts observed at 2θ of 26 and 42° were assigned to the presence of graphitic carbon [100]. In case of NiSP catalyst, no bulk diffraction peak of Ni was detected because metal particles were covered by many carbon layers, which was in good agreement with TEM results. The average Ni crystallite sizes of 10NiCNTs-

SF-E and 10NiCNTs-SF-A catalysts increased after the reaction as shown in **Table 4.7**. The large particle sizes of spent catalysts could be assigned to sintering due to weak the metal-support interaction [106]. These results were also consistent with the TEM results. However, different results were observed on 10NiSF catalyst. The metal particle sizes of 10NiSF catalyst decreased after the reaction.
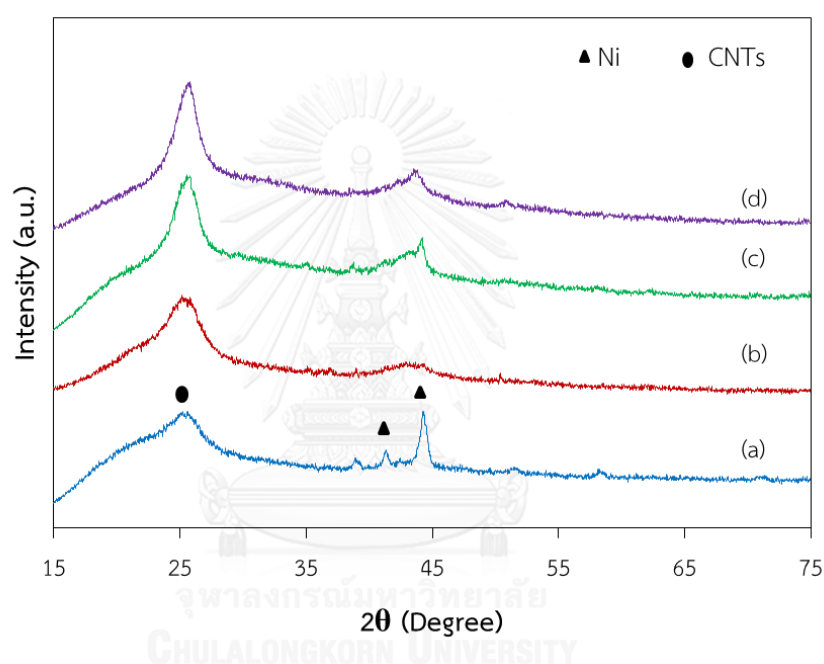
Figure 4.36 XRD patterns of the spent catalysts (a) 10NiSF, (b) 10NiSP, (c) 10NiCNTs-SF-E and (d) 10NiCNTs-SF-A
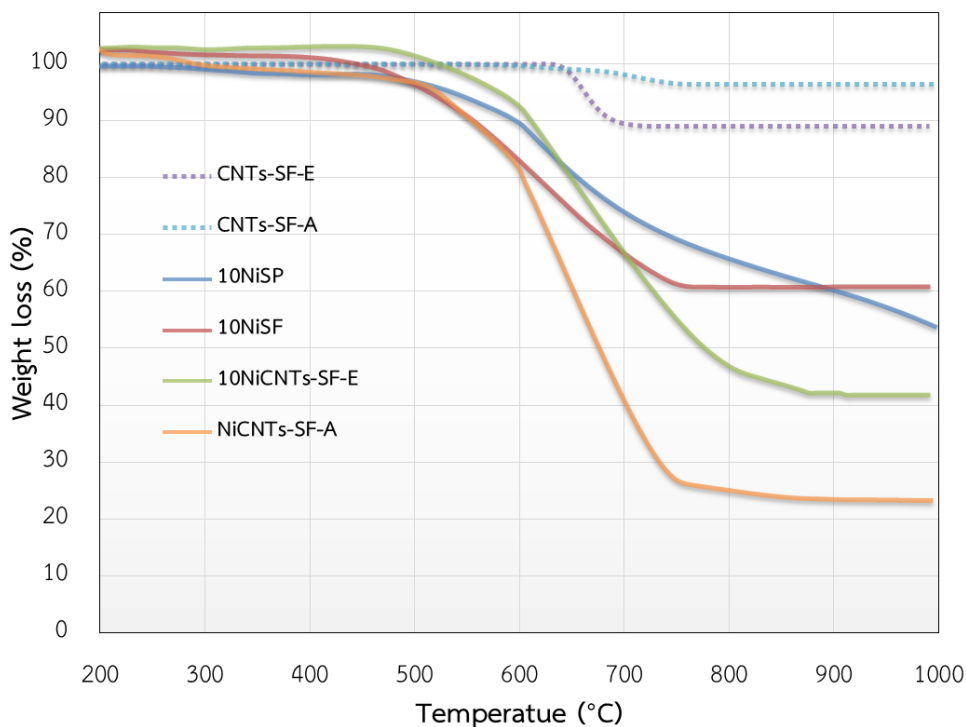
Figure 4.37 TG/DTA profiles of the spent catalysts

Figure 4.37 shows the thermogravimetric analysis of the catalysts after acetic acid steam reforming for 4 h. The weight loss stage of all catalysts was observed above 500 °C that can be ascribed to the oxidation of filamentous coke [88]. It can be seen that carbon formation occurred on fibrous composite and fiber catalysts were easily oxidized by oxidation and complete weight loss above 500 °C. Furthermore, the amount of carbon deposition on 10NiCNTs-SF-E and 10NiCNTs-SF-A catalysts was higher than on 10NiSF. On the other hand, 10NiSP generated a large amount of polymerized carbon which was difficult to be oxidized and could not estimate the exact amount of carbon [107].

CHAPTER V

CONCLUSIONS AND RECOMMENDATIONS

5.1 Co-production of hydrogen and carbon nanotubes-silica fiber (CNTs-SF-E) composite from ethanol steam reforming.

We have successfully synthesized silica fibers (SF) using sol–gel method assisted electrospinning technique. The SF was used as the support for Ni for ethanol steam reforming to produce hydrogen. Influential factors on hydrogen and CNTs (as a by-product), such as Ni loading, W/F, reaction temperature and steam to carbon ratio (S/C) were investigated. The optimized conditions of ESR in terms of conversion and hydrogen yield were established at Ni loading 10 %wt, W/F of 18 g_{cat}h/mol, reaction temperature of 600 °C and S/C of 9:1. Hydrogen yield reached the highest of 55% and CNTs yield of 8% was simultaneously observed. While the highest yield of CNTs 36% along with a hydrogen yield of 29% was obtained at Ni loading of 30 wt%, W/F 9 g_{cat}h/mol and S/C of 1:1. The novel CNTs-SF composite produced from ethanol steam reforming was uniformly distributed with outer and inner diameters of 20-30 nm and 5-11 nm, respectively. The novel composite comprised CNTs and SF offered the advantages of large surface area and entirely open structure, which allowed it more appealing for use as a catalyst support in various reactions.

5.2   Ni supported on CNTs-SF-E fiber catalysts for ethanol steam reforming

In this section, we have applied the fibrous CNTs-SF-E composite as a support catalyst for the low-temperature ethanol steam reforming by Ni loading at 5 and 10 wt%. The NiCNT-SF-E catalyst exhibited high dispersion and relatively high activity even at lower temperature. The 10NiCNT-SF-E catalyst had much higher catalytic performance in terms of activity and stability compared to 10NiSP and 10NiSF. The good performance in low-temperature ethanol steam reforming of 10NiCNT-SF-E could be attributed to the unique characteristics of the composite catalysts. The CNTs-SF-E composite possessed graphene layers and oxygen-containing surface group and combined the advantages of tubular structure silica fiber and CNTs. These could be beneficial to obtain small Ni phase particles size of 6–8 nm and to effectively stabilize the highly metal dispersion, which may account for the excellent catalytic activity of the CNTs-SF-E catalyst. In addition, the SF and CNT-SF-E supported Ni catalysts exhibited stable performance during 22 h on-stream without apparent deactivation, while SP supported Ni catalyst suffered from deactivation after 14 h on-stream because of serious carbon formation. The excellent coking-resistance ability of the CNTs-SF-E catalysts could be attributed to that carbon deposition on CNTs-SF-E catalysts were grown up and continuously extended the tube-length of CNTs. Moreover, the unique characteristics of CNTs-SF-E composite with stronger metal to support interaction combined with large area of π-electron cloud of CNTs could better stabilize and accelerate the rate of coke gasification and facilitate the regeneration of active nickel

surface as well as prevent sintering in the catalytic reaction. Therefore, carbon formation over the CNTs-SF catalysts had no effect on losses of active Ni species and the stability, achieving improved long-term stability.

5.3 Synthesis of carbon nanotubes-silica fibrous composite (CNTs-SF-A) by acetic acid steam reforming and its use as a novel catalyst support for acetic acid steam reforming

The CNTs-SF-A composite was synthesized by acetic steam reforming using the optimum conditions from the first part, Ni loading of 30 wt%, W/F of 9 g_{cat}h/mol and S/C of 1:1. Carbon produced from acetic acid stem reforming consisted of CNTs and curled shape filament carbon. CNTs produced from acetic acid steam reforming were larger outer diameters and a shorter length as compared to CNTs obtained from ethanol steam reforming. Although the amount of carbon formation produced from acetic acid was relatively higher than that from ethanol steam reforming, most of carbon formation was unstable carbon that could be easily removed by acids. These could be attributed to the different number of oxygen atoms of both feed which led to different behaviors in carbon formation.

We have applied CNTs-SF-A as a support catalyst for Ni catalyst for acetic acid steam reforming. The results showed that the NiCNTs-SF-A catalyst had high surface area and Ni particle sizes were small. The results were similar to 10NiCNTs-SF-E due to the graphene layers and oxygen-containing surface group of CNTs in both catalysts

which was known to promote the formation of smaller metal nanoparticles. The result of catalytic performance of 10NiCNTs-SF-E catalyst was much higher than that from 10NiCNTs-SF-A, but the selectivity of all products was quite similar to 10NiCNTs-SF-E. After 4 h of the reaction period, carbon formation occurred on fibrous composite and fiber catalysts was easily oxidized by oxidation and complete weight loss above 500 °C. On the other hand, carbon formation on 10NiSP was difficult to be oxidized and estimated the exact amount because 10NiSP surface was covered by a large amount of polymerized carbon.

5.4   Suggestion and Recommendation

Some aspects of the ethanol steam reforming and CNTs need further investigation as the following:

Steam reforming of ethanol

Although the Ni CNTs-SF-E exhibited enhance catalytic activities with small Ni particles and sufficient active areas as well as improve ability of catalyst, hydrogen produced from the catalyst was still low. Therefore, the development catalyst with high yield to hydrogen is required for further study. An addition of small amounts of the noble catalysts (Rh, Ru, Pd and Ir and) has been suggested as a promising way to improve hydrogen yield as well as catalytic stability.

The use of the CNTs-SF composite as a support catalyst

Ethanol steam reforming is very important process because this process not only produces hydrogen but also leads to the production of a valuable by product, CNTs without any containing amorphous impurity. CNTs can be used in many applications. For instance, CNTs are used as a part of composite for support catalyst. In this work, CNTs-SF composite obtained from ethanol steam reforming was used as a support for Ni-based catalyst in ethanol steam reforming and the synthesized catalyst exhibited the excellent performance in term of stability and high activity at lower reaction temperature. The CNTs-SF composite which combined the advantages of carbon nanostructure and the extremely open structure of silica fiber could be also used as a catalyst support in others reactions. As the formation of carbon on the surface of catalyst is the main cause for catalyst deactivation in various reactions. Therefore, the need of developing a new catalyst with highly activity and stability is very important and appears to be a challenging. In this respect, the use of CNTs-SF composite as a catalyst support can be one of the most attractive choices for other reactions.

CNTs separation technology

CNTs produced from this ethanol steam reforming seemed to be a good candidate for various applications. The development of method for separation CNTs from silica fibers with uniform and high purity requires further investigation. Currently,

the common methods widely used for separation CNTs from template are chemical and physical methods. Chemical method based on the idea of removal template silica, alumina from carbon nanowire by template method. In this method silica could be removed by dissolution in either HF or NaOH. Although the chemical method could effectively separate silica, this method always affects the CNTs structure. In contrast, the physical method such as chromatography, filtration, electrophoresis, high temperature and centrifugation could be used to remove silica from CNTs based on differences in solubility, aspect ratio, and physical size of CNTs and silica. Therefore this method could avoid the damage of CNTs structure. Nevertheless, this method is less effective, time-consuming, and complicated.
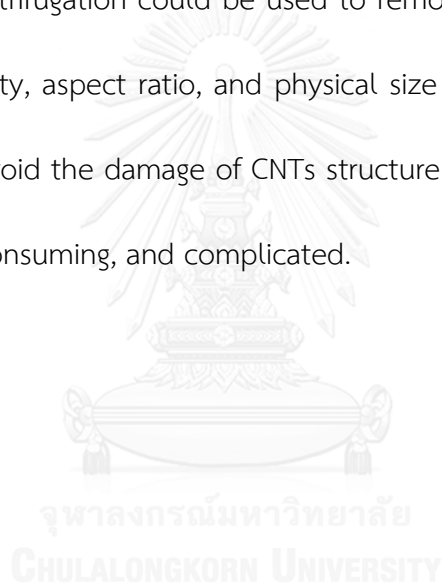
REFERENCES

1. Navarro, R.M., R. Guil, and J.L.G. Fierro, *Introduction to hydrogen production.* 2015: p. 21-61.

2. Contreras, J.L., et al., *Catalysts for H2 production using the ethanol steam reforming (a review).* International Journal of Hydrogen Energy, 2014. **39**(33): p. 18835-18853.

3. Carvalho, F.L.S., et al., *Bio-ethanol steam reforming for hydrogen production over Co3O4/CeO2 catalysts synthesized by one-step polymerization method.* Fuel Processing Technology, 2016. **142**: p. 182-191.

4. Bej, B., N.C. Pradhan, and S. Neogi, *Production of hydrogen by steam reforming of ethanol over alumina supported nano-NiO/SiO2 catalyst.* Catalysis Today, 2014. **237**: p. 80-88.

5. Li, D., et al., *Ceria-promoted Ni/SBA-15 catalysts for ethanol steam reforming with enhanced activity and resistance to deactivation.* Applied Catalysis B: Environmental, 2015. **176-177**: p. 532-541.

6. J. K. Chinthaginjala, K.S., and L. Lefferts, *<Preparation and Application of Carbon-Nanofiber Based Microstructured Materials as Catalyst Supports.pdf>.* Ind. Eng. Chem. Res, 2007. **46**: p. 3968-3978.

7. Lindo, M., et al., *Ethanol steam reforming on Ni/Al-SBA-15 catalysts: Effect of the aluminium content.* International Journal of Hydrogen Energy, 2010. **35**(11): p. 5895-5901.

8. Zhang, L., et al., *Ethanol steam reforming reactions over Al2O3·SiO2-supported Ni–La catalysts.* Fuel, 2009. **88**(3): p. 511-518.

9. Carrera Cerritos, R.l., et al., *Steam Reforming of Ethanol over Ni/Al2O3–La2O3Catalysts Synthesized by Sol–Gel.* Industrial & Engineering Chemistry Research, 2011. **50**(5): p. 2576-2584.

10. Zhang, C., et al., *Hydrogen Production via Steam Reforming of Ethanol on Phyllosilicate-Derived Ni/SiO2: Enhanced Metal–Support Interaction and*

Catalytic Stability. ACS Sustainable Chemistry & Engineering, 2012: p. 121214082043003.

11. Q. Zhang, M.W., T. Zhang, Y. Wang, X. Tang, P. Ning, *<A stable NiSBA-15 catalyst prepared by the IM and AM method.pdf>.* RSC Adv., 2015(5): p. 94016–94024.

12. Vita, A., et al., *Syngas production by methane oxy-steam reforming on Me/CeO2 (Me=Rh, Pt, Ni) catalyst lined on cordierite monoliths.* Applied Catalysis B: Environmental, 2015. **162**: p. 551-563.

13. Tang, Y., et al., *Microfibrous entrapped ZnO-CaO/Al2O3 for high efficiency hydrogen production via methanol steam reforming.* Particuology, 2010. **8**(3): p. 225-230.

14. Wen, M., et al., *Monolithic metal-fiber@HZSM-5 core–shell catalysts for methanol-to-propylene.* Microporous and Mesoporous Materials, 2015. **206**: p. 8-16.

15. Sadeghzadeh, S.M., *Ionic liquid immobilized onto fibrous nano-silica: A highly active and reusable catalyst for the synthesis of quinazoline-2,4(1H,3H)-diones.* Catalysis Communications, 2015. **72**: p. 91-96.

16. Le, X., et al., *Fibrous nano-silica containing immobilized Ni@Au core–shell nanoparticles: A highly active and reusable catalyst for the reduction of 4-nitrophenol and 2-nitroaniline.* Journal of Molecular Catalysis A: Chemical, 2014. **395**: p. 58-65.

17. Reubroycharoen, P., N. Tangkanaporn, and C. Chaiya, *Ni/SiO2 fiber catalyst prepared by electrospinning technique for glycerol reforming to synthesis gas.* 2010. **175**: p. 689-693.

18. Oosthuizen, R.S. and V.O. Nyamori, *Carbon Nanotubes as Supports for Palladium and Bimetallic Catalysts for Use in Hydrogenation Reactions.* Platinum Metals Review, 2011. **55**(3): p. 154-169.

19. Daş, E. and A.B. Yurtcan, *Effect of carbon ratio in the polypyrrole/carbon composite catalyst support on PEM fuel cell performance.* International Journal of Hydrogen Energy, 2016. **41**(30): p. 13171-13179.

20. Chernyak, S.A., et al., *New hybrid CNT–alumina supports for Co-based Fischer–Tropsch catalysts.* Fuel Processing Technology, 2015. **140**: p. 267-275.

21. Idriss, H., M. Scott, and V. Subramani, *Introduction to hydrogen and its properties.* 2015: p. 3-19.

22. Dincer, I. and C. Zamfirescu, *Hydrogen and Its Production.* 2016: p. 65-97.

23. French, R. and S. Czernik, *Catalytic pyrolysis of biomass for biofuels production.* Fuel Processing Technology, 2010. **91**(1): p. 25-32.

24. Ni M., L.D.Y.C., Leung M.K.H., Sumathy K., , *An overview of hydrogen production from biomass.* Fuel Processing Technology, 2006. **87**: p. 461-472.

25. L. Garcı́a, M.L.S., J. Arauzo, R. Bilbao, *<Catalytic pyrolysis of biomass influence of the catalyst pretreatment on gas yields.pdf>.* Journal of Analytical and Applied Pyrolysis, 2001. **58-59**: p. 491‒501.

26. Song, T., et al., *Experimental investigation on hydrogen production from biomass gasification in interconnected fluidized beds.* Biomass and Bioenergy, 2012. **36**: p. 258-267.

27. Y.C., L., *Catalytic valorization of glycerol to hydrogen and syngas, International Journal of Hydrogen Energy.* International Journal of Hydrogen Energy, 2013. **38**: p. 2678 - 2700.

28. Zhang, H., et al., *Comparison of non-catalytic and catalytic fast pyrolysis of corncob in a fluidized bed reactor.* Bioresour Technol, 2009. **100**(3): p. 1428-34.

29. Hossain, M.Z. and P.A. Charpentier, *Hydrogen production by gasification of biomass and opportunity fuels.* 2015: p. 137-175.

30. Chang, A.C.C., et al., *Biomass gasification for hydrogen production.* International Journal of Hydrogen Energy, 2011. **36**(21): p. 14252-14260.

31. Xie, Q., et al., *Syngas production by two-stage method of biomass catalytic pyrolysis and gasification.* Bioresour Technol, 2012. **110**: p. 603-9.

32. Nipattummakul, N., et al., *Steam gasification of oil palm trunk waste for clean syngas production.* Applied Energy, 2012. **92**: p. 778-782.

33. Lv P., Y.Z., Wu C., Ma L., *Bio-syngas production from biomass catalytic gasification, Energy Conversion and Management.* 2007(48): p. 1132–1139.

34. Joensen, F.a.J.R.R.-N., *<Conversion of hydrocarbons and alcohols for fuel cells.pdf>.* Journal of Power Sources, 2000(105(2)): p. 195-201

35. Silva, J.M., M.A. Soria, and L.M. Madeira, *Thermodynamic analysis of Glycerol Steam Reforming for hydrogen production with in situ hydrogen and carbon dioxide separation.* Journal of Power Sources, 2015. **273**: p. 423-430.

36. LeValley, T.L., A.R. Richard, and M. Fan, *The progress in water gas shift and steam reforming hydrogen production technologies – A review.* International Journal of Hydrogen Energy, 2014. **39**(30): p. 16983-17000.

37. Frusteri, F. and G. Bonura, *Hydrogen production by reforming of bio-alcohols.* 2015: p. 109-136.

38. Ni, M., D.Y.C. Leung, and M.K.H. Leung, *A review on reforming bio-ethanol for hydrogen production.* International Journal of Hydrogen Energy, 2007. **32**(15): p. 3238-3247.

39. Trane, R., et al., *Catalytic steam reforming of bio-oil.* International Journal of Hydrogen Energy, 2012. **37**(8): p. 6447-6472.

40. Benito, M., et al., *Bio-ethanol steam reforming: Insights on the mechanism for hydrogen production.* Journal of Power Sources, 2005. **151**: p. 11-17.

41. Vaidya, P.D. and A.E. Rodrigues, *Insight into steam reforming of ethanol to produce hydrogen for fuel cells.* Chemical Engineering Journal, 2006. **117**(1): p. 39-49.

42. Hu, X. and G. Lu, *Acetic acid steam reforming to hydrogen over Co–Ce/Al2O3 and Co–La/Al2O3 catalysts—The promotion effect of Ce and La addition.* Catalysis Communications, 2010. **12**(1): p. 50-53.

43. Basagiannis, A.C. and X.E. Verykios, *Catalytic steam reforming of acetic acid for hydrogen production.* International Journal of Hydrogen Energy, 2007. **32**(15): p. 3343-3355.

44. Lemonidou, A.A., et al., *Steam Reforming of Bio-oils to Hydrogen.* 2013: p. 467-493.

45.   Li, Z., et al., *Renewable hydrogen production by a mild-temperature steam reforming of the model compound acetic acid derived from bio-oil.* Journal of Molecular Catalysis A: Chemical, 2012. **355**: p. 123-133.

46.   Kamalkumar I. Gursahani, R.A., Randy D. Cortright, James A. Dumesic, *<Reaction kinetics measurements and analysis of reaction.pdf>.* Applied Catalysis A: General 2001. **222**: p. 369–392.

47.   Llorca, J., et al., *Efficient Production of Hydrogen over Supported Cobalt Catalysts from Ethanol Steam Reforming.* Journal of Catalysis, 2002. **209**(2): p. 306-317.

48.   Morlanés, N., *Reaction mechanism of naphtha steam reforming on nickel-based catalysts, and FTIR spectroscopy with CO adsorption to elucidate real active sites.* International Journal of Hydrogen Energy, 2013. **38**(9): p. 3588-3596.

49.   Llorca, J., et al., *Hydrogen from Bioethanol.* 2013: p. 135-169.

50.   Zhao, L., et al., *Ni-Co alloy catalyst from LaNi1–xCoxO3 perovskite supported on zirconia for steam reforming of ethanol.* Applied Catalysis B: Environmental, 2016. **187**: p. 19-29.

51.   Sanchezsanchez, M., R. Navarro, and J. Fierro, *Ethanol steam reforming over Ni/MxOyNi/MxOy–Al2O3Al2O3 (M=CeM=Ce, La, Zr and Mg) catalysts: Influence of support on the hydrogen production.* International Journal of Hydrogen Energy, 2007. **32**(10-11): p. 1462-1471.

52.   Mattos, L.V., et al., *Production of hydrogen from ethanol: review of reaction mechanism and catalyst deactivation.* Chem Rev, 2012. **112**(7): p. 4094-123.

53.   J.A Moulijn, A.E.v. Diepen, and F. Kapteijn, *<Catalyst deactivation is it predictable What to do.pdf>.* Applied Catalysis A: General, 2010. **212**(1-2): p. 3–16.

54.   Bartholomew, C.H., *<Mechanisms of catalyst deactivation.pdf>.* Applied Catalysis A: General, 2001. **210**(1-2): p. 17-60.

55.   Haynes, D.J. and D. Shekhawat, *Oxidative Steam Reforming.* 2011: p. 129-190.

56. Li, Y.-h., et al., *Multi-wall carbon nanotubes supported on carbon fiber paper synthesized by simple chemical vapor deposition.* Materials Science and Engineering B 2014(113–119): p. 187.

57. JONG, K.P.D. and J.W. GEUS, *Carbon Nanofibers: Catalytic Synthesis and Applications.* Catalysis Reviews Science and Engineering, 2000. **42**(4): p. 481-510.

58. Wang, G., et al., *Efficient production of hydrogen and multi-walled carbon nanotubes from ethanol over Fe/Al2O3 catalysts.* Fuel Processing Technology, 2011. **92**(3): p. 531-540.

59. Osorio-Vargas, P., et al., *Improved stability of Ni/Al2O3 catalysts by effect of promoters (La2O3, CeO2) for ethanol steam-reforming reaction.* Catalysis Today, 2016. **259**: p. 27-38.

60. Ross, J.R.H., *Catalyst Preparation.* 2012: p. 65-96.

61. J. K. Chinthaginjala, K.S., and L. Lefferts, *Preparation and Application of Carbon-Nanofiber Based Microstructured Materials as Catalyst Supports.* Ind. Eng. Chem. Res., 2007. **46**: p. 3968-3978.

62. Zhao, F., et al., *Synthesis and characterization of magnetic Fe/CNTs composites with controllable Fe nanoparticle concentration.* Physica B: Condensed Matter, 2012. **407**(13): p. 2495-2499.

63. Sun, C., et al., *In situ preparation of carbon/Fe3C composite nanofibers with excellent electromagnetic wave absorption properties.* Composites Part A: Applied Science and Manufacturing, 2017. **92**: p. 33-41.

64. Donphai, W., et al., *Effect of Ni-CNTs/mesocellular silica composite catalysts on carbon dioxide reforming of methane.* Applied Catalysis A: General, 2014. **475**: p. 16-26.

65. Huang, Z.-M., et al., *A review on polymer nanofibers by electrospinning and their applications in nanocomposites.* Composites Science and Technology, 2003. **63**(15): p. 2223-2253.

66. Baji, A., et al., *Electrospinning of polymer nanofibers: Effects on oriented morphology, structures and tensile properties.* Composites Science and Technology, 2010. **70**(5): p. 703-718.

67.   Zhao, Y., et al., *Fabrication of refining mesoporous silica nanofibers via electrospinning.* Materials Letters, 2008. **62**(1): p. 143-146.

68.   Batista, M.S., et al., *Characterization of the activity and stability of supported cobalt catalysts for the steam reforming of ethanol.* Journal of Power Sources, 2003. **124**(1): p. 99-103.

69.   Seelam, P.K., et al., *CNT-based catalysts for H2 production by ethanol reforming.* International Journal of Hydrogen Energy, 2010. **35**(22): p. 12588-12595.

70.   Yong, X., J. Pei-Wen, and L. Quan-Xin, *Carbon Nanofibers-Supported Ni Catalyst for Hydrogen Production from Bio-Oil through Low-Temperature Reforming.* Acta Physica Sinic, 2013. **29**: p. 1041-1047.

71.   Basagiannis, A.C. and X.E. Verykios, *Steam reforming of the aqueous fraction of bio-oil over structured Ru/MgO/Al2O3 catalysts.* Catalysis Today, 2007. **127**(1-4): p. 256-264.

72.   Seo, J.G., et al., *Hydrogen production by steam reforming of simulated liquefied natural gas (LNG) over mesoporous nickel–M–alumina (M=Ni, Ce, La, Y, Cs, Fe, Co, and Mg) aerogel catalysts.* International Journal of Hydrogen Energy, 2011. **36**(5): p. 3505-3514.

73.   van Haasterecht, T., et al., *Stability and activity of carbon nanofiber-supported catalysts in the aqueous phase reforming of ethylene glycol.* Journal of Energy Chemistry, 2013. **22**(2): p. 257-269.

74.   da Silva, A.L.M., et al., *Oxidative steam reforming of ethanol over carbon nanofiber supported Co catalysts.* Catalysis Today, 2011. **164**(1): p. 262-267.

75.   Bobadilla, L.F., et al., *Influence of the shape of Ni catalysts in the glycerol steam reforming.* Applied Catalysis B: Environmental, 2012. **123-124**: p. 379-390.

76.   Gao, L., G. Sun, and S. Kawi, *A study on methanol steam reforming to CO2 and H2 over the La2CuO4 nanofiber catalyst.* Journal of Solid State Chemistry, 2008. **181**(1): p. 7-13.

77.   Wang, Z., et al., *A study on carbon formation over fibrous NiO/CeO2 nanocatalysts during dry reforming of methane.* Catalysis Today, 2013. **216**: p. 44-49.

78.   Hu, X. and G. Lu, *Investigation of steam reforming of acetic acid to hydrogen over Ni–Co metal catalyst.* Journal of Molecular Catalysis A: Chemical, 2007. **261**(1): p. 43-48.

79.   Ratanathavorn, W., C. Samart, and P. Reubroycharoen, *Tinospora crispa-like ZSM-5/silica fibers synthesized by electrospinning and hydrothermal method.* Materials Letters, 2015. **159**: p. 135-137.

80.   Klaigaew, K., et al., *Effect of preparation methods on activation of cobalt catalyst supported on silica fiber for Fischer–Tropsch synthesis.* Chemical Engineering Journal, 2015. **278**: p. 166-173.

81.   Jo, S.W., et al., *Reasonable harmony of Ni and Mn in core@shell-structured NiMn@SiO2 catalysts prepared for hydrogen production from ethanol steam reforming.* Chemical Engineering Journal, 2016. **288**: p. 858-868.

82.   Gouveia Gil, A., et al., *Ni/SBA-15 Catalysts for combined steam methane reforming and water gas shift—Prepared for use in catalytic membrane reactors.* Applied Catalysis A: General, 2015. **506**: p. 188-196.

83.   Li, Z., et al., *Steam reforming of acetic acid over Ni/ZrO2 catalysts: Effects of nickel loading and particle size on product distribution and coke formation.* Applied Catalysis A: General, 2012. **417-418**: p. 281-289.

84.   Xie, H., et al., *Hydrogen production from steam reforming of simulated bio-oil over Ce–Ni/Co catalyst with in continuous CO2 capture.* International Journal of Hydrogen Energy, 2015. **40**(3): p. 1420-1428.

85.   Chen, R., et al., *Production of hydrogen-rich gas and multi-walled carbon nanotubes from ethanol decomposition over molybdenum modified Ni/MgO catalysts.* Journal of Energy Chemistry, 2014. **23**(2): p. 244-250.

86.   Fakeeha, A.H., et al., *Production of hydrogen and carbon nanofibers from methane over Ni–Co–Al catalysts.* International Journal of Hydrogen Energy, 2015. **40**(4): p. 1774-1781.

87.   Palacio, R., et al., *Decomposition of ethanol into H2-rich gas and carbon nanotubes over Ni, Co and Fe supported on SBA-15 and Aerosil.* Applied Catalysis A: General, 2015. **504**: p. 642-653.

88.   Saraswat, S.K. and K.K. Pant, *Ni–Cu–Zn/MCM-22 catalysts for simultaneous production of hydrogen and multiwall carbon nanotubes via thermo-catalytic decomposition of methane.* International Journal of Hydrogen Energy, 2011. **36**(21): p. 13352-13360.

89.   Li, F., et al., *Characterization of single-wall carbon nanotubes by N2 adsorption.* Carbon, 2004. **42**(12-13): p. 2375-2383.

90.   Zhang, J. and F. Li, *Coke-resistant Ni@SiO2 catalyst for dry reforming of methane.* Applied Catalysis B: Environmental, 2015. **176-177**: p. 513-521.

91.   Karimi, S., et al., *Cobalt supported on Graphene – A promising novel Fischer–Tropsch synthesis catalyst.* Applied Catalysis A: General, 2015. **499**: p. 188-196.

92.   Niu, J.J., et al., *An approach to carbon nanotubes with high surface area and large pore volume.* Microporous and Mesoporous Materials, 2007. **100**(1-3): p. 1-5.

93.   Sun, Y., C. Li, and A. Zhang, *Preparation of Ni/CNTs catalyst with high reducibility and their superior catalytic performance in benzene hydrogenation.* Applied Catalysis A: General, 2016. **522**: p. 180-187.

94.   Vicente, J., et al., *Reaction pathway for ethanol steam reforming on a Ni/SiO2 catalyst including coke formation.* International Journal of Hydrogen Energy, 2014. **39**(33): p. 18820-18834.

95.   A.R. Rautio, P.K.S., P. Mäki-Arvela, O. Pitkanen, M. Huuhtanen, R.L. Keiskib, K. Kordas, *Carbon supported catalysts in low temperature steam reforming of ethanol: study of catalyst performance.* RSC Adv. , 2015. **5**: p. 49487–49492.

96.   Wang, W., et al., *Mesoporous nickel catalyst supported on multi-walled carbon nanotubes for carbon dioxide methanation.* International Journal of Hydrogen Energy, 2016. **41**(2): p. 967-975.

97. López, E., et al., *Multiwalled carbon nanotubes-supported Nickel catalysts for the steam reforming of propane.* Journal of Materials Science, 2011. **47**(6): p. 2985-2994.

98. Ma, H., et al., *Efficient hydrogen production from ethanol steam reforming over La-modified ordered mesoporous Ni-based catalysts.* Applied Catalysis B: Environmental, 2016. **181**: p. 321-331.

99. Tourani, S., et al., *Synthesis of Reduced Graphene Oxide-Carbon Nanotubes (rGO–CNT) Composite and Its Use As a Novel Catalyst Support for Hydro-Purification of Crude Terephthalic Acid.* Industrial & Engineering Chemistry Research, 2015. **54**(31): p. 7591-7603.

100. Oemar, U., et al., *CO2reforming of methane over highly active La-promoted Ni supported on SBA-15 catalysts: mechanism and kinetic modelling.* Catal. Sci. Technol., 2016. **6**(4): p. 1173-1186.

101. Dasgupta, K., J.B. Joshi, and S. Banerjee, *Fluidized bed synthesis of carbon nanotubes – A review.* Chemical Engineering Journal, 2011. **171**(3): p. 841-869.

102. Chen, Y., et al., *Effect of different carbon sources on the growth of single-walled carbon nanotube from MCM-41 containing nickel.* Carbon, 2007. **45**(11): p. 2217-2228.

103. Davoodi, M.A., J. Towfighi, and A. Rashidi, *Facile synthesis of carbon nanotube/nanofiber paper on a water-soluble support in one-step by chemical vapor deposition.* Chemical Engineering Journal, 2013. **221**: p. 159-165.

104. Gallego, J., et al., *Synthesis of MWCNTs and hydrogen from ethanol catalytic decomposition over a Ni/La2O3 catalyst produced by the reduction of LaNiO3.* Applied Catalysis A: General, 2011. **397**(1-2): p. 73-81.

105. Datsyuk, V., et al., *Chemical oxidation of multiwalled carbon nanotubes.* Carbon, 2008. **46**(6): p. 833-840.

106. Yang, W., et al., *CO2 reforming of methane to syngas over highly-stable Ni/SBA-15 catalysts prepared by P123-assisted method.* International Journal of Hydrogen Energy, 2016. **41**(3): p. 1513-1523.

107. Yao, D., et al., *Hydrogen production from catalytic reforming of the aqueous fraction of pyrolysis bio-oil with modified Ni–Al catalysts.* International Journal of Hydrogen Energy, 2014. **39**(27): p. 14642-14652.

APPENDICES

APPENDIX A

CALCULATION FOR CATALYST PREPARATION

Calculation for the preparation of silica fiber (SF)

Chemical properties of reagents

Substance	MW(g/mol)	Density(g/cm³)
Silica (SiO$_2$)	60.09	2.20
Ethanol (C$_2$H$_5$OH)	46.07	0.789
ID water (H$_2$O)	18.00	1.00
Hydrochloric acid 37.0% (HCl)	36.46	1.18
Tetraethyl orthosilicate 95%	208.33	0.933

Basis 7.5 g of silica

TEOS 1 mol = silica 1 mol

Therefore, *mole of TEOS* $= \dfrac{7.5 \text{ g}}{60.01 \text{ g/mol}} = 0.1248 \ mol$

weight of TEOS $= \dfrac{0.1248 \text{ mol} \times 208.33 \text{ g /mol} \times 95}{100} = 27.4 \ g$

$volume \ of \ TEOS$ $= \dfrac{27.4 \text{ g}}{0.933 \text{ g}/cm^3} = 29.3 \ ml$

For Sol-gel, the mol ratio of TEOS:EtOH:H$_2$O:HCl equal to 1:2:2:0.01

From above TEOS = 0.1248 mol

So, TEOS:EtOH:H$_2$O:HCl = 0.1248: 0.2494: 0.2494: 1.2x10^{-3}

$$\therefore \text{EtOH} = \frac{0.2494 \text{ mol} \times 46.07 \text{ g/mol}}{0.789 \text{ g}/cm^3} = 14.56 \; ml$$

$$\therefore \text{H}_2\text{O} = \frac{0.2494 \text{ mol} \times 18 \text{ g/mol}}{1 \text{ g}/cm^3} = 4.49 \; ml$$

$$\therefore \text{HCl} = \frac{1.2 \times 10^{-3} \text{ mol} \times 36.46 \text{ g/mol}}{1.18 \text{ g}/cm^3} = 0.04 \; ml$$

Calculation for the preparation of nickel loading

	MW(g/mol)
Nickel (Ni)	58.69
Nickel (II) nitrate hexahydrate (Ni(NO$_3$)$_2$.6H$_2$O)	290.79

10 wt% Ni/SiO2

Based on 100 g of catalyst used, the composition of the catalyst will be as follows:

SiO2 of 90 g and Ni of 10 g

For 5 g of SiO$_2$;

Ni required = 5 x $\dfrac{10}{90}$ = 0.555 g

Ni 0.555 g was prepared from Ni(NO$_3$)$_2$.6H$_2$O

0.555 of Ni required from 100% $Ni(NO_3)_2.6H_2O$

$$= \frac{\text{MW of Ni(NO3)2.6H2O}}{\text{MW of Ni}} \times Ni \; required$$

$$= \frac{290.79}{58.69} \; \text{X} \; 0.555$$

$$= 2.752 \; g$$

Therefore, required from $Ni(NO_3)_2.6H_2O$ = 2.752 g

APPENDIX B

DATA OF ETHANOL STEAM REFORMING

Data of experiment of 10NiSP catalyst for ethanol steam reforming

Condition of experiment : Weight of catalyst 0.2113 g

: Pressure 1 MPa

: Temperature 450 °C

: S/C ratio 9

: W/F 18 g_{cat}h/mol

: 1%H_2/1%CO/1%CO_2/1%CH_4/1%C_2H_4/1%C_2H_6

Data from Gas chromatography

STD gas (TCD)	1	2	3	Average
H_2	11245	11049	12249	11514
CO	21010	21781	21009.801	21267
CO_2	18573	18880	18557	18670
STD (FID)	1	2	3	Average
CH_4	194735	198894	185415	193015
C_2H_4	392748	419448	409593	407263
C_2H_6	417389	407466	394184	406346
C_2H_5OH	35230772	29521290	37660120	34137394

Data from reaction TCD and FID

Time (h)	1	2	3	4
H_2	529103.8	537246.7	537246.7	538429
CO	114396.3	96273.78	95133	121053.4
CO_2	207982.1	209406.4	205235.1	212196.3
CH_4	680498	624779.9	681156.1	646332.9
C_2H_4	0	0	0	0
C_2H_6	4309.908	5062.5	5062.5	3436

APPENDIX C

ETHANOL CONVERSION AND SELECTIVIES CALCULATION

The catalyst preference for the ethanol steam reforming was evaluated in terms of activity for ethanol conversion. Ethanol conversion is defined as moles of ethanol convert with respect to ethanol in feed:

Calculation of glycerol conversion and gas product selectivity

10NiSP catalyst at the 4 h of reaction time

$F_{EtOH,in}$

	H_2O	EtOH
MW (g/mol)	18	46
mole (mol)	9	1
weight (g)	162	46
Density(g/cm^3)	1	0.789
Volume(cm^3)	162	58.3

Determine %volume (V) of ethanol

$$\%W_{EtOH} = \frac{W_{EtOH}}{(W_{EtOH} + W_{water})} \times 100 = \frac{46}{(46 + 162)} \times 100 = 22.11\%$$

Determine weight (W) of mixture fed to the reformer

$$W_{used} = W_{initial} - W_{final} = 9.6 \text{ g}$$

$$F_{EtOH,in} = \frac{9.6 \ g \ \times \ 22.11 \ \times 1 \ mol}{46 \ g \ \times 100} = 0.0461 \ mol = \frac{0.0461 \ mol \times 1000}{240 \ min}$$
$$= 0.1922 \ mmol/min$$

$F_{EtOH,out}$

STD EtOH (99.9%) 1 ml peak area = 34137394

Average peak area of EtOH in liquid phase = 10879461

$$F_{EtOH,out} = \frac{10879461 \ \times 99.9 \ \times 1 \ cm^3 \times \frac{0.789g}{cm^3} \times 1mol}{34137394 \times 100 \times 46 \ g} = 0.005460 \ \ mol$$

Therefore,

$$EtOH \ conversion \ (\%) = \frac{0.0461 - 0.00546}{0.0461} \times 100 = 87\%$$

From
$$S_i \ (\%) = \frac{\text{mole of gaseous product } i \times 100}{\text{mole all gaseous products}}$$

At 4 h flow rate output = 34.09 mL/min

$$mole \ of \ CO \ = \frac{\text{Area CO}}{\text{Area std CO}} = \frac{121053}{21267} = 5.69 \ \% = \frac{5.69 \ \times 34.09 \ ml/ \ min \times 1000}{100 \ \times 22400 \ ml/mol} = 0.08663 \ mmol/min$$

$$mole \ of \ CO_2 \ = \frac{\text{Area } CO_2}{\text{Area std } CO_2} = \frac{212196.297}{18670} = 11.37 \ \% = \frac{11.37 \times 34.09 \ ml/ \ min \times 1000}{100 \ \times 22400 \ ml/mol} = 0.1729 \ mmol/min$$

$$mole \ of \ CH_4 \ = \frac{\text{Area } CH_4}{\text{Area std } CH_4} = \frac{646332.875}{193015} = 3.12\% = \frac{3.12 \times 34.09 \ ml/ \ min \times 1000}{100 \ \times 22400 \ ml/mol} = 0.04754 \ mmol/min$$

$$mole \ of \ C_2H_6 \ = \frac{\text{Area } C_2H_6}{\text{Area std } C_2H_6} = \frac{3436}{406346} = 0.01 \ \% = \frac{2 \times 0.01 \times 34.09 \ ml/ \ min \times 1000}{100 \ \times 22400 \ ml/mol} = 0.00026 \ mmol/min$$

$mole \ of \ total \ carbon \ = CO + \ CO_2 \ + \ CH_4 + \ C_2H_6$

$mole \ of \ total \ carbon \ = 0.08663 + \ 0.01729 + \ 0.04754 + \ 0.00026$ = 0.3074 mmol/min

Therefore

$$S_i \ (\%) = \frac{\text{mole of gaseous product } i \ \times 100}{\text{mole all gaseous products}}$$

$$S_{CO} \ (\%) = \frac{0.08663 \times 100}{0.3074} = 28.18\%$$

$$S_{CO_2}\ (\%) = \frac{0.1729 \times 100}{0.3074} = 56.27\%$$

$$S_{CH_4}\ (\%) = \frac{0.04754 \times 100}{0.3074} = 15.46\%$$

$$S_{CH_4}\ (\%) = \frac{0.00026 \times 100}{0.3074} = 0.08\%$$

VITA

Miss Natthawan Prasongthum was born on May 17, 1988 in Mukdahan, Thailand. She graduated with Bachelor's degree of science,majoring in Chemistry, Faculty of Science, Ubon Ratchathani University in 2010 and Master's degree of science, majoring in Petrochemistry and Polymer Science, Faculty of Science, Chulalongkorn University in 2012. Present she has been a graduate student in Program of Petrochemistry, Faculty of Science, Chulalongkron University, Bangkok, Thailand since 2013 and finished her study in 2016.

Publication

N. Natthawan, P. Paweesuda, P. Reubroycharoen, Highly active and stable Ni supported on CNTs-SiO2 fiber catalysts for steam reforming of ethanol, Fuel Processing Technology Journal. (Submitted)

Presentation Experience

Poster presentation: Co-production of hydrogen and carbon nanotubes (CNTs)-silica fibers (SF) composite from ethanol steam reforming and its use as a catalyst support for ethanol steam reforming 2016, 2nd International Symposium on Catalytic Science and Technology in Sustainable Energy and Environment (EECAT 2016), 11-15/10/2015, Tianjin, China.

Oral presentation: Preparation of Co/SiO2 -Al2O3 fiber by Electrospinning for Fischer-Tropsch Synthesis, The 8th International Conference on Materials Science and Technology (MSAT-8), 15-16/12/2014, Bangkok, Thailand.